
ACTIVE PLASMONICS AND METAMATERIALS

By
MOHAMED ELKABBASH

Submitted in partial fulfillment of the requirements of the degree of Doctor of
Philosophy

Department of Physics

CASE WESTERN RESERVE UNIVERSITY

January, 2018

**CASE WESTERN RESERVE UNIVERSITY
SCHOOL OF GRADUATE STUDIES**

We hereby approve the thesis/dissertation of

Mohamed ElKabbash

Candidate for the degree of **Doctor of Philosophy***.

Committee Chair
Giuseppe Strangi

Committee Member
Michael Hinczewski

Committee Member
Jesse Berezovsky

Committee Member
Mohan Sankaran
Date of Defense
11/07/2017

*We also certify that written approval has been obtained
for any proprietary material contained therein

**To everyone who nurtured me with love and
knowledge.
To my late Grandmother, Galilah, and my mom Enas.**

Acknowledgments

This work was only possible through the support of many people. I would like to thank my supervisor, prof.Strangi, for mentoring, supporting and believing in me throughout my PhD program. I would also like to thank my committee members, Prof. Hinczewski, Prof.

Berezovsky, and Prof. Sankaran. In particular, I would like to thank Prof. Hinczewski whom I just wrote his name without copying from the email address book for the first time and who provided me with mentorship and support beyond what I would expect or ask for.

I would also like to thank my collaborators. First, I would like to thank professor Nader Engheta for his support and being a wonderful scientist and person. I would also like to thank professor Humeyra Caglayan for her support.

Secondly, I would like to thank my colleagues and lab mates, Alireza, Sreekanth and Melissa who were postdocs when I joined the lab and whom I enjoyed their company in the beginning of my PhD. I would also like to thank the brilliant undergraduate students who worked with me and enabled me to have a productive and fun PhD. Yandong Li, Quang Nguyen, Jacob Moran, Theodore Letsou, Nathaniel Hoffman, Alexander Yaney, Pratyusha Sambaru, Nick Ramey, and Kelsey Darrah. I have learned from them more than what I taught them. I would also like to thank my new lab mates Glynis Schumacher and Sharmistha Chatterjee for carrying the lab work wonderfully.

Last but not least, I would like to thank my undergraduate physics mentors at Illinois Wesleyan University, Professor Bruno deHarak, Professor Gabe Spalding, Professor Narendra Jaggi and professor Thushara Perera. Without their support and endless effort, I would not have made it so far.

Contents

Abstract	1
Part I: Active plasmonics	4
Chapter I: Active plasmonics: A brief background	5
1. Optical properties of noble metals	5
1.1. The Drude model	6
1.2. Optical properties of real metals	7
2. Plasmons et. al. , a brief overview	8
2.1. Plasmons	8
2.2. Plasmon-polaritons	9
2.3. Surface plasmon-polaritons	10
3. Optical excitation of propagating surface plasmon-polaritons	16
3.1. Momentum matching via diffraction	16
3.2. Momentum matching via tunneling	17
4. Active plasmonics; the origins	23
4.1. Activity based on modulating ϵ_D	23
4.2. Activity based on modulating ϵ_M	24
4.3. Activity based on modulating ω_p	25
4.4. Activity based on introducing optical gain	26
4.5. Activity due to plasmon hybridization	27
5. References	29
Chapter II: Ultrafast transient optical loss dynamics in exciton-plasmon nano-assemblies	31
1. Introduction to compensation of plasmonic losses with gain	31
2. Results and discussion	36
2.1. Samples characterization	36
2.2. Ultrafast Transient Absorption Spectroscopy measurements (UTAS)	37
2.3. Transient decay kinetics	47
3. Conclusion	51
4. Experimental	51
4.1. Preparation of nanocomposite hybrid systems	51
4.2. Characterization and Measurements	51
5. References	
Chapter III: Room temperature dynamic control of spontaneous emission rate in a single plasmonic nano-cavity	57
1. Introduction to lifetime modification in plasmonic nano-cavities	58
2. Results and discussion	61

2.1. Sample characterization	61
2.2. Time resolved lifetime measurements	62
2.3. All optical modulation of quantum emitter lifetime	65
2.4. Lack of stimulated emission as an alternative mechanism	66
2.5. Excluding plasmonic heating from affecting the measured SE lifetime	67
2.6. Spectral shape modification of emission for PNC coupled emitters	69
3. Methods	71
4. References	74
Chapter IV: Tunable Black Gold: Controlling the near field coupling of immobilized Au nanoparticles embedded in mesoporous silica capsules	79
1. Introduction to plasmonic black gold	80
2. Theoretical background	82
3. Results and discussion	84
4. Methods	90
5. References	94
Part II Active thin-film Metamaterials	96
Chapter I: Active interference based thin-film metamaterials	98
1. Interference; a brief overview	98
2. Amplitude splitting interference in thin-films	101
3. Optical coating perfect light absorbers	105
4. References	108
Chapter II: Iridescence Free and Narrow Band Perfect Light Absorption in Critically Coupled Metal-High Index Dielectric Cavities	110
1. Introduction to thin film cavity absorbers	110
2. Theoretical background	113
3. Experimental and discussion	116
4. Methods	123
5. References	124
Chapter III: Hydrogen sensing using thin-film cavity perfect light absorber	126
1. Introduction to nano-photonic hydrogen sensing	126
2. Thin-film absorber sensor design	128
3. Experimental	129
4. References	133
Chapter IV: Nanometer optical coating absorbers using loss-free dielectrics and low conductivity metals	136
1. Introduction to optical coating absorbers	136
2. Results and discussion	138
3. Conclusion and outlook	146
4. References	147
Chapter V: Hydrogen sensing using optical coating light absorber	149
1. Background and introduction	149

2. Results and discussion	151
3. References	155
Bibliography	157

List of Figures

Part I: Active Plasmonics:

- Figure 1-1 Charge density oscillation driven by a) longitudinal, b) transverse electric field. A net macroscopic charge density oscillation is only possible with a longitudinal field..... 9
- Figure 1-2 The dispersion ω_{sp} (red dotted line) for surface plasmon propagation in a Drude metal appears to result from avoided crossing between the plasmon frequency ω_p (blue line) and the light line $\omega = ck$ (black line).....10
- Figure 1-3 Schematic of propagating SPP. A TM polarized light can excite a propagating surface mode that is evanescently decaying in the transverse direction as well as in the propagation direction due to the existence of losses in metal..... 11
- Figure 1-4 Localized surface plasmon resonance: Metals with bound surface, i.e., with features smaller or similar to the incident wavelength, can support radiative bound modes. These modes correspond to standing electromagnetic waves coupled to charge density oscillations. For small spheres, the most prevalent mode is the dipolar mode depicted in the figure.....14
- Figure 1-5 Excitation of propagating SPP via diffraction: a) A scatterer can diffract incident light to a continuum of scattered waves with different momenta. Some components can launch circular SPPs centered at the scatterer. b) Irradiating the edge of a metal strip scatters light where some components of the scattered light excite an SPP away from the edge. c) Using a diffraction grating, only certain momentum components are generated, if one of them matches the SPP momentum for a given angle, an SPP is launched in the direction of transverse to the grating..... 15
- Figure 1-6 TIR and frustrated TIR: a) Light incident from a medium with a given refractive index on another with lower refractive index can experience TIR. The field only evanescently decay inside the lower index medium. b) If a third medium with a refractive index higher than that of medium 2, the field is no longer evanescent in 3 and energy can propagate..... 18
- Figure 1-7 Excitation of SPP via tunneling using a prism: a) The Kretschmann configuration; light incident at an angle $[\theta_{sp} \geq \theta_c]$ experiences TIR. The field tunnels through a thin-metal film and excites an SPP at the metal-dielectric interface with refractive index nD if $n_{Prism} > nD$. b) The double-Kretschmann configuration; by adding a dielectric spacer with refractive index $n_{Prism} > nD1$ it is possible to excite an SPP on both sides of the metal thin-film. c) The Otto configuration; a spacer dielectric layer, usually air, between a prism and a thick metal layer allow for SPP excitation at the metal-air interface.....19

Figure 1-8 Excitation of SPP with an SPP: A PSPP is evanescent in the direction orthogonal to its propagation as it experiences TIR at the metal-dielectric interface. Placing a metal thin-film within the spatial range of the evanescent field allows for exciting another PSPP. A metal-dielectric thin film stack can support multiple PSPP excitations..... 21

Figure 1-9 Ellipsoidal and hyperbolic dispersions: a) The dispersion of a conventional material with permittivity sharing the same sign in all three basis directions forming an ellipsoidal dispersion. b) If the permittivity in the orthogonal direction is negative while in the parallel direction is positive, the system has a type-I hyperbolic dispersion. c) If the permittivity in the orthogonal direction is positive while in the parallel direction is negative, the system has a type-II hyperbolic dispersion..... 22

Figure 2-1 (a) A schematic of fabricated nanocomposite PDMS films with embedded, I) CdSe@ZnS QDs (GS), II) Au NPs (AuL, AuH) and III) mixture of Au NPs and QDs (GS_AuL, GS_AuH). (b) The QDs normalized extinction and emission. The emission maximum is ≈ 570 nm, and extinction maximum is ≈ 545 nm (c) The extinction spectra of AuL and GS_AuL. AuL has a broad extinction due to NP aggregation. GS_AuL extinction maximum is a convolution of the extinction of both QDs and NPs. An estimate of the “true” plasmon extinction of NPs is presented in the Electronic Supplementary Material section 1 and its maximum is ≈ 590 nm.....35

Figure 2-2 Normalized extinction of GS_AuL before and after excluding the extinction of the incorporated QDs. The extinction of Au NPs in GS_AuL is found to be located at ≈ 590 nm.....37

Figure 2-3 (a) Transient Absorption (TA) results for GS for three delay times; 650 fs, 33 ps, and 1 ns for 1 μ J pump energy. We observe a broadband bleach that has a maximum around 550 nm due to the band filling effect. (b) Pumping GS with 800 nm pump wavelength we observe no bleach since we are not exciting any QDs.....39

Figure 2-4 (a) TA results for AuL for three delay times; 650 fs, 1.3 ps, and 2.5 ps. The bleach maximum is ≈ 575 nm. The TA profile is due to creating hot electrons that modify the NPs permittivity. An absorption wing appears at higher energies with respect to the bleach. There is another low energy absorption wing that is below the noise level. Additionally, the bleach maximum blue shifts as the delay time increases due to reduced EOPRD (b) Excitation of AuL with 400 nm and 800 nm pump wavelengths after 650 fs probe delay exhibits similar TA behavior.....39

Figure 2-5 (a) TA results for GS_AuL for 650 fs, 2.5 ps, and 10 ps delay times. The bleach maxima blue shifts as a function of delay time due to reduced EOPRD. In (b) we compare the bleach magnitude for GS, AuL and GS_AuL. The bleach is considerably stronger for GS_AuL than the combined bleach of both GS and AuL indicating the existence of loss mitigation. However, the TA spectra of AuL and GS-AuL are qualitatively similar..... 41

Figure 2-6 (a) The TA of GS_AuH for three delay times; 650 fs, 2.47 ps, and 5.43 ps shows similar behavior to that of GS-AuL. Compared to AuH, that has the same NP concentration, we see in (b) that the TA spectrum is significantly larger in magnitude due to loss

mitigation. This effect does not take place upon pumping GS_AuH with 800 nm as shown in (c). (d) Shows a comparison between the UTAS results for GS_AuL and GS_AuH.....43

Figure 2-7 Bird-eye view diagrams of GS_AuL for pump wavelengths (a) 400 nm (b) 800 nm. The TA signal magnitude is considerably higher for 400 nm excitation compared to 800 nm excitation. At 800 nm we do not excite the gain and thus we exclude the contribution from loss compensation to the bleach.....44

Figure 2- 8 Maximum bleach wavelength vs. Pump energy for GS_AuL. The maximum bleach wavelength shifts is pulled towards the emission maximum of the coupled gain due to enhanced loss mitigation as a function of pump power.....46

Figure 2- 9 Transient bleach dynamics results of GS, GS_AuL and GS_AuH and their theoretical fitting. The shortening of the bleach decay time for GS_AuH compared to GS_AuL reflects the effect of increasing the acceptor's concentration on gain depletion..... 48

Figure 3-1 Schematic of the coherent energy transfer process where multiple emitters (here two emitters) are coupled via a virtual plasmon to coherently transfer their energy to a plasmonic nanocavity at a higher energy transfer rate..... 59

Figure 3-2 Characterization of integrated plasmonic nano-cavities: a, SEM image of the nano-pillar array (scale bar= 3 μ m). b, a schematic of the nano-pillar PNC, the QDs are spin-coated on a polymeric scaffold, then an Au layer is deposited. c, The measured scattering for nano-pillar array; the resonance maximum was determined by fitting the data with a lorentzian function. The measured resonance closely agrees with the simulated absorption (black dashed line) and scattering (red dashed line) presented in d. e, Shows the PL of the QD spççin coated on an Au film (black spheres) compared to QD incorporated in a single PNC (red spheres)..... 60

Figure 3-3 Intensity dependence of SE rate: a, b Measured time-resolved QD emission for five different excitation intensities for the PNC (a) and the reference Au film (b). The SE lifetime is intensity dependent for the PNC case only. c, The fitted SE rate fast component (black spheres) and slow component (red spheres) for the PNC and in d, for the reference Au film..... 62

Figure 3-4 a) The ratio of the fast and slow rates for QDs on an Au film and inside a plasmonic nanopillar. The ratio provides us information about the origin of both rates. According to the statistical scaling law at room temperature, a ratio of 3 corresponds to the excitation of charged biexcitons and charged excitons for the fast and slow rates respectively. For QDs inside the nanopillar, the ratio is maintained indicating that the number of coherent biexcitons and excitons is the same for a given excitation intensity. b) Experimental vs. calculated fast SE rate. The calculation was done assuming that the origin of the intensity dependence of the SE rate is due to the plasmonic Dicke effect..... 63

Figure 3-5 Reversible tuning of SE rate: for a, the fast and b, slow SE rate components. The excitation intensity is decreasing in the grey shaded region and increasing in the blue shaded region..... 65

Figure 3-6 Absence of stimulated emission: a) Photoluminescence spectrum and b) its corresponding emission maximum (at 631nm) and c) Full-width half maximum. Given that the emission spectrum is neither growing non-linearly at any point nor narrowing, stimulated emission cannot be taking place. d) shows the corresponding lifetime components as a function of pump intensity for the same intensity range and on the same nano-pillar.....	66
Figure 3- 7 a, shows the emission spectrum as a function of pump power. In b, we show the corresponding lifetime as we change the pump power. The emission at 400 microwatts resembles that of heated QDs. The corresponding lifetime is longer than the lifetime at 40 microwatts excitation power.....	69
Figure 3-8 a, shows the emission spectrum as a function of pump power. In b, we show the corresponding lifetime as we change the pump power. The emission at 400 microwatts resembles that of heated QDs. The corresponding lifetime is longer than the lifetime at 40 microwatts excitation power.....	69
Figure 3-9 a, Array of nano-pillars spin-coated with QDs. b, SEM image showing the tip of a pillar where we have QDs landing on its surface. c, The measured scattering of the nano-pillars showing a maximum ~ 650 nm. d, The normalized emission on and off the pillars. The emission on the pillars is redshifted towards the pillars resonant maximum and is broader.....	70
Figure 4-1 Calculations for local field intensity of Au NPs chain with diameters (a) 10nm (b) 15nm, (c) 19nm, and (d) 28nm. The interaction between the NPs is size dependent due to the reduced inter-particle distance.....	84
Figure 4-2 TEM images of Silica shells embedded with pinned Au NPs for (a) S1 ($d = 10$ nm), (b) S2 ($d = 15$ nm), (c) S3 ($d = 19$ nm), and (d) S4 ($d = 28$ nm). For S1, the NPs are well separated and should exhibit no significant inter-particle coupling. As the NPs size increase in S2, the inter-particle distance becomes smaller than the NPs diameter. Further increase of the NP size in S3 and S4 results in the formation of NP aggregates.....	85
Figure 4-3 Schematic of mesoporous silica shell with Au NPs: (a) For small size NPs the near field of resonating NPs is not coupled. However, when the NPs size increases as in (b) the NPs near fields start to couple resulting in collective resonances and broadening in the plasmon resonance.....	86
Figure 4-4 Size dependent plasmon resonance. (a) The measured normalized extinction of S1, S2, S3, and S4. The extinction broadens with the decrease of inter-particle distance. In (b) Pictures of S1, S2, S3, and S4 (from left to right) are shown. It is difficult to see the difference between S2, S3, and S4 because they all strongly absorb in the visible. The plasmon band broadening is associated with a redshift in the extinction maximum as shown in (c). We compare the extinction of S4 with the Air Mass (AM) solar spectrum at sea level in (d). It is clear that S4 extinction engulfs the AM solar spectrum from the visible to the SWIR.....	87

Figure 4-5 Effect of individual NP size. a) TEM image of S5; a 1.34 μm mesocapsule embedding NPs with mean diameter $\sim 18.6 \pm 1.5 \text{ nm}$. b) By comparing the extinction of S5 with that of S3 we see that although their NPs share similar size, the plasmon resonance for S3 is significantly broader. By visually examining S5 it is clear that due to the larger surface area of S5 silica shell, the inter-particle distance is larger than that in S3..... 89

Part II: Active Metamaterials:

Figure 1-1 Fabry-Perot interference in dielectric thin films..... 102

Figure 1-2 Fabry-Perot etalon with an infinite bottom metal film..... 104

Figure 1-3 Lossless dielectric thin-film coating on a metal with finite conductivity. Light suffers limited absorption as it reflects from the metal, however, most light intensity escapes the resonator due to the weak reflection from the dielectric at the I-II interface compared to the reflection from the metal-dielectric II-III interface..... 106

Figure 1-4 Lossy dielectric thin-film coating on a metal with finite conductivity. The strong losses in the dielectric allows, under the right conditions, for perfect cancellation of reflected light and the wave can be absorbed entirely inside the resonator..... 107

Figure 2-1 (a) Wavelength $\lambda_{\text{min}}(\theta)$ at which reflectance is minimized in the NIR region, as a function of incident angle θ for p and s polarized light. Dots correspond to the solution of the exact transfer matrix approach, while solid lines correspond to the solution of the approximate theory, Eq. (1). Two systems are compared: Ag-MMA-Ag (red/orange) and Ag-Ge-Ag (blue/dark blue), with thicknesses and optical constants..... 116

Figure 2-2 NIR perfect absorber. a, b, Experimental reflectivity spectra for the Ag (13.5nm)-Ge (130nm)-Ag (70nm) and Ag (22nm)-MMA (560nm)-Ag(70 nm) NIR absorbers, respectively, for angles of incidence from 15° to 75° . c,d The calculated spectra corresponding to those in a, b respectively. The iridescence of a low index dielectric (MMA) is clear compared to the angle insensitivity of high index dielectric (Ge)..... 117

Figure 2-3 Visible light absorber. a, b Experimental and calculated reflectivity spectra for Ag (30nm)-TiO₂ (117nm)-Ag (100nm)absorber respectively. Optical images for two wide angle range visible absorbers are presented in c, d, and e for $\approx 0^\circ, 40^\circ$ and 80° . Clearly there is no color change for a wide-angle range validating our proposed approach..... 120

Figure 2-4 Transmission for NIR and visible cavity. a) For the NIR absorber and b) the visible absorber. The transmission is negligible for both systems..... 121

Figure 2-5 Angular reflection for s polarized light. a) For the NIR and b) the visible absorbers. Both systems exhibit strong angle independence over the measured range of angles, however, only the visible absorber shows super and strong absorption..... 122

Figure 3-1 Fabry-Perot cavity absorber sensor: a) A light absorber, metal (Pd)-dielectric (TiO₂)-metal (Ag) cavity. The reflection decrease due to destructive interference b) Exposing the absorber to hydrogen convert the Pd layer to a hydride PdH_x with a given

hydrogen atomic ratio (x). The cavity can be designed such that formation of the hydride results in total destructive interference and perfect light absorption.....	128
Figure 3-2 Schematic of the sensing setup: A microfluidic channel is attached to the thin-film absorber and connected to two mass flow controllers (MFCs). One MFC controls the flow of nitrogen mixed with hydrogen (4% in concentration) and another MFC controls the flow of pure nitrogen. The sensor is then placed on a variable angle ellipsometer to measure the angular reflectivity.....	130
Figure 3-3 Reflectance as a function of hydrogen concentration: The reflectivity of the cavity absorber as a function of hydrogen concentration. The absorption mode red-shifts and decrease in absorption.	131
Figure 3-4 Hysteresis in the cavity absorber: Coherency strains affect the relaxation of the absorption cavity mode and result in hysteresis.....	132
Figure 4-1 Optical coating absorbers based on a) lossy dielectric on a metal with high σ (OC1) where the absorption mainly takes place in the dielectric, and b) a lossless dielectric on low σ (OC2) where the absorption mainly takes place in the metal. In all cases, when the destructive interference condition is met, the reflected wave at the air-dielectric interface would have an equal magnitude to the sum of the partial waves reflected from the metal substrate. c) and d) show the calculated total power dissipated on OC1 and OC2 respectively. In OC1 the power is mainly dissipated inside the dielectric with some losses incurred in the metal, while in OC2 the power is entirely dissipated inside the metal.....	139
Figure 4-2 Reflectivity spectrum: Experimental Reflectivity spectra for S-polarized light for angles of incidence from 15°to 75° for an Ag film (left) and Ni film (right) coated with TiO2 thickness A) 20nm, B) 40nm, C) 60nm and D) 80 nm.....	142
Figure 4-3 Optical images of visible light absorbers: a) A glass slide with a 90nm Ni film coated with different thicknesses of TiO2 showing a variety of colors. b) Shows a frosted (roughened) glass substrate with a 90nm Ni film coated with 55nm (right) and 65nm(left) TiO2. The iridescent-free property of the optical coating allows maintaining color integrity even on a rough surface.....	143
Figure 4-4 Short wavelength IR absorber: [add the labels] Depositing an 80nm of Ge on a) Ag, and b) Ni substrates only result in light absorption for Ni substrate because Ge has low losses for energies below the NIR. The absorption maximum corresponds to 1700nm which means that the dielectric thickness is $< \lambda/4n$. This is possible because Ni does not behave as a PEC in the SWIR region.....	144
Figure 4-5 Oxidized metal thin-film absorber: a) Optical images of a Ni thin film that is heated on a hot plate showing a light-yellow, yellow, light-red, purple and blue colors. b) an SEM image of a cross-section in the yellow (top) and purple (bottom) films.....	145
Figure 4-6 Reflectivity measurements for oxidized metal absorber for the a) yellow, b) purple, and c) blue samples showing a wide angle range perfect light absorption.....	146

Figure 5-1 Schematic of the setup and sensor: a) A microfluidic channel is attached to the optical absorber and connected to two mass flow controllers (MFCs). One MFC controls the flow of nitrogen mixed with hydrogen (4% in concentration) and another MFC controls the flow of pure nitrogen. The sensor is then placed on a variable angle ellipsometer to measure the angular reflectivity. b) A schematic of the optical coating sensor. The microfluidic channel is attached to the top of the Pd film in order to expose Pd to the gas from the MFCs..... 151

Figure 5-2 Sensitivity for different angles of incidence: a) reflectivity measurements for the optical absorber before and after introducing hydrogen with C= 4% for three different incident angles 25° , 35° , and 45° . b) A contour plot for the reflectivity (color bar range 0-0.50 R) shows the angular reflection of the absorber. The FWHM increases significantly after introducing hydrogen for all incident angles..... 153

Figure 5-3 Sensitivity for different hydrogen concentration: a) Reflectivity of the absorber as a function of hydrogen concentration. b) Hysteresis in the shift in reflectivity minimum λ_{\min} 154

Abstract | ACTIVE PLASMONICS AND METAMATERIALS

MOHAMED ELKABBASH

The past two decades has seen considerable interest in Plasmonics and Metamaterials (**P & MM**); two intertwined fields of research. The interest is driven by matured nano-fabrication and characterization technologies and the limitations facing traditional photonics. While light cannot be *squeezed* beyond the diffraction limit, extreme light-matter interactions enabled the manipulation of light at length-scales much shorter than the wavelength of light. The prospects of plasmonics and metamaterials include subwavelength nano-photonics interconnects and circuits, light harvesting and solar energy, enhancement of linear and non-linear optical processes, sensing, ultrathin optical displays, structural coloring and quantum information and communication.

The field of plasmonics studies all aspects related to structures that can support plasmons; oscillations of free electrons in metals. From this perspective, one can consider plasmonics as the field of metal photonics that studies light-metal interaction in the optical range. Metals are not subject to the diffraction limit since light is confined by coupling to electron oscillations, or plasmons, in the metal. Electromagnetic (**EM**) field can thus be confined on length scales comparable to the dimensions of the metallic nanostructure. On the other hand, Metamaterials are engineered materials that enjoy optical properties and functionalities beyond what natural materials can provide. Usually metamaterials are composed of different materials or structures that interact with light resulting in an emergent property due to the interplay of all the component materials and/or structures.

In the optical range (visible and NIR), metamaterials heavily rely on metallic nanostructures as they allow for strong light-matter interaction at the sub-wavelength range.

The strong field localization, however, comes at a cost; electrons scatter and absorb the localized field at the femtosecond timescale. The problem of strong optical losses in plasmonics and metamaterials with metal components is the major obstacle in applications and devices that require high efficiency, e.g. perfect lenses, cloaking devices, and plasmonic transistors and interconnects. The confinement-loss tradeoff is what defines the future of P & MM [1].

As the field of plasmonics and metamaterials mature, the possible applications are adapting to the fundamental limitations of metal photonic materials. In addition to traditional, low efficiency applications of plasmonics, e.g., surface enhanced Raman spectroscopy (SERS), other applications that does not require high efficiency, e.g., metal enhanced fluorescence and plasmonic rulers are promising. Furthermore, losses can be desirable in applications that require strong light absorption and/or heat generation such as thermo-photovoltaics, solar energy generation, thermal emitters, optical absorbers and structural coloring, cancer photo-thermal therapy, and heat assisted magnetic recording.

Between low efficiency applications and applications where losses are desirable, one can envision a wide array of applications where the benefits of field confinement out-weigh the losses. In particular, an important consequence of strong field confinement is that changes in the surrounding EM environment can induce a strong change in the optical properties of a P & MM system. Such changes would result in an ultrafast, sub-nanosecond, response that can be useful in many applications. An active P & MM system is one where the existence of

an external mechanical, electrical, thermal or optical stimulus modifies the system's light-matter interaction.

This thesis aims to explore various active P & MM systems. To design an active system one needs first to create a passive system that enjoys a certain feature which is a function of the EM environment. By introducing a change in the EM environment, we obtain a measurable change in the passive feature. The first part deals with active plasmonics, particularly, gain-plasmon dynamics. We study the ultrafast dynamics of gain-plasmon interaction and reveal an active plasmonic system where the spontaneous emission rate of a quantum emitter is dynamically modulated. The main objective of this thesis is to slightly uncover the richness of P & MM *despite* the existence of strong losses and beyond the traditional or loss-based applications. The second part of the thesis deals with metamaterials that exhibit tunable, strong to perfect light absorption and their application in hydrogen gas sensing as an example for their optical activity.

[1] J. B. Khurgin, How to deal with the loss in plasmonics and metamaterials, *Nature Nanotechnology* 10, 2–6 (2015)

Active Plasmonics

In this part, we address our work on active-plasmonics. Chapter I provides a brief overview on plasmonics. A detailed treatment of plasmonics can be found in many textbooks and reviews [1, 2, 3, 4]. However, the chapter will cover the basic principles of three main plasmonic quasi-particles; propagating surface plasmon-polaritons, localized surface plasmon-polaritons, and bulk-plasmon polaritons. Afterwards, we will cover the origins of the active nature of plasmonic systems which are relevant to this thesis.

Gain-plasmon active systems are dealt with in Chapters II and III. Chapter II presents our work on the ultrafast transient optical loss dynamics in exciton-plasmon nano-assemblies. Previous studies attempted to prove the existence of plasmonic loss compensation using pump-probe spectroscopy. In this work, we provide a detailed study on the dynamics of compensating plasmonic losses with gain using femtosecond transient absorption pump-probe spectroscopy.

Chapter III presents our work on real-time, dynamic modulation of the spontaneous emission rate of gain resonantly coupled to a single plasmonic nano-cavity. We provide the first clear demonstration of the Plasmonic Dicke effect. We also show that it is possible to dynamically change the spontaneous emission rate of a quantum emitter at the sub-nanosecond level by changing the excitation intensity.

Chapter IV deals with plasmon-plasmon active systems. Here, the optical properties of a plasmonic nanoparticle is affected by the presence of other plasmonic nano-particles. We show that this can be used in creating tunable black gold.

Active Plasmonics: A brief background

Plasmonics is a relatively new term that describes the field dealing with all aspects related to the study, fabrication and applications of plasmon-supporting structures [1]. While the term plasmonics is new, the field itself is not as it is mainly concerned with the optical properties of metals, and in particular, noble metals like gold and silver. The rise of plasmonics as an independent and attractive field is due to the modern advances in nano-fabrication, nano-chemistry, high spatial resolution imaging techniques and high temporal resolution spectroscopy techniques. This is because many interesting emergent phenomena take place when the metallic structure is in the order of the wavelength of light i.e. the nano-scale. This chapter is divided into four sections: section 1, addresses the basics of the optical properties of metals. Section 2 is a brief introduction to plasmons and other quasi-particles that are associated with the optical excitation of plasmons. Section 3 deals with the different methods for optical excitation of propagating surface plasmon polaritons. Finally, section 4 provides an overview on the origins of the optical activity of surface plasmons.

1- Optical properties of noble metals:

Metals have a variety of distinguishing properties such as high reflectivity and good electronic and heat conductivity. The properties share the same physical origin; the presence of free conduction electrons. To a good approximation, the free electrons in a metal move and oscillate in a background of fixed positive ions. These free electrons,

accordingly, form plasma which is called solid-state plasma. The simplest model that deals with the optical properties of metals is the Drude model which ignores the existence of a restoring force. We will then consider the effect of inter-band transitions on the metal optical properties.

1.1- The Drude model:

The well-known Lorentz model describes the optical response of an electron bound with a restoring force characterized by a resonant frequency ω_0 . However, conduction electrons in a metal are, to a good approximation, not bound and can therefore be described by the Lorentz model without the restoring force (i.e. $\omega_0 \approx 0$); this is called the Drude model. Accordingly, the electric permittivity $\varepsilon(\omega)$ of a metal is given by

$$\varepsilon(\omega) = 1 - \frac{n e^2}{m \varepsilon_0} \frac{1}{\omega^2 + i \gamma_0 \omega} \quad (1)$$

, where n is the number volume density of free electrons, m is the free electron mass, γ_0 is the free electron collision rate (damping term) and for most noble metals it is relatively small compared to electron oscillation frequency ω . The response of the positive ions in the crystal can be included as a constant background with a real dielectric function $\varepsilon_\infty \geq 1$. Accordingly, the modified Drude model is given by

$$\varepsilon(\omega) = \varepsilon_\infty \left(1 - \frac{\omega_p^2}{\omega^2 + i \gamma_0 \omega} \right) \quad (2)$$

, where ω_p is the plasma frequency and defined as

$$\omega_p = \sqrt{\frac{n e^2}{m_e \varepsilon_0 \varepsilon_\infty}} \quad (3)$$

, where n is the electron number density, e is the electron charge and m_e is the electron mass. Taking the real and imaginary parts of the permittivity from equation 2, we get:

$$Re(\varepsilon(\omega)) = \varepsilon_\infty \left(1 - \frac{\omega_p^2}{\omega^2 + \gamma_0^2}\right) \quad (4)$$

, and

$$Im(\varepsilon(\omega)) = \frac{\varepsilon_\infty \omega_p^2 \gamma_0}{\omega(\omega^2 + \gamma_0^2)} \quad (5)$$

It is clear from the Drude model that if the plasma frequency is located in the UV, then the real permittivity of metals will be small and close to zero in the UV, then negative in the visible and very negative in the infrared which is the real behavior of most metals. The negativity of the real permittivity is the defining feature of metals in the optical range and is responsible for the high reflectivity of metals and most plasmon related effects.

1.2- Optical properties of real metals:

Drude model deals with electronic excitation within the conduction band , i.e., intra-band transitions. However, in real metals, additional processes can occur that contribute to the optical properties such as Landau damping [cite], and mainly inter-band transitions. Inter-band transitions are optical excitations of bound electrons to higher energy band which can be approximated as a collection of Lorentz Oscillators. The contribution of inter-band transitions $\varepsilon_b(\omega)$ adds to that of free electron contribution

$$\varepsilon(\omega) = \varepsilon_b(\omega) - \varepsilon_\infty \frac{\omega_p^2}{\omega^2 + i \gamma_0 \omega} \quad (6)$$

The presence of $\varepsilon_b(\omega)$ does not affect the optical properties of the metal strongly if the transition energy occurs in the UV range. For some metals, e.g., Au, where inter-band transitions are close to or below the plasma frequency the optical response of $\varepsilon_b(\omega)$ must be added. We will deal with Landau damping latter on when we describe the various causes of losses in plasmon-supporting systems in chapter II.

2- Plasmons et. al., a brief overview:

This section aims to provide an intuitive and brief overview on plasmons. First, we define plasmons and their nature, then we discuss optically excited plasmons (a.k.a. plasmon-polaritons). After that we will address several types of plasmon-polaritons of relevance to our work.

2-1 Plasmons:

A plasmon is a quantum quasi-particle representing the elementary excitations of the charge density oscillations in a plasma. A plasmon is therefore simply to the plasma charge density what photons are to the electromagnetic field [1]. This definition correctly reflects the quantum nature of plasmons. However, in practice, the term plasmon is used loosely to identify its classical analogue where we mean charge density oscillation wave. These charge density oscillations are longitudinal in nature. A transverse wave where the propagation and oscillation directions are orthogonal will not create any macroscopic charge density oscillations (See Fig. 1). Mathematically, a longitudinal electromagnetic mode is when $\mathbf{E} \parallel \mathbf{k}$ and $\mathbf{E} \times \mathbf{k} = \mathbf{0}$ and $\nabla \times \mathbf{E} = \mathbf{0}$, while a transverse electromagnetic mode is when $\mathbf{E} \perp \mathbf{k}$ and $\mathbf{E} \cdot \mathbf{k} = \mathbf{0}$, and $\nabla \cdot \mathbf{E} = \mathbf{0}$. The plasmon can either propagate inside the bulk of the metal, i.e., bulk (volume) plasmon or bound to its surface, i.e., surface plasmon. In metals, the lack of internal free charge

density always ensures that $\nabla \cdot \mathbf{D} = 0$, where D is the displacement field. This necessarily means that any longitudinal electric field will always be zero unless the permittivity is zero. In such case, it is possible to excite a longitudinal electric mode inside the bulk, i.e. a bulk plasmon. This mode is excited only at the plasma frequency (where $Re(\epsilon(\omega)) = 0$). However, because of the transverse nature of photons, these modes, in general, cannot be optically excited. It is possible for p-polarized light at higher angles of incidence to excite such modes in metals; these modes are known as Ferrel-Berremen modes [5].

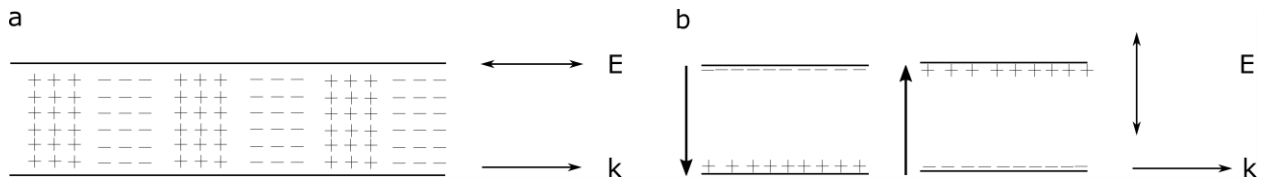


Figure 1 Charge density oscillation driven by a) longitudinal, b) transverse electric field. A net macroscopic charge density oscillation is only possible with a longitudinal field.

2-2 Plasmon-polaritons:

Strictly speaking, a photon corresponds only to an electromagnetic wave in vacuum, and it becomes a polariton in any media. A polariton is a quasi-particle that results from a photon coupling strongly to a magnetic or electric dipole excitation. When the electric dipole excitation is a plasmon, the resulting hybrid quasi-particle is a plasmon-polariton. For such a hybrid particle to exist, the energy is shared between the two oscillators; the photon and the plasmon. The hybridization results in level repulsion that manifests itself as anti-crossing of the plasmon frequency and the electromagnetic mode dispersion [see Fig. 2] [6].

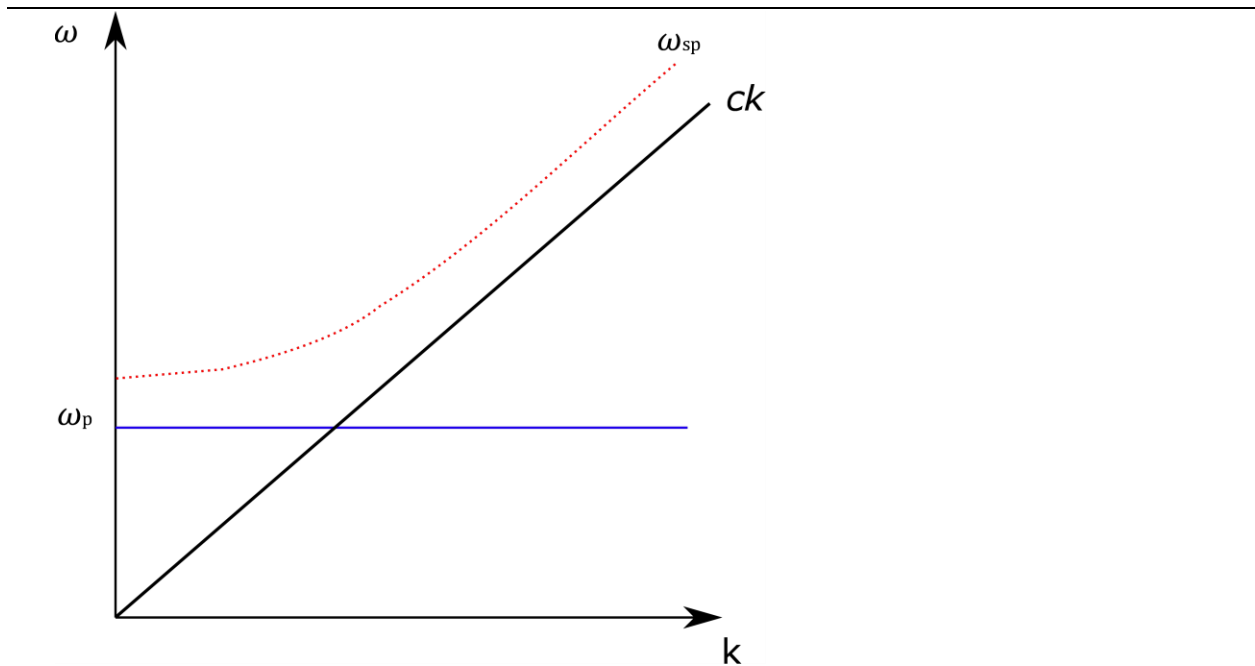


Figure 2| The dispersion ω_{sp} (red dotted line) for surface plasmon propagation in a Drude metal appears to result from avoided crossing between the plasmon frequency ω_p (blue line) and the light line $\omega = ck$ (black line).

2-3 Surface plasmon-polaritons:

For a metal-dielectric interface, there exists a non-zero surface charge density at the boundary. This entails that the existence of an electric field component at the interface is possible even for non-zero metal permittivity. However, in order to obtain a longitudinal mode where \mathbf{E} and \mathbf{k} are parallel, the incident field must be transverse magnetic (TM) field. This is because only a TM polarized wave has a non-zero component that is parallel to the wave-vector at the interface [see fig. 3]. This longitudinal electromagnetic mode at the surface of a metal-dielectric interface is called surface plasmon-polariton (SPP) which indicates that the electromagnetic energy is shared between a photon and a plasmon oscillating at the metal-dielectric interface.

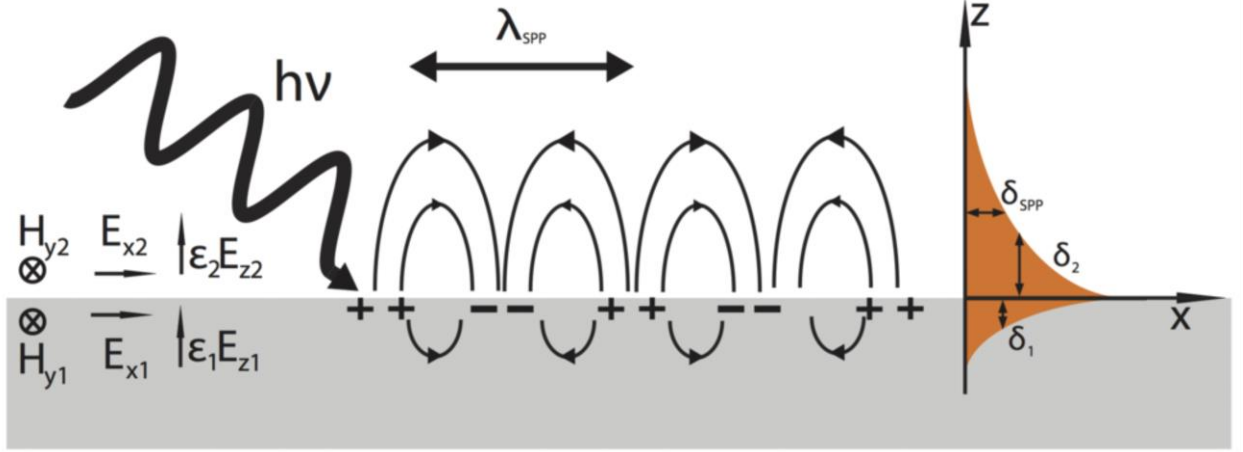


Figure 2: Schematic of propagating SPP. A TM polarized light can excite a propagating surface mode that is evanescently decaying in the transverse direction as well as in the propagation direction due to the existence of losses in metal.

Furthermore, for a given frequency ω the wave-vector component along the interface k_x should satisfy the momentum of the excited surface wave k_{sp} given by

$$k_{sp} = \frac{\omega}{c} \sqrt{\frac{\varepsilon_M \varepsilon_D}{\varepsilon_M + \varepsilon_D}} \quad (7)$$

, where ε_M and ε_D are the complex metal and dielectric permittivity respectively. For $\varepsilon_M < 0$ and $\varepsilon_D > 1$, then $\sqrt{\frac{\varepsilon_M \varepsilon_D}{\varepsilon_M + \varepsilon_D}} > 1$ and $k_{sp} > k_x$ under any conceivable illumination angle. According to the time reversal symmetry of Maxwell's equations, such electromagnetic mode is non-radiative (dark) as it cannot couple to (from) far-field radiation. Because $Im(\varepsilon_M) \neq 0$ in equation 7, k_{sp} is also complex and the SPP should decay evanescently in the direction of propagation. The propagation length is given by

$$\frac{1}{L_{sp}} = 2 Im k_{sp} = \frac{\omega}{c} \frac{\varepsilon_1^{\frac{3}{2}} \varepsilon_2(\omega)}{|\varepsilon_1(\omega)|^{\frac{1}{2}} (|\varepsilon_1(\omega)| - \varepsilon_1)^{\frac{3}{2}}} \quad (8)$$

, and the dispersion of the propagating SPPs (PSPPs)

$$\omega_{sp} = \frac{\omega_p}{(1 + \epsilon_D)^{1/2}} \quad (9)$$

Here, we would like to point out that the momentum mismatch with the far field radiation is *not a property* of surface plasmon-polaritons, rather a *condition* for its existence under general illumination conditions since SPPs are bound mode. A bound mode is one that can exist even in the absence of the incident wave. A non-bound mode (a.k.a. incident wave mode), however, requires the existence of an incident wave. For a bound electromagnetic mode between two mediums to exist (Fig. 3), the field cannot transmit or reflect in either media. For instance, an electromagnetic wave propagating in a dielectric sandwiched between two other dielectrics can be bound if it is evanescent in both media which requires that the mode satisfies the condition of total internal reflection (TIR) in both media. This forms an all-dielectric waveguide used in optical fibers. Such TIR necessarily mean that the momentum of the bound mode is mismatched with momentum in both media. For a metal-dielectric interface, it is possible to obtain a bound mode at the interface because the metal surface screens the electromagnetic field and the field is naturally evanescent inside the metal. However, for the dielectric medium, the mode can only be bound if it experiences TIR at the dielectric interface which requires momentum mismatch otherwise it will simply reflect off of the metal layer.

On the other hand, some surface plasmon-polaritons can be excited radiatively if the dielectric medium consists of a photonic crystal at its stop band (Tamm plasmon-polaritons or TPPs) or the dielectric is sandwiched between two metal films and is thin

enough for the SPP modes supported by each metal-dielectric interface strongly couple (gap-SPP). For TPPs and gap-SPPs, light has to tunnel through one metal interface which must be thin enough to allow for some light transmission. The radiative nature of these propagating modes mean that the SPP will eventually tunnel back through the thin metal layer and leak to the far field. Accordingly, PSPP is not necessarily a dark mode, and can exist even without momentum mismatch with the incident wave.

Another way to create a longitudinal bound mode is to have a bound surface, i.e., a surface with features smaller than or equal to the incident wavelength such that its thickness in the localization direction is smaller than the metal skin depth (See fig.4). In this case, the mode is bound because the surface is spatially bound [3]. For a spherically bound surface, e.g., a nano-particle, the charge oscillation should be periodic which quantize the field variation [3]. For a metallic sphere these modes correspond to spherical harmonics with solutions representing the localized SPP (LSPP) frequencies ω_l given by

$$\omega_l = \omega_p \left(\frac{l}{\epsilon_D (l+1) + l} \right)^{1/2}, \quad l = 1, 2, 3, \dots \quad (10)$$

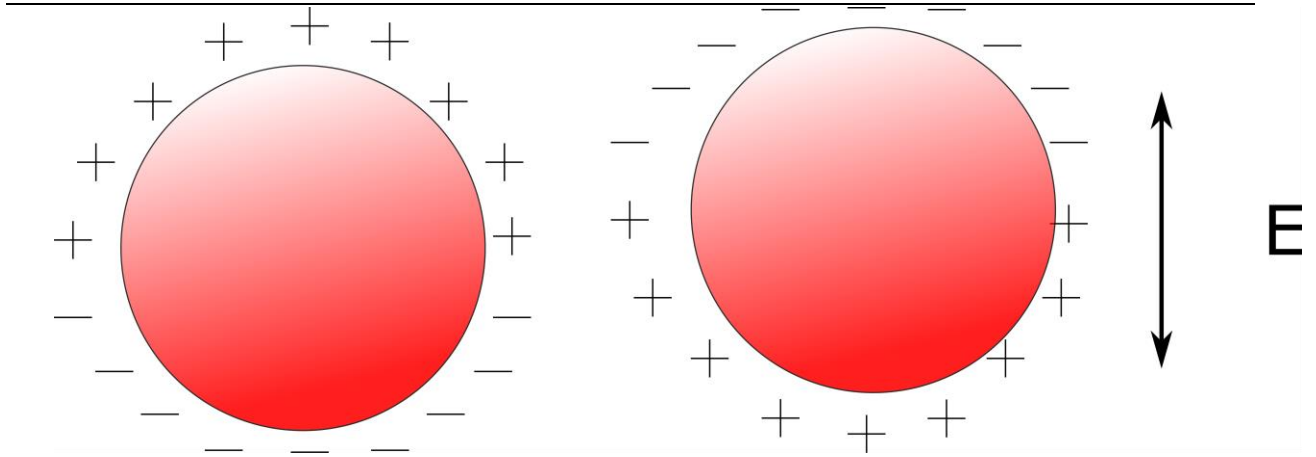


Figure 3| Localized surface plasmon resonance: Metals with bound surface, i.e., with features smaller or similar to the incident wavelength, can support radiative bound modes. These modes correspond to standing electromagnetic waves coupled to charge density oscillations. For small spheres, the most prevalent mode is the dipolar mode depicted in the figure.

For small spheres, only the dipole term ($l = 1$) is important. As the size of the sphere increases, contributions from higher multipoles start to become significant [2]. It is interesting to note that for $l \rightarrow \infty$, $\omega_l \rightarrow \omega_{sp}$ which highlights the aforementioned assertion that a bound surface creates a bound mode and both LSPP and PSPP are manifestation of the same phenomenon.

The depolarization field E_{pol} inside the particle for an incident field E_0 is then [4]

$$E_{pol} = \frac{\epsilon_D - \epsilon_M}{\epsilon_M + 2\epsilon_D} E_0 \quad (11)$$

Accordingly, for a metallic spherical nanoparticle with radius a absorption cross-section σ_{abs} is given by [3]

$$\sigma_{abs} = 4\pi k a^3 \text{Im} \left(\frac{\epsilon_D - \epsilon_M}{\epsilon_M + 2\epsilon_D} \right) \quad (12)$$

and the scattering cross-section σ_{Sc} is

$$\sigma_{Sc} = \frac{8}{3} \pi k^4 a^6 \left| \frac{\varepsilon_D - \varepsilon_M}{\varepsilon_M + 2\varepsilon_D} \right|^2 \quad (13)$$

The absorption cross-section scales with the volume. The scattering, however, scales with the volume squared since it requires absorbing and re-emitting light [3]. Considering that for most dielectrics $Im(\varepsilon_D \approx 0)$, σ_{Sc} is a maximum when $Re(\varepsilon_M + 2\varepsilon_D) \approx 0$ and it does not diverge since the $Im(\varepsilon_M + 2\varepsilon_D) \approx Im(\varepsilon_M) \ll 0$. In addition, $Re(\varepsilon_M + 2\varepsilon_D) \approx 0$ corresponds to enhanced field confinement according to equation 11. The quantization of the field confinement (boundedness) for LSPs makes them effectively an open leaky cavity. The leakiness of such cavity is because LSPs are radiative modes. However, such cavity differs from traditional cavities since it localizes the field at length scales much smaller than the resonant wavelength. For a traditional cavity, the cavity confinement length a cannot be smaller than half the optical length of the confined wavelength λ , (i.e., $a \geq \lambda/2 n$), where n is the cavity refractive index. This is important in order to allow for self-sustaining oscillation by maintaining the energy balance between the energy stored in the electric and the magnetic fields. For a given frequency ω , the cavity confinement length must allow for the electric (magnetic) field at $(\omega t = 0)$ to create its magnetic (electric) field counterpart at $(\omega t = \pi/2)$. For a plasmonic nano-particle (NP), the plasmon resonances correspond to standing waves just like a cavity. However, the dimensions of the NP need not to be $\geq \lambda/2 n$ because some of the energy stored in the electric field can be transferred partially to the kinetic energy of freely oscillating electrons and partially in the magnetic field and the energy

balance is restored. This confinement is maximized when the response of the free electrons is maximum, i.e., at resonance.

3- Optical excitation of propagating surface plasmon-polaritons:

The excitation of a bound PSPP at a metal-dielectric interface requires a momentum coupler, i.e., a method by which the momentum matching condition is satisfied. There are several methods that enable momentum matching, however, they share two main mechanisms; momentum matching via photonic tunneling and via diffraction.

3-1 Momentum matching via diffraction:

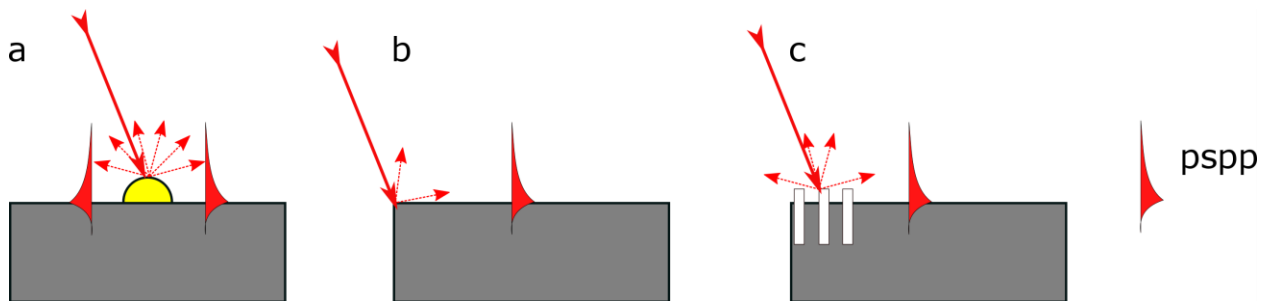


Figure 4| Excitation of propagating SPP via diffraction: a) A scatterer can diffract incident light to a continuum of scattered waves with different momenta. Some components can launch circular SPPs centered at the scatterer. **b)** Irradiating the edge of a metal strip scatters light where some components of the scattered light excite an SPP away from the edge. **c)** Using a diffraction grating, only certain momentum components are generated, if one of them matches the SPP momentum for a given angle, an SPP is launched in the direction of transverse to the grating

One way to add momentum to an incident wave is via diffraction. The simplest way to do so is to diffract light on a surface feature or using a scatterer (Fig 5a). Although using randomly distributed scatterers does not require any special arrangements, this method is hardly used since the diffracted components, in the near field, have all possible wave-vectors (momenta). Given that propagating SPP is not a resonant excitation, the SPP excitation condition with random scatterers becomes ill-defined. Furthermore, the existence of a scatterer affects the propagation of an already excited SPP; It can either a) scatter a PSPP into a PSPP propagating another direction (SPP

scattering), b) propagate in the same direction (SPP transmission) or c) scattering PSPP into light (out-coupling).

Another way to diffract light is to irradiate an edge of a metal strip (Fig.5b), an advantage of this method is the strong presence of the evanescent field at the smooth part of the metal film. However, it is generally difficult to target the edge of the metal strip.

Perhaps the most common diffraction-based method is using a diffraction grating (see Fig. 5c). If a diffraction grating is created on part of a smooth metal film, components of the diffracted light whose momentum matches the SPP momentum will be coupled to SPPs. Formally this condition is satisfied when

$$\mathbf{k}_{sp} = \frac{\omega}{c} n_D \sin \theta \mathbf{u}_{12} \delta_p \pm p \frac{2\pi}{\Lambda} \mathbf{u}_1 \pm q \frac{2\pi}{\Lambda} \mathbf{u}_2 \quad (14)$$

, where $\delta_p = 1$ for p-polarized incident light and 0 for s-polarized light, \mathbf{u}_{12} is the unit vector in the direction of the in-plane component of the wavevector of the incident light, n_D is the refractive index of the medium through which the film is illuminated, \mathbf{u}_1 and \mathbf{u}_2 are the unit lattice vectors of a periodic structure, Λ is its period (assumed to be the same in both the x_1 -and x_2 -directions), and p and q are integer numbers corresponding to the different propagation directions of the excited SPPs. Because of the well-defined excitation condition, this method is very efficient in exciting SPPs. Note that the grating can also out-couple the excited SPP into light which limits the PSPP excitation efficiency.

3-2 Momentum matching via tunneling:

For total internal reflection (TIR) to take place, momentum must be mismatched between the two media at the reflection interface. For that reason, the incidence medium must have a higher refractive index such that it has a set of values that cannot be matched in the lower index medium ($n_1 > n_2$). In such case, the field is evanescently decaying away from the incidence medium (Fig. 6a) and extends spatially in the order of the incident wavelength. The evanescent field transmits zero net energy across the interface. However, if a third medium with higher refractive index n_3 or that supports a bound wave with matched momentum is present *within* the spatial range of the evanescent field, energy can tunnel through the low index medium (Fig. 6b). This is called evanescent wave coupling and in the context of TIR is called frustrated TIR.

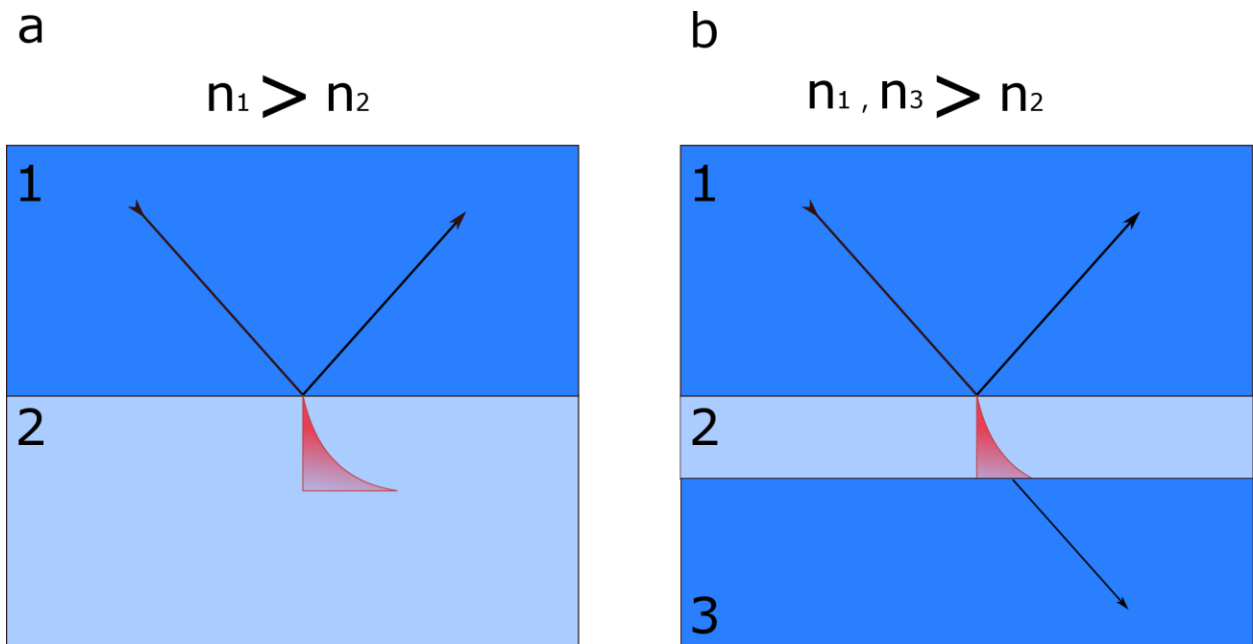


Figure 5| TIR and frustrated TIR: **a)** Light incident from a medium with a given refractive index on another with lower refractive index can experience TIR. The field only evanescently decay inside the lower index medium. **b)** If a third medium with a refractive index higher than that of medium 2, the field is no longer evanescent in 3 and energy can propagate.

With that in mind, any system that can produce an evanescent field due to TIR is capable of exciting an SPP. For instance, light incident on a prism above the prism critical angle is capable of exciting an SPP ($\theta_{sp} \geq \theta_c$) where $k_{sp} = k_0 n \sin \theta_{sp} \sqrt{\epsilon_{Prism}}$. Clearly it is not possible to excite an SPP at the metal-prism interface since the momentum is already matched inside the prism. Accordingly, a PSPP can be excited at another metal-dielectric interface such that $n_D < n_{prism}$. There are three known configurations to do so. The Kretschmann configuration where light tunnels through a thin metal film and excites an SPP at the metal-dielectric interface (Fig. 7a). The double Kretschmann configuration where a spacer layer with refractive index n_1 is deposited between the prism and the metal (Fig. 7b). Two SPPs can be excited one at the metal dielectric I interface and another at the metal dielectric II interface. In both Kretschmann configurations, the metal film must be optically thin as to allow for light to tunnel through it in order to excite an SPP. Finally, there is the Otto configuration where a spacer is located between the prism and an optically thick metal film (Fig. 7c). Clearly, the SPP is excited at the metal-spacer interface.

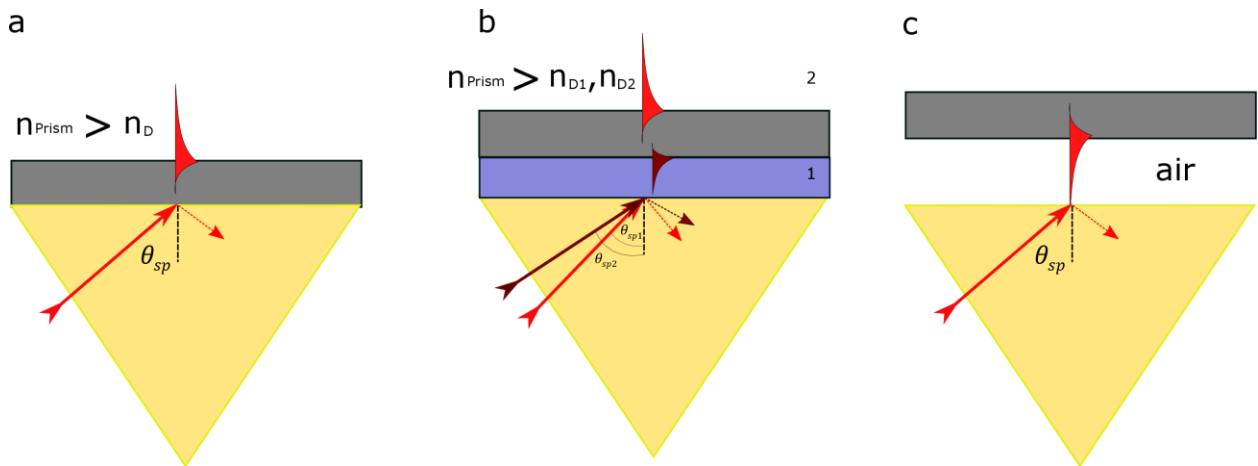


Figure 6| Excitation of SPP via tunneling using a prism: a) The Kretschmann configuration; light incident at an angle $\theta_{sp} \geq \theta_c$ experiences TIR. The field tunnels through a thin-metal film and excites an SPP at the metal-dielectric interface with refractive index n_D if $n_{Prism} > n_D$. **b)** The double-Kretschmann configuration; by adding a dielectric spacer with

refractive index $n_{\text{Prism}} > n_{\text{D1}}$ it is possible to excite an SPP on both sides of the metal thin-film. **c)** The Otto configuration; a spacer dielectric layer, usually air, between a prism and a thick metal layer allow for SPP excitation at the metal-air interface.

Although exciting an SPP using a prism is a popular method, this method is conceptually similar to exciting an SPP using other unconventional methods. It is possible, for instance, to excite an SPP using a highly focused optical beam using an oil-immersed objective. If the numerical aperture of the objective is large enough, then the focused beam has large angular spread. Accordingly, some of its components will experience TIR and will excite SPPs [4].

A beam focused beyond its diffraction limit using a metallic tip can also be used to excite SPPs; this is called near-field excitation which is a mixture of excitation by tunneling and diffraction. The near-field of the tip naturally has evanescent modes that will not couple in the far-field and can satisfy the SPP excitation condition. Similar to that method, any dipole (antenna) is capable of exciting an SPP via its near-field. Accordingly, quantum emitters, close to a metal surface, are capable of exciting SPPs via their near-field.

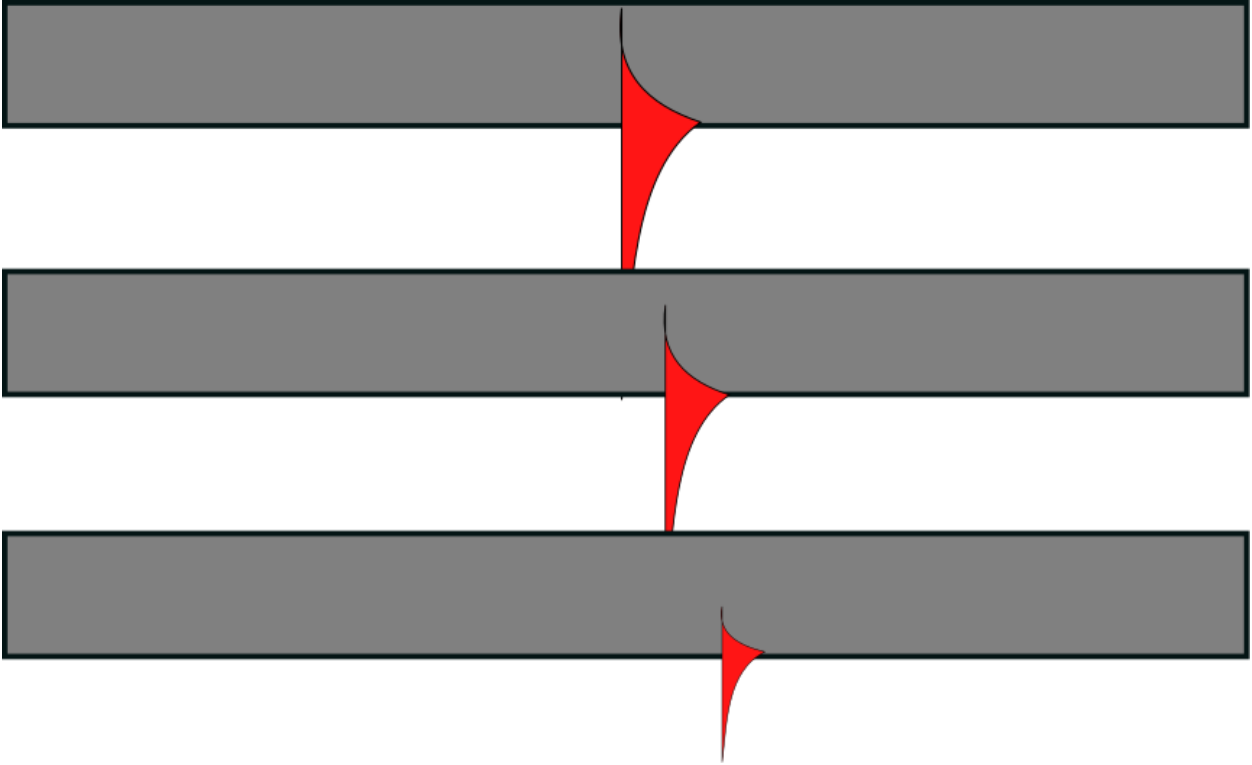


Figure 7|Excitation of SPP with an SPP: A PSPP is evanescent in the direction orthogonal to its propagation as it experiences TIR at the metal-dielectric interface. Placing a metal thin-film within the spatial range of the evanescent field allows for exciting another PSPP. A metal-dielectric thin film stack can support multiple PSPP excitations.

A very interesting case is exciting a PSPP using another propagating SPP. As we discussed earlier, a PSPP cannot propagate in the far-field in the dielectric medium unsolicited because it experiences TIR, i.e., it is a bound mode. Instead the field evanescently decays in the dielectric medium away from the surface. This means that the existence of another metal layer within the range of the evanescent field can frustrate the TIR and allow for exciting another SPP at the other metal-dielectric interface. One can further extrapolate and imagine a stack of metal-dielectric layers where each metal layer supports an SPP that is capable of exciting another SPP in the metal layer(s) underneath it (Fig. 8). In such case, the proper treatment of such system should consider a pseudo-propagating mode in the direction orthogonal to the propagation direction of the SPP. Naturally, this system is behaving as a metal in the

plane of propagation of the PSPP (i.e., $\epsilon_{\parallel} < 0$). However, since it supports a propagating wave in the orthogonal direction (bulk) of the metal-dielectric stack, its permittivity must be dielectric-like in the bulk (i.e. $\epsilon_{\perp} > 0$). The fact that the permittivity parallel and orthogonal to the plane of incidence have opposite signs means that the medium dispersion is hyperbolic. Unlike the conventional ellipsoidal dispersion (Fig. 9a) where the permittivity shares the same sign in all directions, hyperbolic dispersion allows for infinitely high momenta, in the effective medium approximation, which correspond to slow group velocity and high local density of photonic states (LDOS). The dispersion of a material with $\epsilon_{\perp} > 0$ and $\epsilon_{\parallel} < 0$ is a type II hyperbolic dispersion (Fig. 9c).

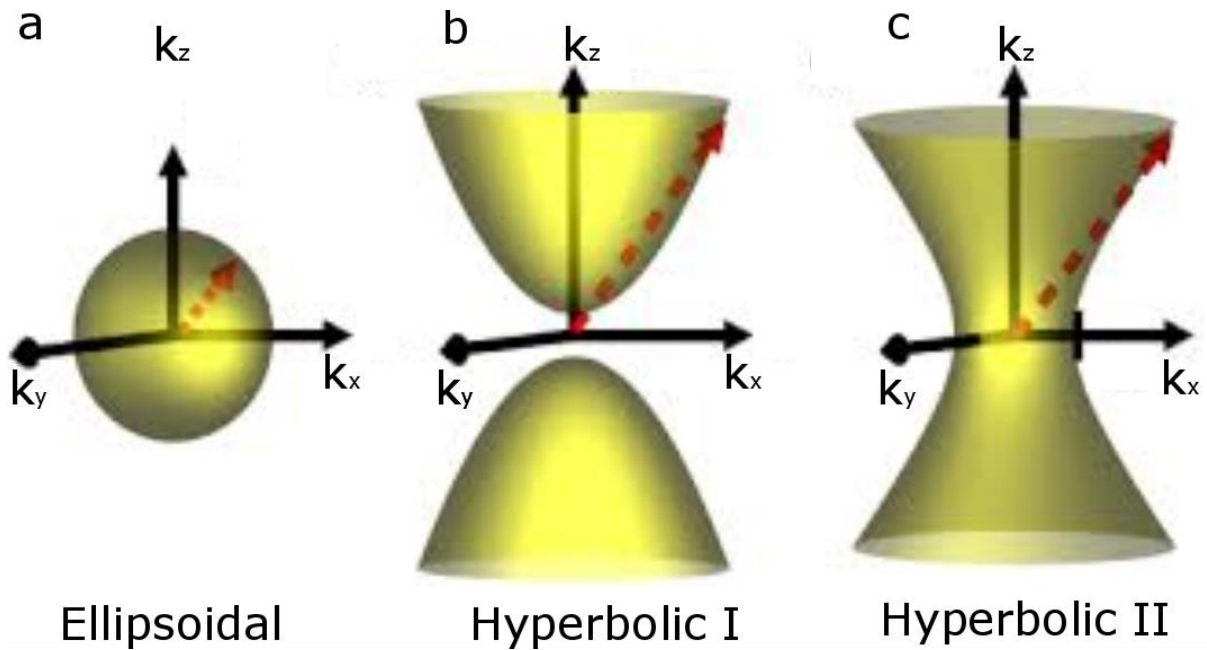


Figure 8| Ellipsoidal and hyperbolic dispersions: a) The dispersion of a conventional material with permittivity sharing the same sign in all three basis directions forming an ellipsoidal dispersion. b) If the permittivity in the orthogonal direction is negative while in the parallel direction is positive, the system has a type-I hyperbolic dispersion. c) If the permittivity in the orthogonal direction is positive while in the parallel direction is negative, the system has a type-II hyperbolic dispersion

Another possible medium with a type I hyperbolic dispersion is when $\epsilon_{\parallel} > 0$, and $\epsilon_{\perp} < 0$ (Fig. 9b). One way to realize type I hyperbolic dispersion is using metallic out-of-plane nano-rods embedded in a dielectric matrix. These rods can support SPPs

propagating in the bulk while maintaining an effective dielectric behavior in the plane of incidence.

4- Active Plasmonics; the origins:

Active plasmonics refer to plasmonic systems that change their optical properties in response to external stimuli. Now that we are equipped with a general understanding of surface plasmons and other closely related systems, we can clearly see the origins of such optical activity. Equations 3, 7, 9, 10, 11, 12, and 13 include the basis for most active plasmonic systems. We will approach the subject of active plasmonics by addressing each parameter responsible for modulating the optical properties of surface plasmons.

4-1 Activity based on modulating ϵ_D :

Just like the plasmonics, the term active plasmonics came into existence decades later after it found widespread applications. In the 1980s SPPs were introduced as highly sensitive refractometers that are capable of sensing changes in the surrounding medium refractive index which was translated into bio(chemical)-sensors [7]. The change in ϵ_D of the surrounding dielectric is an external stimulus that results in a change in ω_{sp} for PSPPs (Equation 9), and ω_l for LSPPs (Equation 10). While an SPP-sensor is, strictly speaking, an active system, the field of active plasmonics goal is to gain control over the stimulus as well in order to modulate the SPP at will. The first true active-plasmonic system was introduced in 2004 [8], where a PSPP was excited via a grating to propagate on a smooth metal film and later decoupled to far-field radiation via another grating. The smooth metal layer is covered by a gallium layer. The dielectric permittivity is controlled by thermally driving reversible phase-changes in gallium.

Similarly, for LSPPs, the plasmon resonance can be actively tuned by changing the optical constant of the surrounding dielectric which can be done, for example, electrically [9], or by using phase-change materials [10].

4-2 Activity based on modulating ϵ_M :

The permittivity of a metal supporting SPPs can be modified by irradiating the metal with a high intensity laser (e.g., pulsed laser) in order to change the electron occupancy of the metal. When free electrons absorb the incident wave, intra-band transitions take place which change the electron occupancy. Over few hundred femtoseconds, electron-electron scattering takes place which thermalize the electron sea retrieving their Fermi-Dirac distribution, however, at a higher Fermi energy. Below the Fermi energy, there will be more vacant states. Subsequent transitions into these vacant states become more likely [11]; this corresponds to an increase in the imaginary part of the permittivity, leading to a change to the real part of the permittivity according to Kramers-Kronig relations. The thermalized electrons then cool down via electron-phonon scattering (picosecond timescale). The thermalized lattice is then cooled down via phonon-phonon scattering (nanosecond timescale). The femtosecond response and picosecond decay of electron thermalization (and modification of ϵ_M) makes this method very interesting for “ultrafast” modulators especially that it can be done all-optically [12,13].

The change in ϵ_M , naturally affects PSPPs and LSPPs. From equation 7, k_{sp} depends on ϵ_M . Accordingly, any change in ϵ_M would result in a change in the phase matching condition for exciting a PSPP [14]. Interestingly, using an unpatterned metal thin-film it is possible to create a transient grating by patterning the incident pulsed laser beam via

interference on the metal surface which would allow the excitation of SPP for a probe beam [15]. In this case, the activity is not coming from changing the dispersion of the SPP, rather changing the excitation condition which is still not a well explored area. For instance, one can imagine using a grating or a prism momentum coupler and change their optical constants instead of the optical constants of the dielectric or the metal at the interface where the SPP propagates.

4-3 Activity based on modulating ω_p :

Equations 9 and 10 show that both ω_{sp} , and ω_l depend on ω_p ; the plasma frequency. The plasma frequency depends on two parameters that can be modulated; the electron number density n and electron effective mass m_e . Both the n and m_e are affected by direct optical excitations to the metal supporting the SPP. The electron carrier density can be altered via inter-band transitions, which would result in a change in ω_p and red-shifts the plasmon resonance [12]. Note that inter-band transitions also have a similar effect to intra-band transitions in terms of modifying the metal's permittivity [11]. A more relevant effect is changing the electron effective mass m_e via optical excitations. This effect is significant in metals with non-parabolic dispersion relations. In general, the free electron assumption in metals is a mere approximation since it ignores any interaction between the electrons and the potential created by the crystal lattice of the metal. For free electrons, the electron energy is equivalent to its kinetic energy $E = (\hbar k)^2 / 2 m_e$, this leads to a parabolic dispersion relation. The inverse of the effective mass is proportional to the curvature of the dispersion curve and having a parabolic dispersion ensures that it is a constant. Optically excited electrons would lie at a different point in the dispersion curve. If the dispersion is parabolic, m_e will remain

unchanged. If the dispersion, however, is non-parabolic, then excited electrons will have considerably different m_e and the plasma frequency will change significantly. An example of metals with non-parabolic dispersion is conductive metal oxides (CMOs). Recent works have exploited this property of CMOs in ultrafast modulation of the spectral location of LSPPs [12], and in creating a femtosecond polarization switch [13].

4-4 Activity based on introducing optical gain:

Introducing gain to the dielectric environment of a plasmonic system yields interesting and, somewhat, complicated interactions. Although we can trace back the effect of gain into modifying ϵ_D introduced in section 4-1, we prefer to deal with active gain-plasmon systems separately. The language we will use in order to describe gain-plasmon interactions is that of non-radiative resonant energy transfer (RET). The RET condition is satisfied when the emitter emission spectrally overlaps with the PNC surface plasmon resonance. The energy transfer is a dipole-dipole energy transfer, similar to FRET, where the gain decays and creates a surface plasmon, i.e., the gain is weakly coupled to the LSPP. The LSPP, then, can either decay into a photon or it can be absorbed. In case of photon emission, the LSPP emission rate is higher than that of the emission rate of a quantum emitter and the result is enhanced spontaneous emission rate [16]. Another consequence of RET is compensating the losses of the plasmonic cavity. The loss compensation is translated into enhanced scattering and transmission. The enhanced scattering can be seen by investigating equation 13. The enhanced scattering cross-section in a passive plasmonic cavity occurs when the real part of the denominator in equation 13 goes to zero, i.e., $Re(\epsilon_M + 2\epsilon_D) = 0$. The scattering, however, diverges completely when both the real and imaginary parts approach zero. Because the

imaginary component of gain is opposite in sign to that of the metal it is possible to satisfy both conditions, i.e., $Re(\epsilon_M + 2\epsilon_D) = Im(\epsilon_M + 2\epsilon_D) = 0$. The transmission of a plasmonic system following loss compensation should also increase. The transmittance of a certain medium with an effective complex refractive index $n = n' + in''$ is given by [17],

$$T = e^{-\alpha x} \quad (15)$$

where x is the medium thickness and α is the attenuation coefficient which in turn is related to the extinction coefficient, i.e., the imaginary part of the *effective* refractive index according to the following relation

$$\alpha = \frac{2 \omega n''}{c} \quad (16).$$

For metallic inclusions in a gain medium, the effective imaginary index of refraction diminishes substantially allowing for enhanced transmission in the case of an active medium.

4-5 Activity due to plasmon hybridization:

Earlier we considered the possibility to excite a PSPP via another PSPP. The coupling between the two PSPPs is weak coupling since the energy is tunneled from one PSPP to another. However, in some cases, two SPPs (localized or propagating) strongly couple and result in a distortion in the dispersion (for PSPPs) or resonance frequencies (for LSPPs) due to the hybridization between the two oscillators. This is a frequently omitted, yet possibly impactful, mechanism to achieve optical activity in plasmonic systems, i.e., plasmon induced activity. For the purposes of this thesis, we are interested

in the plasmon hybridization of LSPPs. For two identical NPs with plasmon resonance ω_l that couple strongly with an interaction energy between the different multipolar l and azimuthal m angular components ($U_{lm,lm}$), the resulting symmetric ω_- and antisymmetric ω_+ solutions are given by [3]

$$\omega_{\pm}^2 = \omega_l^2 \pm \frac{|U_{lm,lm}|}{2} \quad (17)$$

For dipole-dipole interaction, the symmetric mode corresponds to in-phase dipole oscillation between the two nano-particles and according to equation 17 it occurs at lower frequencies. On the other hand, the antisymmetric mode corresponds to the out-of-phase dipole oscillations and occurs at a higher energy. However, only the in-phase oscillation is detectable in the far-field since the out-of-phase mode cancel out. Accordingly, plasmon hybridization between two LSPPs results in a red-shift in the plasmon resonance. One application of plasmon-induced activity is

References:

- [1] E. Le, R. Pablo Etchegoin, Principles of Surface-Enhanced Raman Spectroscopy, 1st edition. Elsevier Science, 2008.
- [2] A. Zayats, I. Smolyaninov, A. A. Muradudin, Nano-optics of surface plasmon polaritons, Volume 408, Issues 3–4, Pages 131-314, 2005.
- [3] M. Pelton, G. W. Bryant, Introduction to Metal-Nanoparticle Plasmonics, Wiley, 2013.
- [4] S. A. Maier, Plasmonics: Fundamentals and Applications, Springer Science & Business Media, 2007.
- [5] W. D. Newman, C. L. Cortes, J. Atkinson, S. Pramanik, R. G. DeCorby, Z. Jacob. Ferrell–Berreman Modes in Plasmonic Epsilon-near-Zero Media, ACS Photonics, 2 (1), 2015.
- [6] M. Sukharev, A. Nitzan, Optics of plasmon-exciton nanomaterials, Journal of Physics: Condensed Matter, 2017.
- [7] L. Cao, M. L. Brongersma, Active Plasmonics: Ultrafast developments, Nature Photonics 3, 12 – 13, 2009.
- [8] A. V. Krasavin, N. I. Zheludev, Active plasmonics: Controlling signals in Au/Ga waveguide using nanoscale structural transformations. Applied Physics Letters, 84, 1416 –1418 (2004).
- [9] T. B. Hoang, M. H. Mikkelsen, Broad electrical tuning of plasmonic nanoantennas at visible frequencies , , Applied Physics Letters , 108 , 18 , 183107, 2016.
- [10] Y. Abate, R. E. Marvel, J. I. Ziegler, S. Gamage, M. H. Javani, M. I. Stockman, R. F. Haglund, Control of plasmonic nanoantennas by reversible metal-insulator transition Scientific Reports, 5, 13997, 2015.

-
- [11] S. Link, M. A. El-Sayed, Spectral properties and relaxation dynamics of surface plasmon electronic oscillations in gold and silver nanodots and nanorods, *The Journal of Physical Chemistry B*, 103 ,40, Pages 8410-8426, 1999.
- [12] P. Guo, R. D. Schaller, J. B. Ketterson, R. P. H. Chang, Ultrafast switching of tunable infrared plasmons in indium tin oxide nanorod arrays with large absolute amplitude. *Nature Photonics*. 10, 267–273 (2016).
- [13] Y. Yang, K. Kelley, E. Sacht, S. Campione, T. S. Luk, J.,-P., Maria, M. B. Sinclair, I. Brener, Femtosecond optical polarization switching using a cadmium oxide-based perfect absorber . *Nature Photonics*, 11, 390–395 (2017).
- [14] K. F. MacDonald, Z. L. Sámsón, M. I. Stockman , N. I. Zheludev, Ultrafast active plasmonics, *Nature Photonics* 3, 55 - 58 (2009).
- [15] N. Rotenberg, M. Betz, H. M van Driel, Ultrafast control of grating-assisted light coupling to surface plasmons, *Optics letters* , 33 , 18 , 2137-2139, 2008.
- [16] M. Pelton Modified Spontaneous Emission in Nanophotonic Structures. *Nature Photonics*. 9, 427–435, 2015.
- [17] J. H. Simmons, K. S. Potter, *Optical Materials*, Academic Press, 2000.

Ultrafast transient optical loss dynamics in exciton-plasmon nano-assemblies

In this chapter, we study the exciton-plasmon dynamics that lead to optical loss mitigation via ultrafast transient absorption spectroscopy (UTAS) on hybrid aggregates of core-shell quantum dots (QDs) and Au nanoparticle (NP). We highlight that generating hot electrons in plasmonic NPs contribute to the transient differential absorption spectrum under optical excitation. The results suggest modifying the method of analyzing the transient absorption spectra of loss mitigated systems. Additionally, we investigate the effect of Electron Oscillation frequency-Phonon Resonance Detuning (EOPRD) on loss mitigation efficiency. Moreover, power dependent UTAS reveal a frequency pulling like effect in the transient bleach maximum towards the gain emission. We show that appropriate choice of the pump wavelength and by changing the pump power we can conclusively prove the existence of loss mitigation using UTAS. Finally, we study the transient kinetics of hybrid gain-plasmon systems and report interesting hybrid transient kinetics.

1-Introduction to compensation of plasmonic losses with gain:

Surface plasmons (SPs) are quasi-particles that result from coupling electromagnetic (EM) field to free electrons that collectively oscillate at an interface where the real part of the dielectric function changes signs. The field of plasmonics utilizes SPs for many applications in different technological areas [1-4]. Except for low efficiency applications that are not affected much by losses [5-7] such as surface enhanced Raman spectroscopy (SERS), perfect light absorption and photo-thermal cancer therapy, the strong absorption and

optical losses in the available plasmonic materials is the main obstacle for their promising applications.

EM field confinement is the major advantage of plasmonics. The ability to confine the EM field beyond the diffraction limit requires the existence of free electrons. In general the EM field achieves self-sustaining oscillations by transferring the conserved energy between its electric and magnetic components. However, this self-sustaining oscillation is not possible beyond the diffraction limit, i.e. below $\lambda/2n$, because in deeply sub-wavelength regime the electric (magnetic) field will not get a chance to fully develop its magnetic (electric) counterpart to conserve the total energy [8]. On the other hand, by storing some of the EM energy in the kinetic energy of resonant free electrons in metals (i.e. SPs), sub-wavelength self-sustained oscillation will be possible. In that sense, one can think of a plasmonic NP as a leaky cavity. The motion of such free electrons is inevitably damped due to electron scattering events creating a causal link between excitation of free electrons (SPs) and loss of EM energy.

Localized surface plasmons (LSPs) are excited in nanoparticles (NPs) with free electrons (e.g. metals or doped semiconductors) that are dimensionally comparable or smaller than the wavelength of the resonant electromagnetic field. Absorption of the EM field results from electron scattering events which are mainly electron-phonon scattering, electron-surface scattering and inter-band transitions [8, 9]. These loss channels broaden the plasmon resonance spectrally creating what is called a plasmon band. For instance, the plasmon band of Ag is narrower and sharper than that of Au because the electronic inter-band transition in Au spectrally coincides with the SP resonance, thus adding an extra loss channel.

One possible scheme to deal with losses in plasmonics while maintaining the EM sub-wavelength confinement is to introduce gain in the dielectric surrounding of the plasmonic NPs such that the gain emission spectrally overlaps with the plasmon band [10-12]. The gain provides an energy source that compensates the optical losses and thus maintains self-sustaining oscillation of the EM field while keeping the sub-wavelength field confinement in the vicinity of the NP. This energy transfer takes place through dipole-dipole non-radiative resonant energy transfer between the excitonic element (donor) and plasmonic NPs (acceptor). The resonance condition is satisfied when the donor emission spectrally overlaps with the SP resonance of the acceptor. The energy transfer process is irreversible and thus the gain is weakly coupled to the plasmonic NP. This effect has been experimentally investigated by using reflection and transmission pump-probe spectroscopies complemented by fluorescence time-resolved spectroscopy [13-16]. In addition, transient absorption spectroscopy (TAS) has been employed to verify the existence of loss mitigation effects [17-19].

wavelength field confinement in the vicinity of the NP. This energy transfer takes place through dipole-dipole non-radiative resonant energy transfer between the excitonic element (donor) and plasmonic NPs (acceptor). The resonance condition is satisfied when the donor emission spectrally overlaps with the SP resonance of the acceptor. The energy transfer process is irreversible and thus the gain is weakly coupled to the plasmonic NP. This effect has been experimentally investigated by using reflection and transmission pump-probe spectroscopies complemented by fluorescence time-resolved spectroscopy [13-16]. In addition, transient absorption spectroscopy (TAS) has been employed to verify the existence of loss mitigation effects [17-19].

However, a systematic and detailed study utilizing pump-probe transient absorption spectroscopy on hybrid gain-plasmon systems has not been performed to date. In addition, previous theoretical [15,16] and experimental [14,17] works have neglected the effect of the pump beam on the NP optical properties. This is a significant issue since it can result in experimental artifacts for the optical characterization of plasmonic materials.

In this work, we study the transient absorption of resonant gain-plasmon aggregates as hybrid nano-assemblies and their ultrafast transient kinetics. We perform detailed pump-probe transient absorption spectroscopy experiments to investigate the loss mitigation process of aggregated Au NPs in close vicinity of core-shell QDs. We show that enhanced transmission could be due to other effects occurring in the material during optical pumping and probing processes and that these effects can be misinterpreted as loss mitigation. Furthermore, we highlight the transient nature of the plasmon band quality factor and the effect of Electron Oscillation frequency-Phonon Resonance Detuning (EOPRD) on loss mitigation efficiency. Additionally, we show that loss mitigation of NP aggregates occurs for the subset of plasmon resonances that overlap with the gain emission and that loss mitigation efficiency is wavelength dependent. Such wavelength dependence is translated in the dependence of loss mitigation maximum wavelength on pump power, which has been predicted theoretically, [15] and in the effect of EOPRD on loss mitigation at different wavelengths. Finally, we study the transient kinetics of loss mitigated systems and the effect of NP-gain relative concentrations on the dynamics of loss mitigation. In addition to understanding the dynamics of optical loss mitigation in resonant gain-plasmon nano-assemblies, we provide new insights regarding engineering hybrid gain-plasmon systems to unlock potential applications of plasmonic nanostructures.

The measurements are carried out on three systems a) a Polydimethylsiloxane (PDMS) host doped with aggregates of core-shell CdSe@ZnS QDs; this is the Gain System (GS), b) a PDMS host doped with aggregates of 11 nm Au NPs, in two different concentrations; lower concentration (AuL) of 1×10^{-6} M and higher concentration (AuH) of 3×10^{-6} M, and c) a PDMS host containing a mixture of QDs and Au NPs with the same concentration of QDs in GS and the same concentration of Au NPs of AuL (for GS_AuL) and AuH (for GS_AuH). Fig. 1a shows a scheme of the three systems.

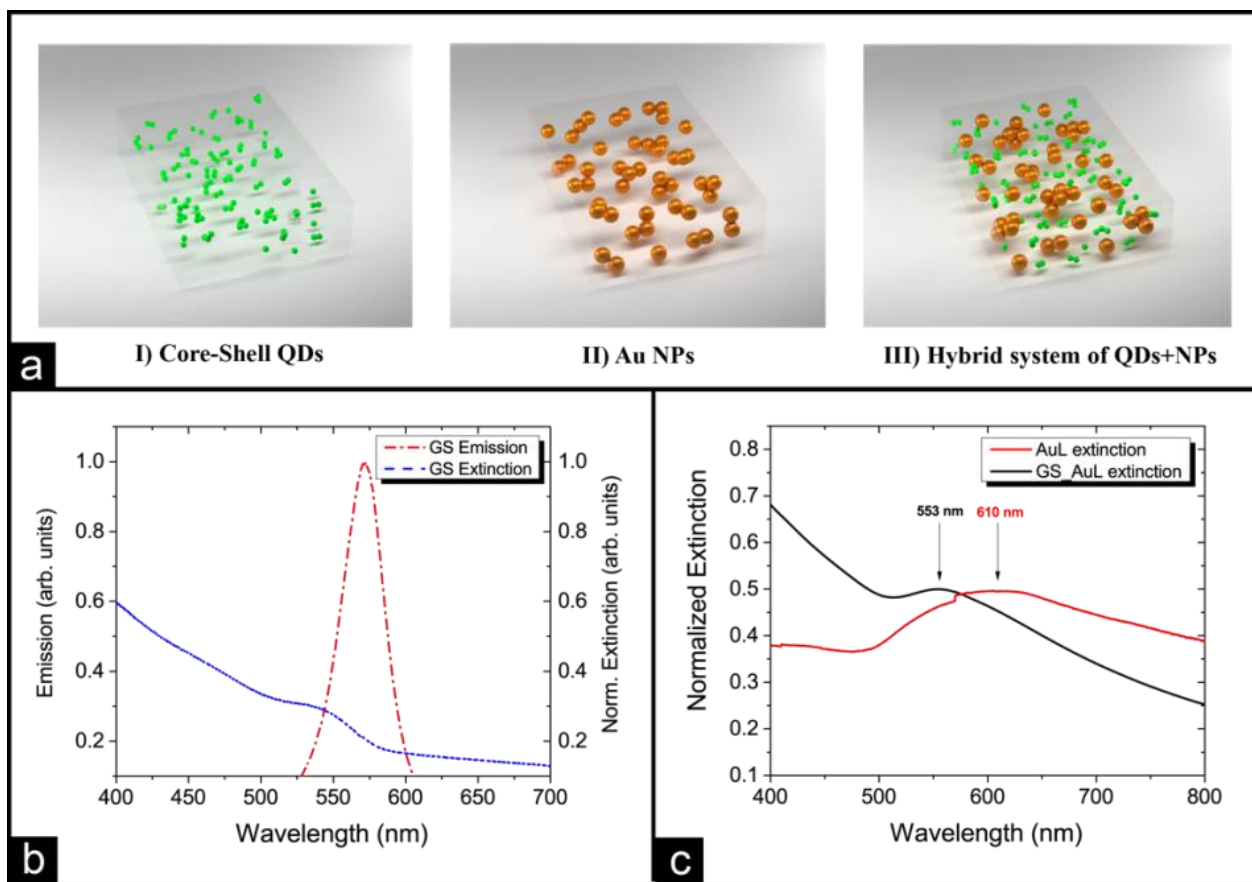


Figure 9 | (a) A schematic of fabricated nanocomposite PDMS films with embedded I) CdSe@ZnS QDs (GS) II) Au NPs (AuL, AuH) and III) mixture of Au NPs and QDs (GS_AuL, GS_AuH). (b) The QDs normalized extinction and emission. The emission maximum is ≈ 570 nm, and extinction maximum is ≈ 545 nm (c) The extinction spectra of AuL and GS_AuL. AuL has a broad extinction due to NP aggregation. GS_AuL extinction maximum is a convolution of the extinction of both QDs and NPs. An estimate of the “true” plasmon extinction of NPs is presented in the Electronic Supplementary Material section 1 and its maximum is ≈ 590 nm.

2- Results and discussion

2.1 Samples characterization

The extinction and emission curves of **GS** as well as the extinction of both **AuL** and **GS_AuL** are presented in Fig. 1b and 1c, respectively. According to Figure 1c, the broad extinction peak of **AuL** is centered at roughly 610 nm. The broadening of the plasmon band is due to NP aggregation within the polymer [20].

Furthermore, **GS_AuL** extinction reflects the extinction of aggregates of both QDs and NPs exhibiting a peak at ≈ 553 nm. This is not the true plasmon resonance extinction peak due to the influence of the QDs extinction.

Our analysis shows that the plasmon extinction peak wavelength of **GS_AuL** is ≈ 590 nm. To locate the extinction of the NPs only in the hybrid system **GS_AuL**, we removed the QDs extinction by subtracting their properly scaled extinction from that of **GS_AuL** (Fig.2). To perform this operation, we choose a particular wavelength where there is little variation in the difference between the extinction of **GS** and **GS_AuL**. For our calculations we picked 470nm, where the absorption curves of **GS** and **GS_AuL** are nearly parallel, i.e. they differ by a constant. This means that there is a very small contribution from the NPs to the total extinction in **GS_AuL**. We then subtract the optical density of **AuL** at this location from that of **GS_AuL**, and divide the result by the optical density of **GS**. By doing this we receive a scale factor that we use to scale down the extinction of **GS** so that it can be directly subtracted from **GS_AuL**. After performing the subtraction, we find that the new peak is located at ≈ 590 nm approximately 40 nm away from the measured extinction of the hybrid system.

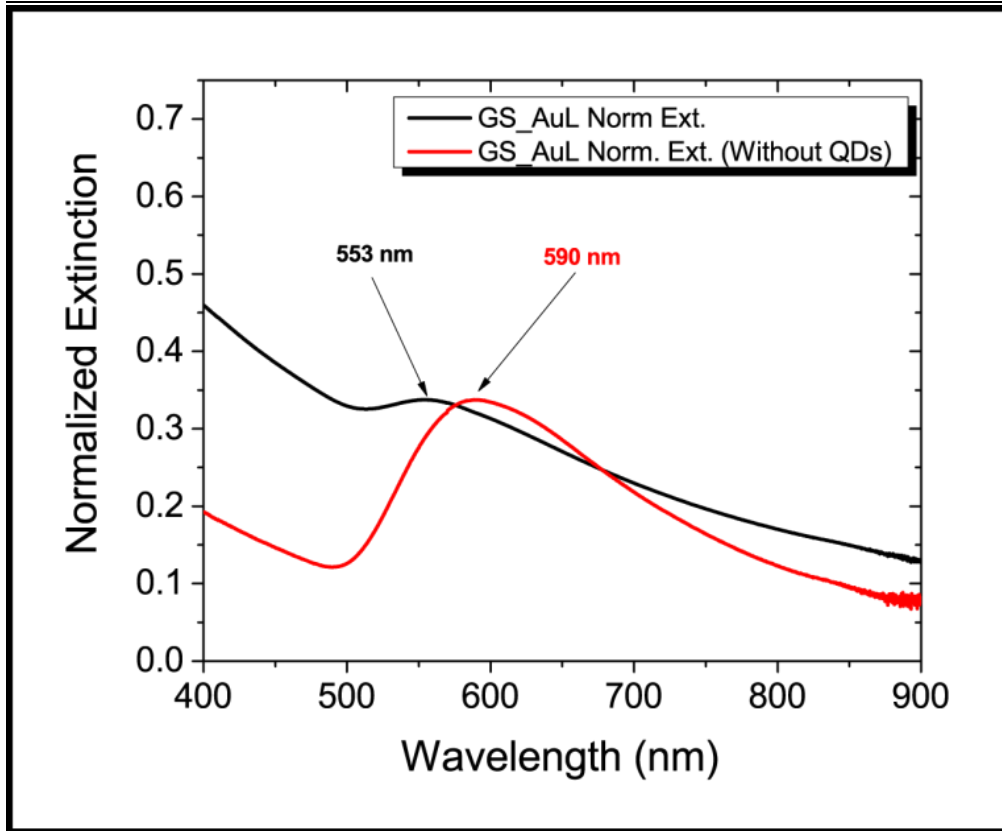


Figure 2 | Normalized extinction of **GS_AuL** before and after excluding the extinction of the incorporated QDs. The extinction of Au NPs in **GS_AuL** is found to be located at ≈ 590 nm.

The emission of the embedded QDs is roughly the same for **GS** and **GS_AuL**. The emission maximum of QDs is at $\lambda = 570$ nm overlapping with the plasmon band of **GS_AuL** and thus satisfying the loss mitigation non-radiative resonant energy transfer condition.

2.2 Ultrafast Transient Absorption Spectroscopy measurements (UTAS)

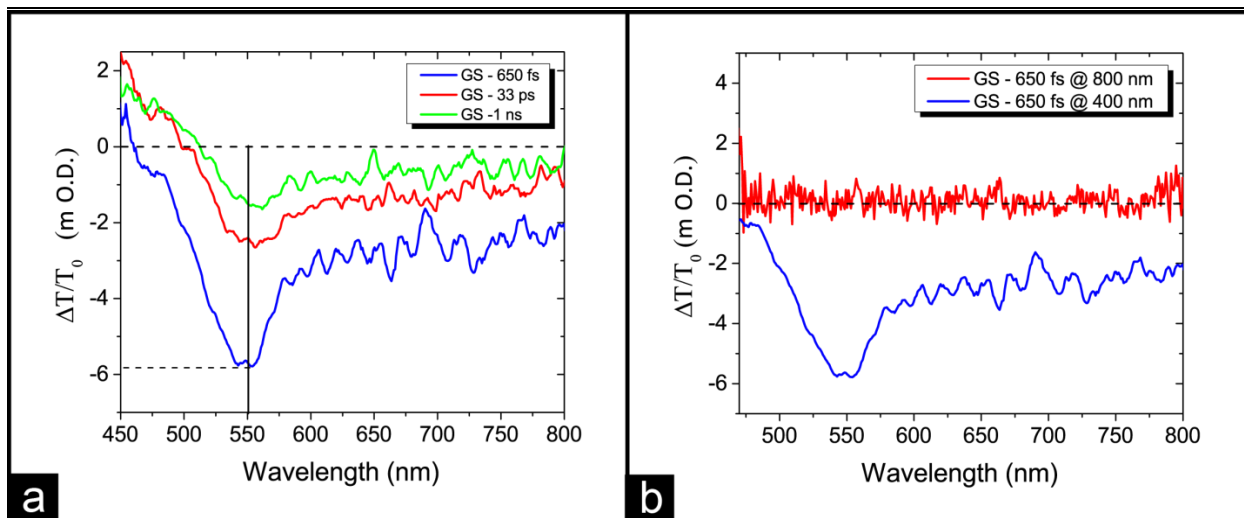
After exciting the sample by an ultrafast pump pulse, a temporally delayed probe pulse is used to extract the pump-induced absorbance change of the sample. The experimental setup details are provided in the methods section. By measuring the wavelength-dependent intensity of the delayed probe spectra in the presence ($I_{\lambda,t}$) and the absence ($I_{\lambda,0}$) of the pump pulses, the transient absorption signal $S(\lambda,t)$ is calculated based on the following equation:

$$S(\lambda, t) = \frac{\Delta T}{T_0} = -(I_{\lambda, t} - I_{\lambda, 0}) / I_{\lambda, 0} \quad (18)$$

Note that according to our sign convention, a positive sign of pump-probe differential transmission ($\Delta T/T_0$) corresponds to a decrease in transmission (transient absorption), whereas a negative sign of $\Delta T/T_0$ corresponds to an increase in transmission (transient bleach).

The measurements were performed by using 400 nm and 800 nm excitation wavelengths in order to independently probe the effect of gain excitation and energy transfer processes on the transient absorption signal. In addition, the delay between the pump and probe was varied to observe the modification of the transient absorption signal over time and to examine the transient decay kinetics of all the systems.

Transient absorption (TA) measurements for GS sample (Fig. 3a) are performed using a 400 nm wavelength pump at 1 μJ for 650 fs, 33 ps, and 1 ns delay times. The maximum bleach wavelength is ≈ 550 nm which is close to the local absorption maxima shown in Fig. 1b. As we increase the delay time the bleach initially increases in magnitude, reaching its maximum at 650 fs, and then it starts to decrease. The QDs bleach in GS is mainly due to the well-known band filling effect [21, 22] where the pump beam excites the valence band electrons to the conduction band. The TA signal for the band filling effect corresponds to a bleach effect reflecting the inability to excite more electrons to the already populated states in the conduction band. On the other hand, exciting the system with 800 nm does not cause any bleach as it is outside the QDs absorption band (Fig. 3b).



(a) Transient Absorption (TA) results for GS for three delay times; 650 fs, 33 ps, and 1 ns for 1 μ J pump energy.

Figure 3

We observe a broadband bleach that has a maximum around 550 nm due to the band filling effect. (b) Pumping GS with 800 nm pump wavelength we observe no bleach since we are not exciting any QDs.

Fig. 4a shows the TA spectrum of AuL at 650 fs, 1.3 ps and 2.5 ps delay times for 400 nm excitation pump wavelength and 1 μ J energy. The signal vanishes within the noise at around 3 ps. The bleach maximum wavelength is \approx 575 nm, which blue shifts over time. Additionally, we observe a positive absorption band at the higher energy side of the bleach.

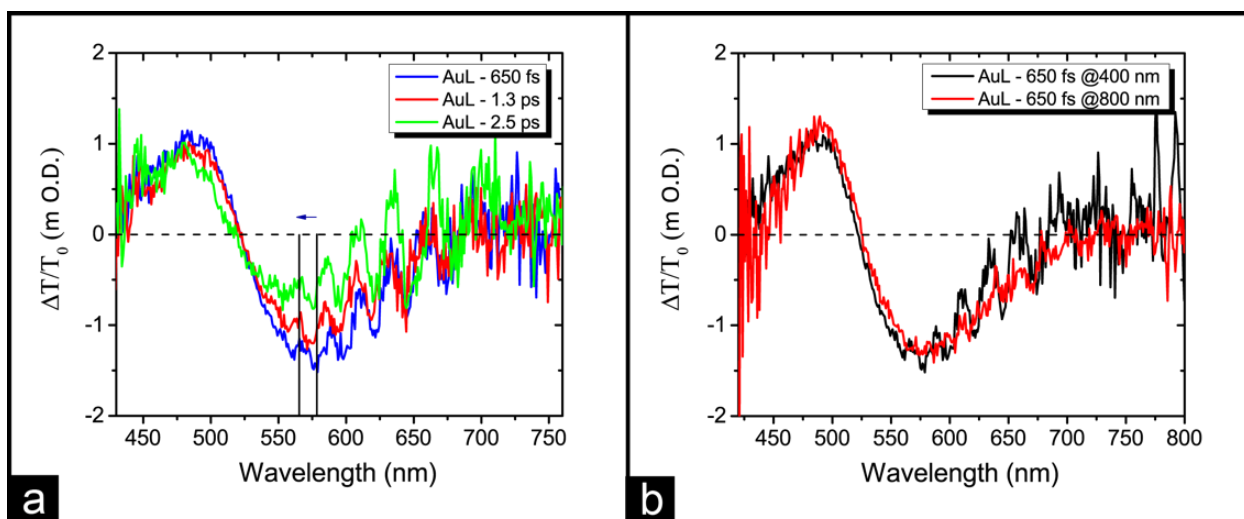


Figure 4 (a) TA results for AuL for three delay times; 650 fs, 1.3 ps, and 2.5 ps. The bleach maximum is \approx 575 nm. The TA profile is due to creating hot electrons that modify the NPs permittivity. An absorption wing appears at higher energies with respect to the bleach. There is another low energy absorption wing that is below the noise level. Additionally, the bleach maximum blue shifts as the delay time increases due to reduced EOPRD (b) Excitation of AuL with 400 nm and 800 nm pump wavelengths after 650 fs probe delay exhibits similar TA behavior.

Generally, the excitation of mono-dispersed Au NPs results in plasmon bleaching feature; i.e., transient quenching and broadening of the plasmon band [23]. Accordingly, $(\Delta T/T_0)$ figure features a transient bleach centered at the plasmon band absorption maximum and two positive absorption bands (or wings) at lower and higher energies relative to the bleach. This is attributed to modifying the NPs permittivity due to the creation of hot electrons, i.e. electrons that thermalize after absorbing EM field energy due to a scattering event and are at an elevated temperature with respect to the metal lattice [24]. Upon pumping the NPs, the plasmon band broadens spectrally and its maximum peak intensity drops, i.e. the plasmon resonance quality factor decreases. This drop in plasmon resonance quality factor indicates the existence of an extra damping or loss mechanism of the oscillating free electrons as we have discussed earlier. Hot electrons are more likely to experience scattering according to Fermi liquid theory [24, 25]. Furthermore, hot electrons have an augmented velocity due to their thermalization which makes them more amenable to surface scattering as well as collision-less Landau damping that occurs for plasma oscillation of hot electrons [26]. It is important to emphasize that the quality factor of the plasmon resonance is not a steady state property. In practice, exciting the NP directly or indirectly, e.g. by exciting the gain, introduces additional losses and thus modifies the plasmon resonance transient quality factor.

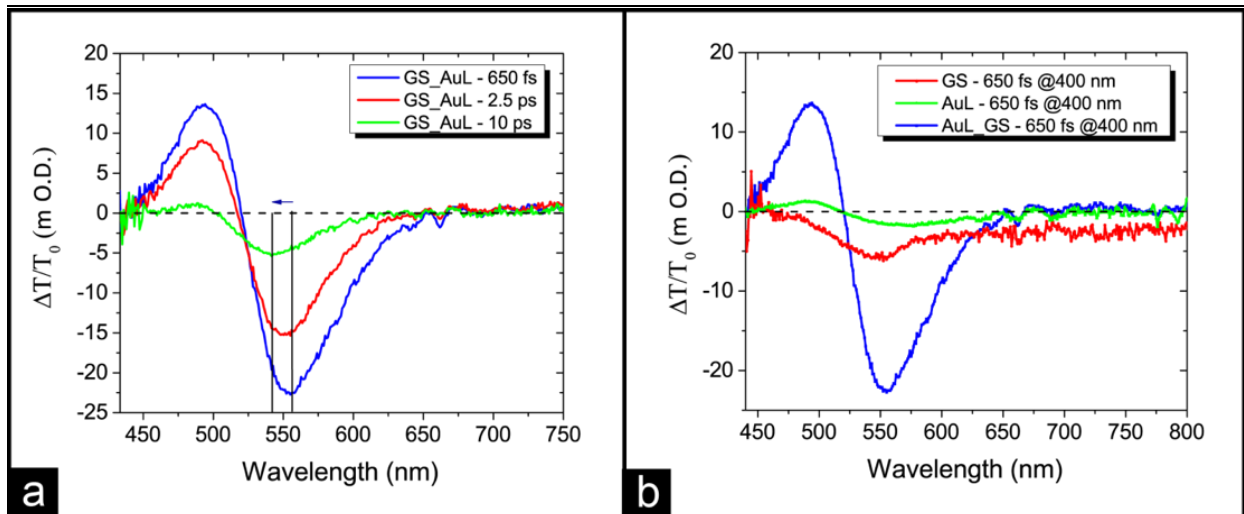


Figure 5] (a) TA results for GS_AuL for 650 fs, 2.5 ps, and 10 ps delay times. The bleach maxima blue shifts as a function of delay time due to reduced EOPRD. In (b) we compare the bleach magnitude for GS, AuL and GS_AuL. The bleach is considerably stronger for GS_AuL than the combined bleach of both GS and AuL indicating the existence of loss mitigation. However, the TA spectra of AuL and GS-AuL are qualitatively similar.

Previous works have shown that the transient absorption bands/wings of pumped NP aggregates are uneven [27, 28]. The higher energy absorption wing is larger in magnitude than the lower energy wing. We also observe two uneven transient absorption wings; however, the lower energy wing magnitude is lower than the noise level. Fig. 4a shows a blue-shift in the bleach maxima as a function of delay time for **AuL**. This is due to faster transient bleach decay for longer wavelengths compared to shorter wavelengths. The blue shift of the bleach peak for NP aggregates is attributed to a reduction in the EOPRD [28]. EOPRD reflects the coupling strength between the electron oscillation frequency and the phonon modes of a given NP such that the smaller the detuning the stronger the coupling. The electron oscillation frequency is equal to v_f/R where v_f is the fermi velocity and R is the domain radius. For very small domains, the electron oscillation frequency exceeds the Dybe frequency of phonons which corresponds to the upper bound of the phonon mode spectrum. This frequency detuning decreases the electron-phonon coupling strength [29]. Given that hot electrons cool down by exciting phonons via electron-phonon scattering, the smaller the frequency detuning, the stronger the

electron-phonon coupling and the faster the decay of the transient absorption/bleach. It has been suggested previously [28] that the probe beam interrogates a particular subset of the aggregates that corresponds to the excited resonance. For NP aggregates, resonances that correspond to longer wavelengths have larger domain radii which enhance the coupling to phonon modes [30]. Accordingly, longer wavelengths should experience faster decay kinetics of the TA spectrum compared to shorter ones resulting in the observed blue shift in the bleach maxima as a function of delay time. This is not the case for mono-dispersed NPs, where increasing the NP size decreases EOPRD, but also decreases the electron-surface scattering rate resulting in seemingly size independent decay kinetics [29,31]. It is important to note that exciting AuL at 800 nm (Fig 4b) results in a similar bleach to that of 400 nm excitation [31].

For the hybrid system (**GS_AuL**), we have shown previously that the gain is coupled via non-radiative energy transfer to the embedded plasmonic NPs via time resolved spectroscopy and pump probe spectroscopy [32]. Here we are interested in the transient dynamics of loss mitigation in such hybrid system. Fig. 5a shows the transient absorption results for **GS_AuL** at 650 fs, 2.5 ps and 10 ps delay times for 400 nm excitation pump wavelength and 1 μ J energy per pulse. We observe a transient bleach band, and two uneven transient absorption wings. Compared to the TA results of both **GS** and **AuL**, the bleach signal of the hybrid system is considerably higher than the combined bleach of **GS** and **AuL** (Fig. 5b). This observation quantitatively proves the existence of loss mitigation indicated by significant enhancement in transmission. To further confirm our results, we performed UTAS measurements on **GS_AuH** and obtained the same behavior of **GS_AuL** (Fig. 6).

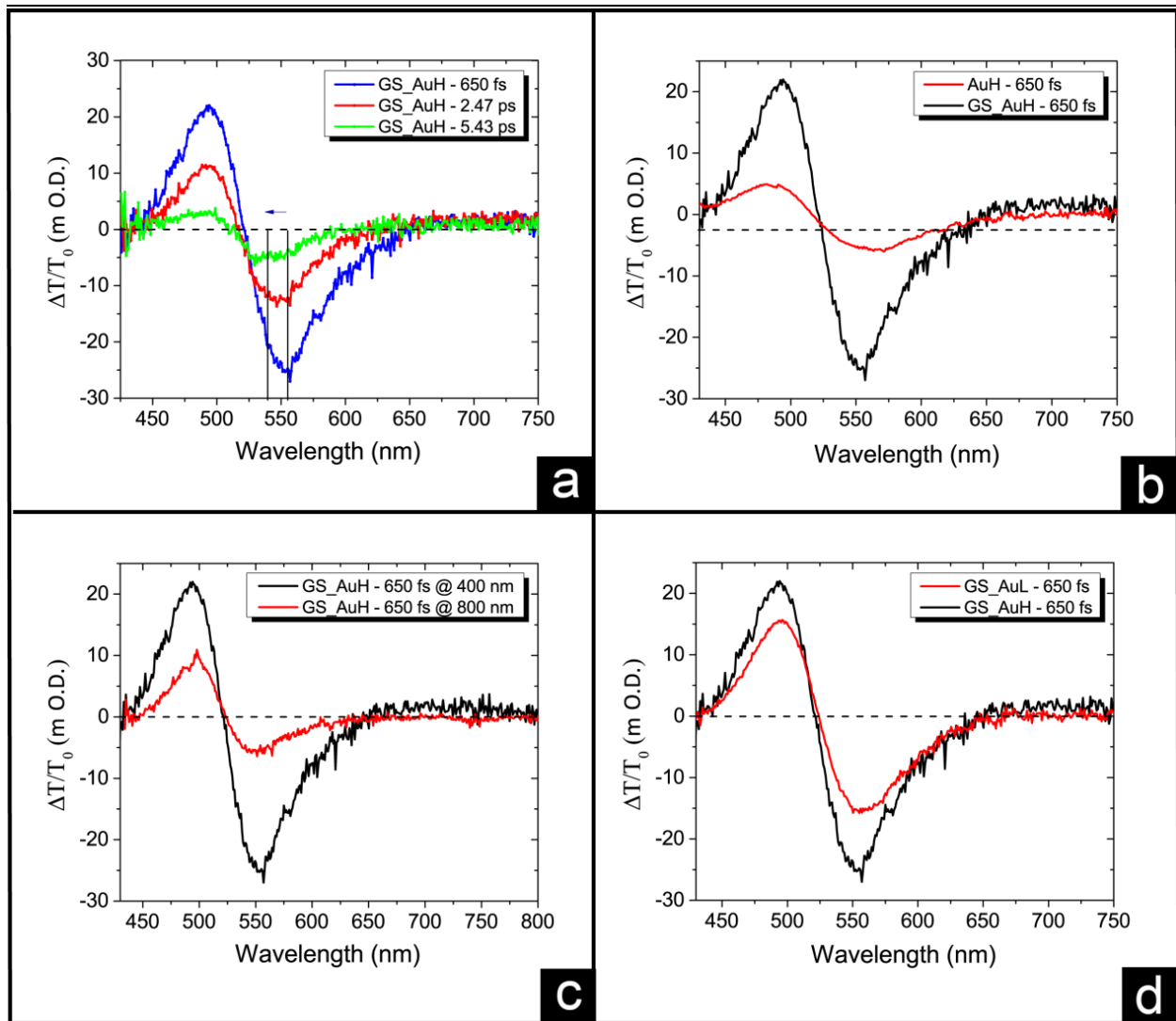


Figure 6 | (a) The TA of **GS_AuH** for three delay times; 650 fs, 2.47 ps, and 5.43 ps shows similar behavior to that of GS-AuL. Compared to AuH, that has the same NP concentration, we see in (b) that the TA spectrum is significantly larger in magnitude due to loss mitigation. This effect does not take place upon pumping **GS_AuH** with 800 nm as shown in (c). (d) Shows a comparison between the UTAS results for **GS_AuL** and **GS_AuH**.

From a qualitative point of view, however, **AuL** and **GS_AuL** provide very similar TA spectra (Fig. 5b). This may be misinterpreted as loss mitigation and it is a consideration that was largely ignored by previous works [15]. In addition, performing a transient measurement by varying the delay time between the pump and probe beams cannot exclude such effect because it is also a transient phenomenon. It is necessary to note that the modifications of NP permittivity due to creating hot electrons and due to loss mitigation are completely different phenomena. Plasmon

bleaching of NPs due to creating hot electrons results in a simultaneous drop in absorption as well as scattering of the electromagnetic field by the NPs, i.e. the NP polarizability drops [33] and a new source of damping and loss is created. However, for the case of loss compensation, the final goal is to decrease the NP absorption while increasing its scattering [11] through providing energy to the quasi-static plasmon field in order to compensate for electron oscillation damping. On the other hand, the two effects produce similar TA spectrum; both produce bleach within a certain spectral range, and an increase in absorption in a contingent spectral range. For the case of loss compensation, however, the absorption increase is a consequence of Kramers-Kronig integral relations [14, 15] and not due to a drop in the resonance quality factor as in the case for NPs only in **AuL**.

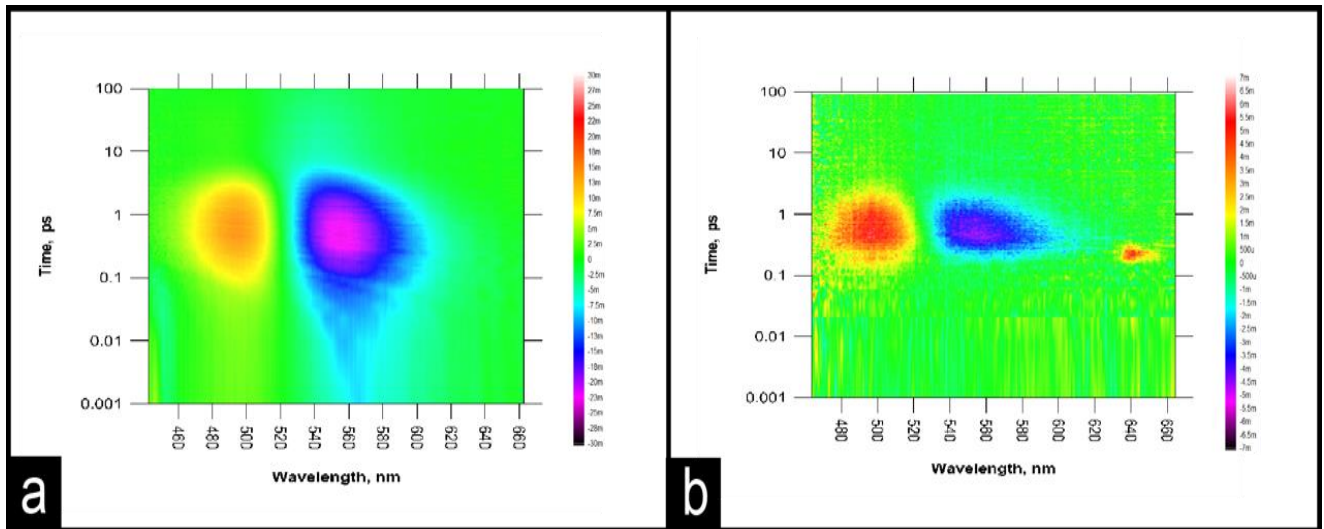


Figure 7 | Bird-eye view diagrams of GS_AuL for pump wavelengths (a) 400 nm (b) 800 nm. The TA signal magnitude is considerably higher for 400 nm excitation compared to 800 nm excitation. At 800 nm we do not excite the gain and thus we exclude the contribution from loss compensation to the bleach.

One way to distinguish between these two effects is to perform transient reflection spectroscopy (TRS) in addition to TAS. If the bleach in TAS spectrally corresponds to a drop in scattering in TRS, then this is merely due to modifying the NPs permittivity [33, 13]. However,

TRS is not a suitable technique for our system because embedding the NPs in a dielectric host reduces scattering significantly and thus results in a very low signal to noise ratio.

Another way to exclude the effect of pump induced permittivity modification is by pumping the hybrid system away from the gain absorption. Therefore, we pump **GS_AuL** @ 800 nm with pump energy 1 μJ per pulse (Fig.7). It is clear that the bleach for 800 nm excitation is significantly lower than that for 400 nm unlike what we have seen earlier in Fig. 4b for AuL. The same behavior of **GS_AuL** was observed for **GS_AuH** and is shown in Fig.6.

Fig. 5a shows that the bleach maxima also blue shifts over time. This blue shift is in part due to the decreased EOPRD of hot electrons in NP aggregates at longer wavelengths resulting from direct absorption of the excitation beam as we detailed previously for the case of **AuL** system. However, induced bleach due to loss mitigation should also exhibit a similar blue shift. This is because electron-phonon scattering plays a dual role: a) it mediates absorption of electromagnetic energy creating hot electrons, and b) it cools down hot electrons by transferring its extra heat to the lattice through phonons. In the case of loss mitigation, oscillating electrons at longer wavelengths in NP aggregates also experience stronger electron-phonon scattering because of their lower EOPRD. This means that enhanced transmission due to loss mitigation at longer wavelengths should decay faster than that at shorter wavelengths because of the existence of stronger damping, mediated by electron-phonon scattering. The

enhanced electron-phonon scattering rate for longer wavelengths is of considerable significance. Although, it has been suggested that red-shifting the plasmon resonance of noble metals would allow them to exhibit lower losses, [34] this suggestion ignores the introduction of an extra transient loss mechanism, i.e. decreased EOPRD at longer wavelengths.

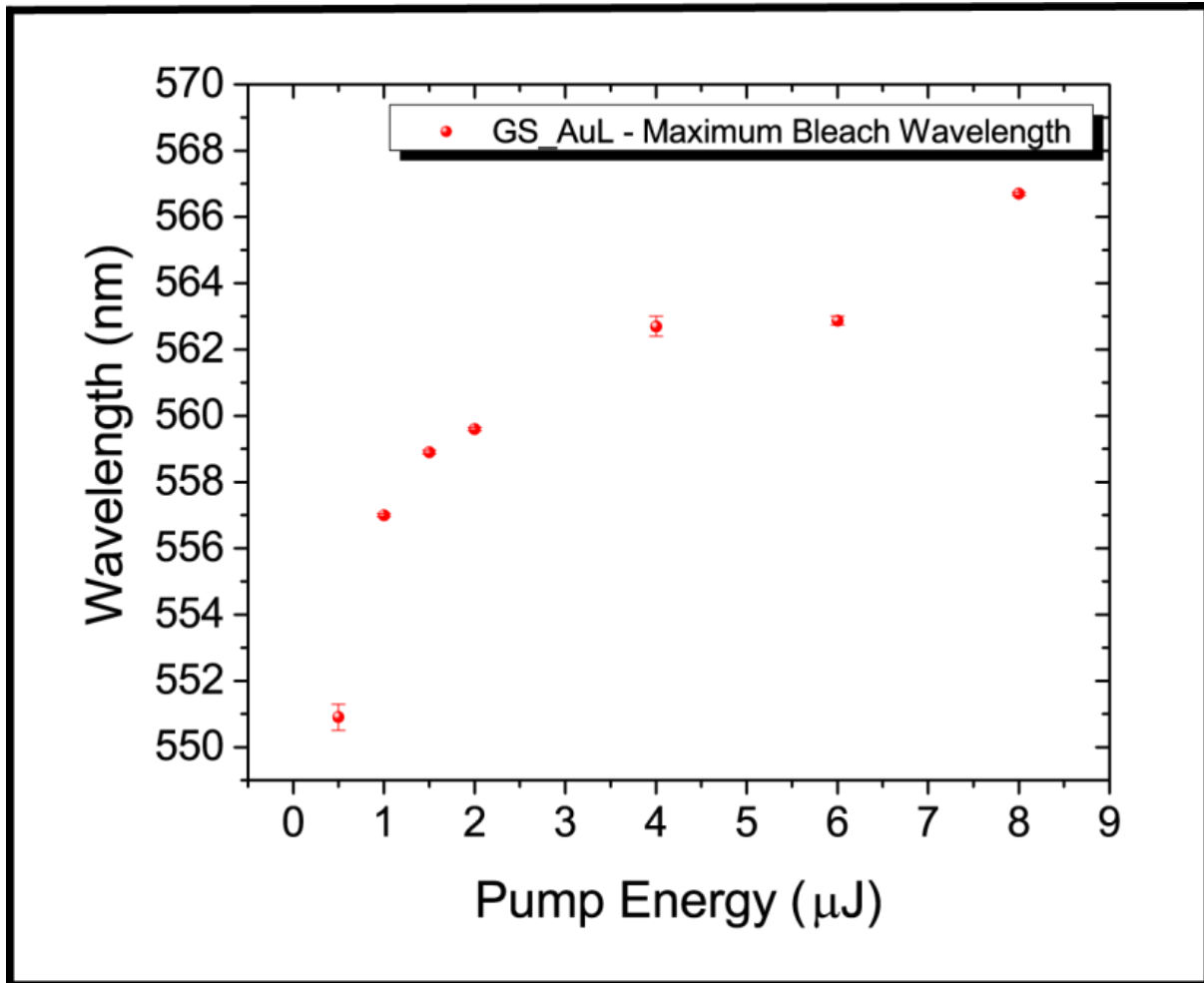


Figure 8: Maximum bleach wavelength vs. Pump energy for GS_AuL. The maximum bleach wavelength shifts is pulled towards the emission maximum of the coupled gain due to enhanced loss mitigation as a function of pump power.

While it has been shown previously that loss mitigation can be optimized for the case of Au core-Gain shell aggregates due to enhanced field localization, [35] one should take into account the transient dynamics of such compensation. Compensating losses of the subset of

SP resonances that experience stronger damping, in our case resonances at longer wavelengths due to EOPRD, decreases the efficiency of loss compensation over time [10].

Furthermore, for 400 nm excitation the bleach maximum wavelength shifts as a function of pump power. As shown in Figure 6, the maximum bleach wavelength starts at ≈ 551 nm for 0.5 μ J and progresses towards $\lambda = 570$ nm which corresponds to the maximum emission wavelength. The maximum bleach wavelength was determined by using a polynomial fit to the bleach curve. This frequency pulling like effect of the bleach maximum is due to enhanced loss mitigation at the maximum emission wavelength as a function of pump energy. For AuL, however, we observe no shift in the bleach maximum as a function of pump energy. A similar behavior was reported theoretically in reference [15]. The authors defined a figure of merit (FOM) of loss mitigation as $FOM = \text{Re}\{n\}/\text{Im}\{n\}$. The FOM increased as a function of pump intensity and the maximum FOM wavelength shifted towards the maximum emission wavelength of the gain [15]. Since the probe beam interrogates the subset of aggregates that correspond to a given excited resonance, we can conclude that loss mitigation occurs for electromagnetically coupled NP aggregates for the subset of frequencies that correspond to the gain emission and depends on the loss mitigation efficiency at each emission wavelengths.

2.3 Transient decay kinetics

The transient decay kinetics of exciton-plasmon resonant hybrids provides a panoramic view on the evolution of loss mitigation process over time. In particular, it allows us to study the non-radiative exciton-plasmon energy transfer process by studying the decay kinetics of the transient absorption spectrum. Here we focus on the spectral region where the bleach occurs. The lifetimes are fitted by the following equation:

$$S(t) = e^{-\left(\frac{t-t_0}{IRF/2.2}\right)^2} \times \sum_i A_i e^{-\frac{t-t_0}{\tau_i}} \quad (19)$$

where $S(t)$ is the fitting function, IRF is the width of instrument response function (full width half maximum) and is set to be 0.1 ps corresponding to the pump pulse, t_0 is time zero where the fitting starts, A_i and τ_i are the amplitudes and decay times respectively.

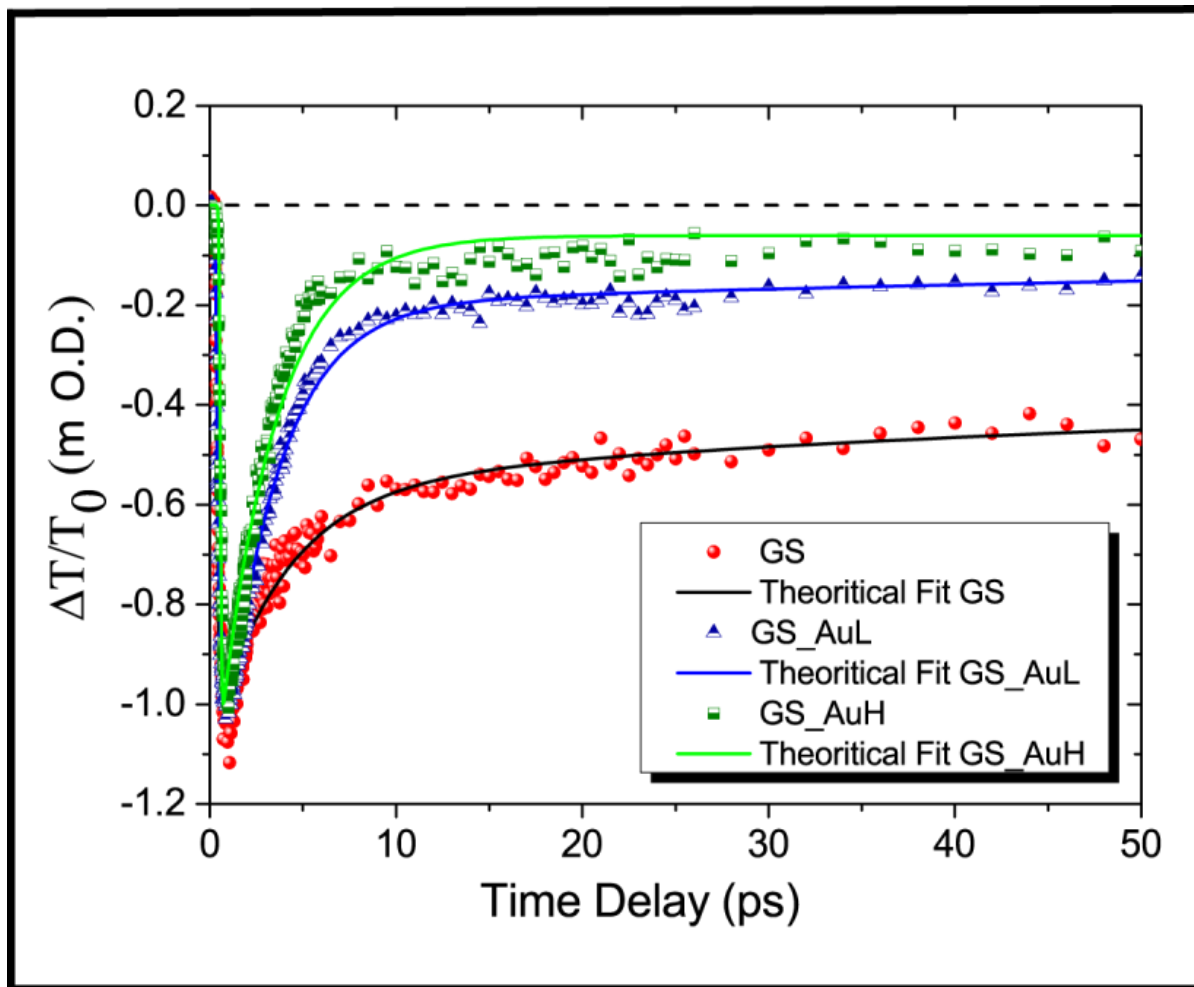


Figure 9| Transient bleach dynamics results of GS, GS_AuL and GS_AuH and their theoretical fitting. The shortening of the bleach decay time for GS_AuH compared to GS_AuL reflects the effect of increasing the acceptor's concentration on gain depletion.

The transient kinetics results of **GS**, **AuL**, **AuH**, **GS_AuL**, and **GS_AuH** are at 570 nm presented in table 1. In all samples, the first time component τ_1 is assigned to the increase in the bleach (for 400 nm excitation wavelength with 1 μ J pump energy per pulse), while all other

components correspond to the decay of the bleach over time. For GS, the bleach decay has three lifetime components. An infinite lifetime means that it is longer than the maximum delay achievable by our setup. For **AuL** and **AuH** we have one bleach rise lifetime component (τ_1) and two bleach decay lifetime components (τ_2 and τ_3). The first lifetime component (τ_1) reflects electron-electron scattering that thermalizes the electron gas creating a fermi distribution of hot electrons which results in the observed bleach. The bleach decay components (τ_2) and (τ_3) correspond to electron-phonon relaxation and phonon-phonon relaxation respectively [24]. Interestingly, the decay kinetics for **GS_AuL** shows similar behavior to that of **GS** as they share the same lifetime components with shorter bleach decay lifetimes (τ_2 and τ_3) for **GS_AuL** compared to **GS**. The decay kinetics of the hybrid system dynamics reflects both the drop in the bleach due to hot electron cooling as well as the decay in loss compensation efficiency over time as the (donor) gain depletes due to transferring its energy to the (acceptor) plasmonic NPs. When we have high plasmonic NPs concentration as in **GS_AuH**, the gain depletion process becomes more efficient and the decay kinetics starts to look similar to that of pure plasmonic system. Accordingly, the decay dynamics of the hybrid system has gain like and plasmon like features where the gain tends to increase the bleach lifetime and the energy transfer accompanied by plasmonic losses tends to decrease it (Fig. 9).

Sample	τ_1 (ps)	τ_2 (ps)	τ_3 (ps)	τ_4 (ps)
GS	0.15±0.02	3.1±0.3	737±150	inf
AuL	0.17±0.1	2.6±0.5	inf	-
AuH	0.17±0.07	1.8±0.2	inf	-
GS_AuL	0.19±0.01	2.45±0.09	115±32	inf
GS_AuH	0.2±0.06	2.1±0.2	inf	-

The observed behavior of the decay kinetics highlights the fact that gain mediated loss mitigation is a transient phenomenon by its nature as the gain itself depletes over time. It also shows that gain mediated loss mitigation does not eliminate losses like other strategies [8]. Oscillating electrons will still scatter and the energy will be absorbed with or without the gain. The existence of the gain, however, maintains the resonant response of oscillating free electrons from decaying by transferring energy over time to the quasi-static field of the plasmonic nanoparticles.

3- Conclusion

In summary, we have studied ultrafast dynamics of coupled core-shell CdSe@ZnS QDs, and Au NPs aggregates via femtosecond TAS. By studying the TA signal of QDs only and Au NPs only, we were able to separate loss mitigation in hybrid exciton-plasmon nano-assemblies from other effects that also enhance the transient transmission (bleach). Additionally, we showed a frequency pulling like effect of the transient bleach signal towards the emission maximum of the gain; an effect that has been previously predicted theoretically.¹⁵ Furthermore, we presented that loss mitigation can occur for the subset of resonances of NP aggregates that overlap with the gain emission. Finally, we have investigated the transient kinetics of the bleach for all systems. The hybrid gain-plasmon systems have hybrid bleach decay dynamics reflecting the non-radiative energy transfer process between the gain (donor) and plasmonic NPs (acceptor).

This work provides deeper understanding of exciton-plasmon dynamics to control optical losses in plasmonic nanostructures. Exciting the NPs directly creates hot electrons which suffer from more losses compared to cold electrons. To reduce optical losses, it is important to minimize the excitation of hot electrons. The excitation of hot electrons can be

moderated by increasing the gain concentration in the presence of plasmonic NP aggregates since most of the pump energy will be absorbed by the gain, as proven by our TAS analysis. Furthermore, we reported that by increasing EOPRD we have decreased electron-phonon coupling, and this increases loss mitigation efficiency. While other works³⁶ attempted to directly improve the quality factor of plasmon resonance through careful choice of materials and design of plasmonic nanostructures, performing TAS analysis opens a new venue for investigating and optimizing the transient quality factor of plasmon resonance and eventually control losses in selected frequency ranges.

4-Experimental

4.1 Preparation of nanocomposite hybrid systems

The elastomer was mixed thoroughly with the curing agent in the weight ratio of 10 : 1 and then degassed under vacuum to remove entrapped air bubbles. Au NPs (100 μ L, 3×10^{-6} M solution in hexane) and/or QDs (100 μ L, 6×10^{-5} M solution in hexane) were added to the pre-polymer mixture (2 g) and vigorously stirred for 1 h to obtain a homogeneous mixture. The resulting mixtures were cast into a support template (2.5 cm \times 2.5 cm) and the films were cured at 70 $^{\circ}$ C for 24 h to obtain ca. 3 mm thick self-standing films. The detailed information about the synthesis procedure of QDs and Au NPs can be found in [37].

4.2 Characterization and Measurements

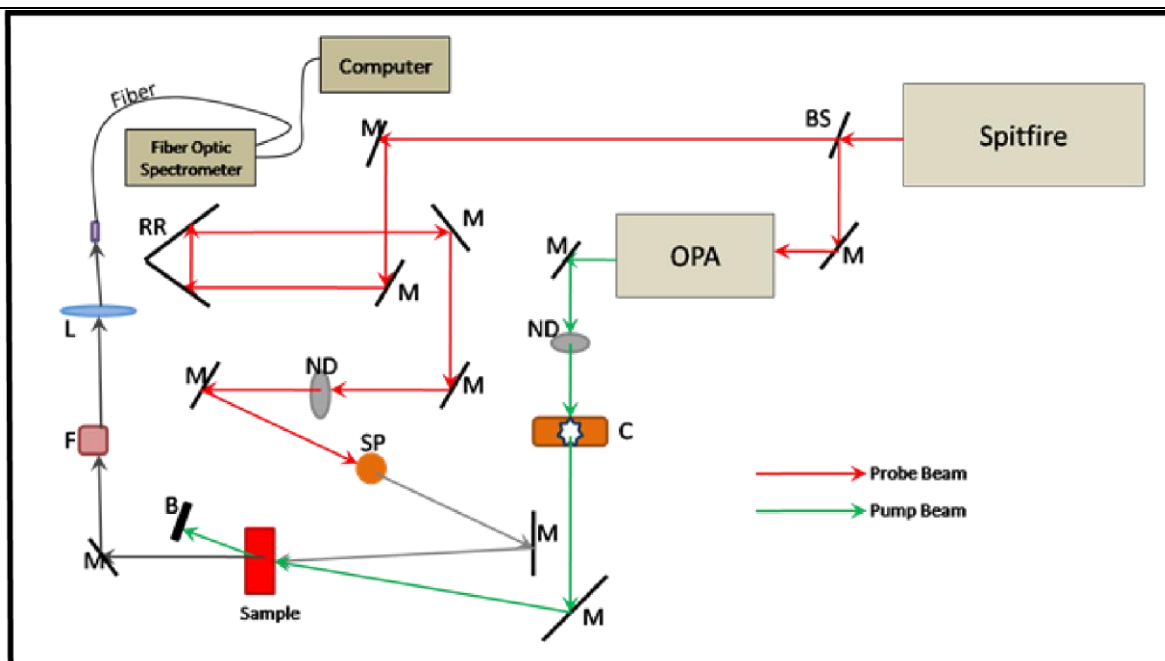
The extinction was measured using Cary 300 UV-VIS spectrophotometer, whereas the Steady-state emission spectra were measured by means of an advanced fluorescence lifetime spectrometer (Edinburgh, FLS980 Series), equipped with CCD Camera (Andor,

iDus 420 Series), a 450 W xenon arc lamp, high performance triple grating monochromators with integrated filter wheels, and a Hamamatsu MCP-PMT.

Ultrafast transient absorption spectroscopy experiments were carried out on all samples using Ti:Sapphire laser amplifier-optical parametric amplifier system (Spectra Physics) with 44 fs pulse duration and 1 kHz repetition rate. Commercial pump-probe experimental setup with white light continuum probe beam (Spectra Physics) was used (for more details see scheme 1). Experiments were performed in transmission geometry. Pulse duration is 100 fs inside pump-probe experimental setup. The sample is pumped with tunable output of the optical parametric amplifier. The excitation wavelength of the pump beam is set based on the energy levels of the target sample. The OPA unit provides the possibility to vary the output wavelength of the pump beam at a wide spectral range of 250 nm to 2800 nm. White light continuum used as probe beam is generated by impinging the 800 nm wavelength light of the Spitfire unit on a sapphire plate. This broadband beam (350 nm-800 nm) is used to monitor the occurred transitions of the electrons to allowed energy levels of the sample. Repetition rate of the pump and probe beams are 500 Hz and 1 KHz respectively. As a result of this matter, the effect of the pump beam will be observed only in one of two consecutive probe beams. Both the pump and probe beams should overlap spatially and temporally over the sample. However, transmitted probe spectra are detected with a fiber optic spectrometer while pump beam is dumped.

In pump-probe technique, the ground state electrons are transferred to the excited states by applying a proper wavelength and energy values of the pump beam. Neutral density filter is used to modify the pump beam power. Consecutive probe spectra with lower intensity are used to extract the changes in spectra due to the pump pulses. The promoted

electrons by the pump beam to the first excited state can be transferred to the higher permitted energy levels by the probe beam. Therefore, in the absence of the pump beam, probe beam can cause the linear absorption, while in simultaneous presence of pump and probe beams, both linear and non-linear absorptions can occur. In order to measure the time duration in which electrons remain in different energy levels, the probe beams must be delayed against to the pump beam. Such a delay is applied by using a motorized retro-reflector mirror in the path of probe beam. The maximum delay of 3 ns between pump and probe pulses can be created by the retro-reflector mirror. The zero reference time is considered as the time that both temporally synchronized pump and probe pulses hit over the sample. Therefore, at the point of zero time, majority of the firstly excited electrons will be promoted to the higher excited states. The successive probe pulses will be delayed increasingly with respect to the pump pulses, by traveling in a longer beam paths created by the retro-reflector mirror. In this case, a portion of the primarily promoted electrons to the first excited state return to the ground state by the aid of the broadband probe beam. In the meantime, the number of stimulated electrons to the higher excited states by the probe light will decrease exponentially. As a result of the exponentially decaying behavior of the observed non-linear effects, at a specific wavelength of the white beam spectrum the decay time of the transient effects can be measured.



Schematic representation of the pump-probe spectroscopy setup. M: Mirror, L: Lens, BS: Beam Splitter, C: Chopper B: Beam Blocker, F: Filter, ND: Natural Density Filter, RR: Retro-Reflector Mirror, SP: Sapphire Plate, OPA: Optical Parametric Amplifier.

Acknowledgments:

This work was done in collaboration with Gul Yaglioglu group, Ankara University, Ekmel Ozbay and Humeyra Caglayan groups, Belkint University. The research leading to these results has received support and funding from the Ohio Third Frontier Project Research Cluster on Surfaces in Advanced Materials (RC-SAM) at Case Western Reserve University. This work was supported by Projects DPT-HAMIT and NATO-SET-193. One of the authors (E. O.) acknowledges partial support from the Turkish Academy of Sciences. H. C. acknowledges support from the Science Academy of Turkey through the BAGEP programme and Turkish Academy of Sciences through the GEBIP programme. This work is published in the following article: “Mohamed ElKabbash, Alireza R. Rashed, Betul Kucukoz, Quang Nguyen, Ahmet Karatay, Gul Yaglioglu, Ekmel Ozbay, Humeyra Caglayan and Giuseppe Strangi , Ultrafast transient optical loss dynamics in exciton-plasmon nano-assemblies, *Nanoscale*, 9, 6558-6566, 2017.

5-References

- 1- H. A. Atwater. *Sci. Am.* 2007, 296, 56.
- 2- J. B. Pendry, D. R. Smith, *Sci. Am.* 2006, 295, 60.
- 3- E. Ozbay, *Science* 2006, 311, 189.
- 4-S. Schlücker, *Angew. Chem. Int. Ed.* 2014, 53, 4756.

-
- 5-X. Huang, M. A. El-Sayed, J. Adv. Res. 2010, 1, 13.
- 6-M. Hedayati, F. Faupel. J. Materials 2014, 7, 1996.
- 7- C. M. Watts, X. L. Liu, W. J. Padilla. Adv. Mater. 2012, 24, 98.
- 8- J. B. Khurgin. Nat. Nanotechnol. 2015, 10, 2.
- 9- U. Kreibig, C. V. Fragstein. Phys. 1969, 224, 307.
- 10- M. El Kabbash, R. A. Rashed, K. V.Sreekanth, A. De Luca, M. Infusino, G. Strangi. J. Nanomat. 2016, 2016, 1.
- 11- N. M. Lawandy. Appl. Phys. Lett. 2004, 85, 5040.
- 12- G. Strangi, A. De Luca, S. Ravaine, M. Ferrie, R. Bartolino. Appl. Phys. Lett. 2011, 98, 251912.
- 13- A. De Luca, M. P. Grzelczak, I. Pastoriza-Santos, L. M. Liz-Marzan, M. La Deda, M. Striccoli, G. Strangi. ACS Nano. 2011, 5, 5823.
- 14-M. Infusino, A.De Luca, A.Veltri, C. Vazquez-Vazquez, M. A. Correa-Duarte, R. Dhama, G. Strangi. ACS Photonics 2014, 1, 371
- 15- S. Xiao, V. P. Drachev¹, A. V. Kildishev¹, X. Ni¹, U. K. Chettiar, H.-K. Yuan¹, V. M. Shalaev. Nature 2010 , 466, 735.
- 16- O. Hess, J. B. Pendry, S. A. Maier, R. F. Oulton, J. M. Hamm. Nat. Mater. 2012 , 11, 573.
- 17- N. Meinzer, M. Ruther, S. Linden, C. M. Soukoulis, G. Khitrova, J. Hendrickson, J. D. Oltzky, H. M. Gibbs, M. Wegener. Opt. Express 2010, 18, 24140.
- 18-J. Y. Suh, C. H. Kim, W. Zhou, M. D. Huntington, T. D. Co, M. R. Wasielewski, T. W. Odom. Nano Lett., 2012, 12, 5769.
- 19-J. M. Hamm,S. Wuestner, K. L. Tsakmakidis, O. Hess. Phys. Rev. Lett. 2011, 107, 167405.
- 20-M. Quinten, U. Kreibig. Surf. Sci. 1986, 172, 557.

-
- 21- C. Burda, S. Link, T. C. Green, M. A. El-Sayed. *J. Phys. Chem. B* 1999, 103, 10775.
- 22- S. Hunsche, T. Dekorsy, V. Klimov, H. Kurz. *Appl. Phys. B* 1996, 62, 3.
- 23 -X.Wang, Y. Guillet, P. R. Selvakannan, H. Remita, B. Palpant. *J. phys. Chem. B.* 2015, 119, 7416.
- 24- S. Link, M. A. El-Sayed. *J. Phys. Chem. B.* 1999, 103, 8410.
- 25- T. S. Ahmadi, S. L. Logunov, M. A. El-Sayed. *J. Phys. Chem. B* 1999, 100, 8059.
- 26- D. D. Ryutov. *Plasma Phys. Control. Fusion* 1999, 41, A1.
- 27- P. K. Jain, W. Qian, M. A. El-Sayed. *J. Phys. Chem. B* 2006, 110, 136.
- 28 -C. D. Grant, A. M. Schwartzberg, T. J. Norman, J. Z. Zhang. *J. Am. Chem. Soc.* 2003, 125, 549.
- 29- M. J. Feldstein, C. D. Keating, Y.H. Liao, M. J. Natan, N. F. Scherer. *J. Am. Chem. Soc.* 1997, 119, 6638.
- 30- B. A. Smith, J. Z. Zhang, U. Giebel, G. Schmid. *Chem. Phys. Lett.* 1997, 270, 139.
- 31- S. Link, M. A. El-Sayed. *Int. Rev. Phys. Chem.* 2000, 19, 3, 409.
- 32- R. Dhama, A. R. Rashed, V. Caligiuri, M. El Kabbash, G. Strangi, A. De Luca. *Opt. Express.* 2016, 24, 13, 14632.
- 33- R. W. Schoenlein, W. Z. Lin, J. G. Fujimoto, G. L. Esley. *Phys. Rev. Lett.* 1987, 58, 1680.
- 34- R. F. Oulton. *Nat. Phot.* 2012, 6, 219.
- 35- A. R. Rashed, A. De Luca, R. Dhama, A. Hosseinzadeh, M. Infusino, M. El Kabbash, S. Ravaine, R. Bartolino, G. Strangi. *RSC Adv.* 2015, 5, 53245.
- 36- G. Lilley, M. Messner, K. Unterrainer. *Opt. Mater. Express,* 2015, 5, 2112.
- 37- A. De Luca, N. Depalo, N.E. Fanizza, M. Striccoli, M. L. Curri, M. Infusino, A. R. Rashed, M. La Deda, G. Strangi. *Nanoscale* 2013, 5, 6097.

Room temperature dynamic control of spontaneous emission rate using the plasmonic Dicke effect

1. Introduction to lifetime modification in plasmonic nano-cavities:

Ordinary fluorescence arises from the decay of excited quantum emitters to lower states by spontaneous emission (SE) of light where the emitters interact independent from each other with the radiation field. The interaction with the radiation field can be modified by modifying the emitter's electromagnetic environment. In the Wigner-Weisskopf approximation, the SE rate is directly proportional to the electromagnetic local density of states (LDOS) ^{1, 2, 3}. Accordingly, the LDOS can be modified by placing an emitter inside a cavity where the enhanced SE rate is proportional to the ratio of the cavity quality factor Q and modal volume V ($\propto Q/V$); this is the Purcell effect ⁴. Furthermore, when emitters interact with the radiation field coherently due to spontaneous phase-locking of the emitters dipoles, they radiate a field at a faster rate which is linearly proportional to the number of coherent emitters ⁵. The phase-locking requires having multiple emitters in close proximity with inter-distance smaller than the radiation wavelength such that the emitters are indiscernible and the emission of a photon cannot be assigned to a single emitter according to the Heisenberg principle. The phase-locking is mediated by the exchange of virtual photons between the emitters ⁶. The collective emission (*superradiance*) of quantum emitters at a faster emission rate is known as the Dicke effect⁷. Placing quantum emitters near a resonant metallic nanostructure can modify the emitter LDOS due to the excitation of localized surface plasmon polaritons (LSPPs), discrete

collective oscillations of free electrons in response to an oscillating electric field. The excitation of LSPPs allows for strong electromagnetic field confinement which reduces the field's effective modal volume. Excited emitters transfer their energy *independently* to LSPPs which decay into a photon at a faster rate than the radiation rate of emitters in free space. The plasmonic nanostructure functions as an optical nanoantenna which radiates in free space more efficiently. Although the Q -factor of a plasmonic nanostructures is considerably lower than that of a photonic crystal cavity due to strong ohmic and radiative losses in plasmonic nanostructures⁸, considerable SE rate enhancement of emitters coupled to PNCs was recently demonstrated in several works^{1, 9,10,11,12}. The SE rate enhancement using plasmonics, however, is limited. Strong field confinement (lower V) is associated with high ohmic losses and lower Q factors. In addition, while using sharp metallic tips result in extraordinary high field confinement¹³, it is difficult to ensure the spatial overlap between the emitters and the region of high local field intensities.

Quantum emitters can also transfer their energy coherently to LSPPs where the phase-locking is dominated by virtual LSPP exchange rather than direct radiative dipole-dipole coupling⁶. The energy transfer rate is linearly proportional to the number of coherent emitters and the energy transfer rate of independent emitters¹⁴. The surface plasmon mediated coupling, however, is expected to be stronger and more uniform compared to radiation coupling as LSPPs extend throughout the metallic nanostructure which act as a hub that connects nearby and remote dipoles with relatively equal strengths⁶. Albeit its strength, the plasmonic Dicke effect has only been indirectly observed^{15,16}. The existence of a plasmonic nanostructure alters both the decay rate and the quantum efficiency of the

resonant quantum emitter in a nontrivial manner even in the absence of cooperative energy transfer.

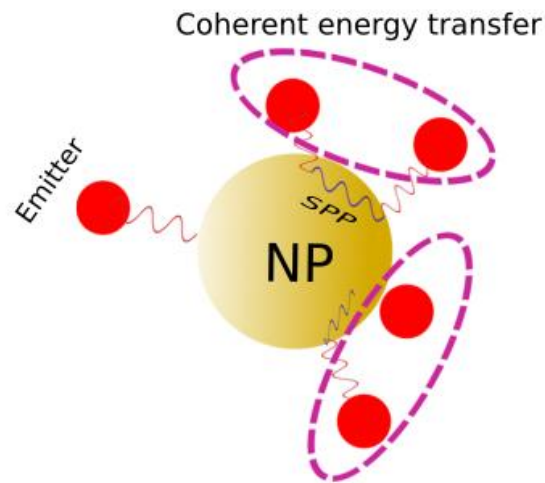


Figure 10 | Schematic of the coherent energy transfer process where multiple emitters (here two emitters) are coupled via a virtual plasmon to coherently transfer their energy to a plasmonic nanocavity at a higher energy transfer rate.

In this letter, we provide a clear demonstration of the plasmonic Dicke effect. We show that the SE rate of quantum dots resonantly coupled to a plasmonic nano-antenna linearly increase as a function of the excitation intensity with a slope proportional to the energy transfer rate of independent emitters. We demonstrate up to six-fold enhancement in the SE rate of CdSe/ZnS quantum dots by varying the excitation intensity. The additional SE rate enhancement due to coherent energy transfer process is of great importance for short distance optical communications which requires low power and high modulation speed light sources^{17,18}. While lasers can provide high modulation speeds (>100 GHz), it requires high power density to operate. On the other hand, spontaneous emission light sources, e.g.,

LEDs, have slow emission rates, and low modulation speeds. Utilizing the plasmonic Dicke effect, the plasmon enhanced SE rate can be further enhanced and potentially exceeds laser light modulation speeds¹⁹. Furthermore, the ability to dynamically control the SE rate of quantum emitters in real time presents a significant challenge due to their short lifetime ($\sim 1\text{ns}$). Recent works (1,2) dynamically controlled the lifetime of quantum emitters at cryogenic temperatures by “molding” the radiation field in real time (1) or by modifying the exciton energy (2). We demonstrate real time, dynamic tuning of the SE rate at room temperature using the plasmonic Dicke effect and reveal its possible application as an optical modulator.

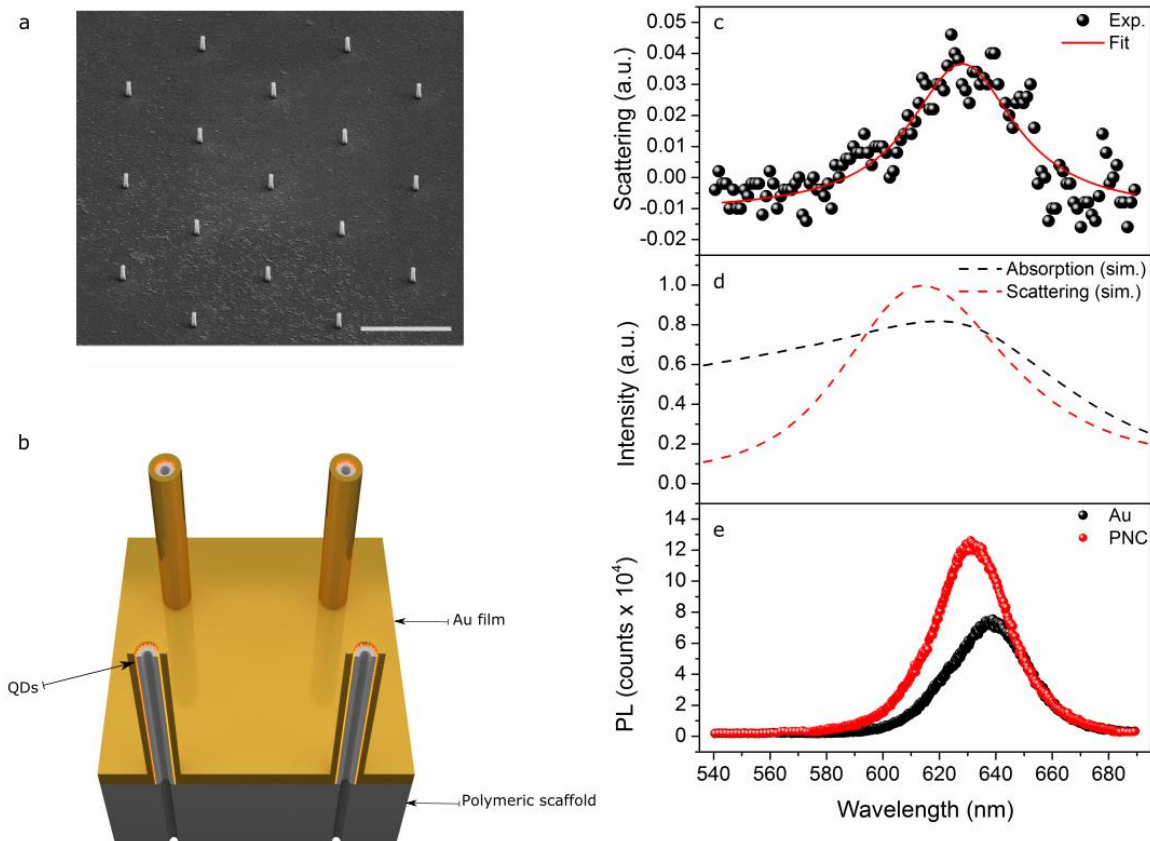


Figure 2 | Characterization of integrated plasmonic nano-cavities: **a**, SEM image of the nano-pillar array (scale bar= $3\mu\text{m}$). **b**, a schematic of the nano-pillar PNC, the QDs are spin-coated on a polymeric scaffold, then an Au layer is deposited. **c**, The measured scattering for nano-pillar array; the resonance maximum was determined by fitting the data with a Lorentzian function. The measured resonance closely agrees with the simulated absorption (black dashed line) and scattering (red dashed line)

presented in **d. e**, Shows the PL of the QD spççin coated on an Au film (black spheres) compared to QD incorporated in a single PNC (red spheres)

2. Results and discussion:

2.1 Sample characterization:

To demonstrate the effect, we fabricated three dimensional, out-of-plane hollow nanostructures (Nano-pillars). Fig. 2a shows an SEM image of an array of the nano-pillars. The nano-pillars are composed of cylindrical polymeric scaffold, 20 nm thick and 450 nm height. We spin-coated CdSe/ZnS quantum dots (QDs) onto which plasmonic shell is formed by coating a 20nm gold layer (see Fig. 2b). The outer and inner diameters of the cavity are approximately 120 and 40 nm, respectively. The fabrication procedure is detailed in the methods section. We use QDs as a quantum emitter due to their strong dipole moment which increases the energy transfer efficiency. In addition, the QD-plasmonic shell inter-distance is fixed and they are only separated by the ligands attached to the QDs. The out-of-plane geometry makes the pillars highly directional. Finally, the large size of the nanoantenna increases the antenna radiative efficiency¹⁸. As we will show, these properties of the fabricated emitter-plasmon system will play an important role in demonstrating the effect. In order to control for other gain-plasmon interactions that are not related to the excitation of LSPPs, we prepared a reference sample where the QDs are spin coated on top of an Au film. The measured and calculated (*Methods*) LSP resonance of the nanopillars are in close agreement as shown in Fig. 2c and 2d respectively. In Fig. 2e we compare the QD photoluminescence (PL) collected from a single nanopillar (red spheres) to PL from the reference sample (black spheres) with excitation intensity 18.5 W. cm^{-2} . The excitation wavelength is $490 \pm 20 \text{ nm}$. The PL maximum is blue shifted from 638 nm (reference) to 631nm (nanopillar) and is pulled towards the LSPP resonance peak ($\sim 628 \text{ nm}$). This clearly indicate that most of the collected PL is from the nanopillar antenna¹³.

2.2 Time resolved lifetime measurements:

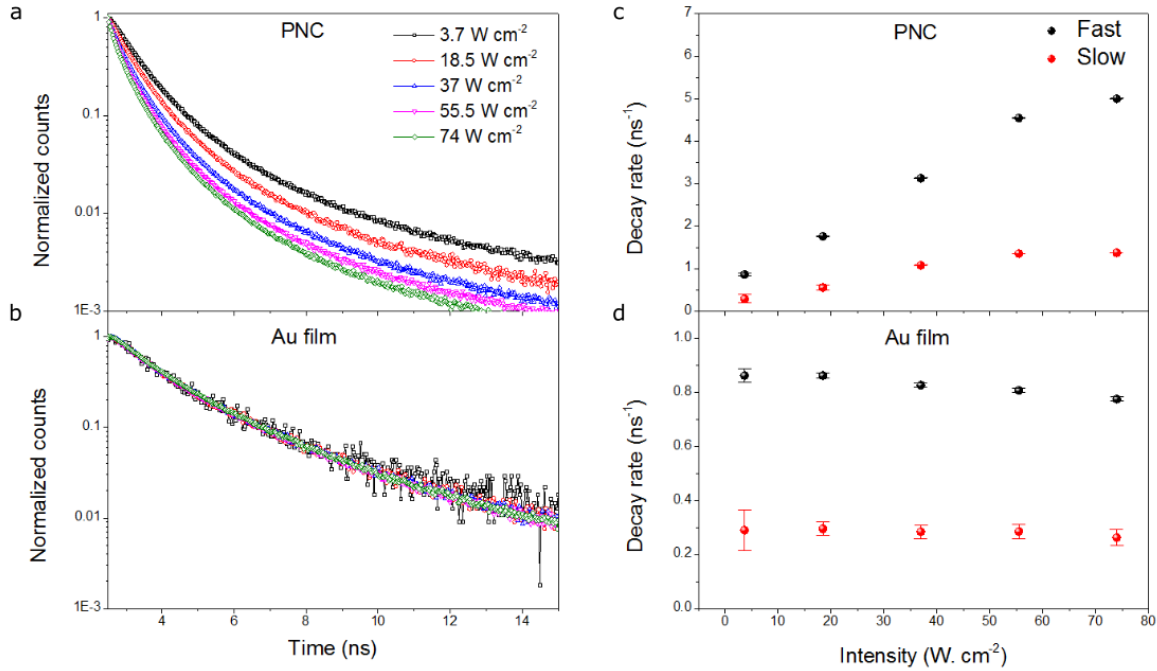


Figure 11 Intensity dependence of SE rate: **a, b** Measured time-resolved QD emission for five different excitation intensities for the PNC (a) and the reference Au film (b). The SE lifetime is intensity dependent for the PNC case only. **c, d** The fitted SE rate fast component (black spheres) and slow component (red spheres) for the PNC and in d, for the reference Au film.

Using a confocal laser setup (*Methods*), we located a single nano-pillar and measured the time-resolved emission of the QDs at emission wavelength 630 nm for a range of pump intensities (3.7 W. cm^{-2} - 74 W. cm^{-2}) and $490 \pm 20 \text{ nm}$ excitation wavelength. Figure 3a and 3b show the time-resolved emission collected from a single nano-pillar and the reference Au film respectively. The measured lifetime for the Au film shows no excitation intensity dependence. On the other hand, the emission lifetime from the nanopillar strongly depends on the excitation intensity. We fitted the time trace of the PL decay with a bi-exponential function and obtained a fast and a slow SE rate components. By increasing the pump intensity, the SE rate increased up to six-fold and fivefold for the fast and slow components respectively.

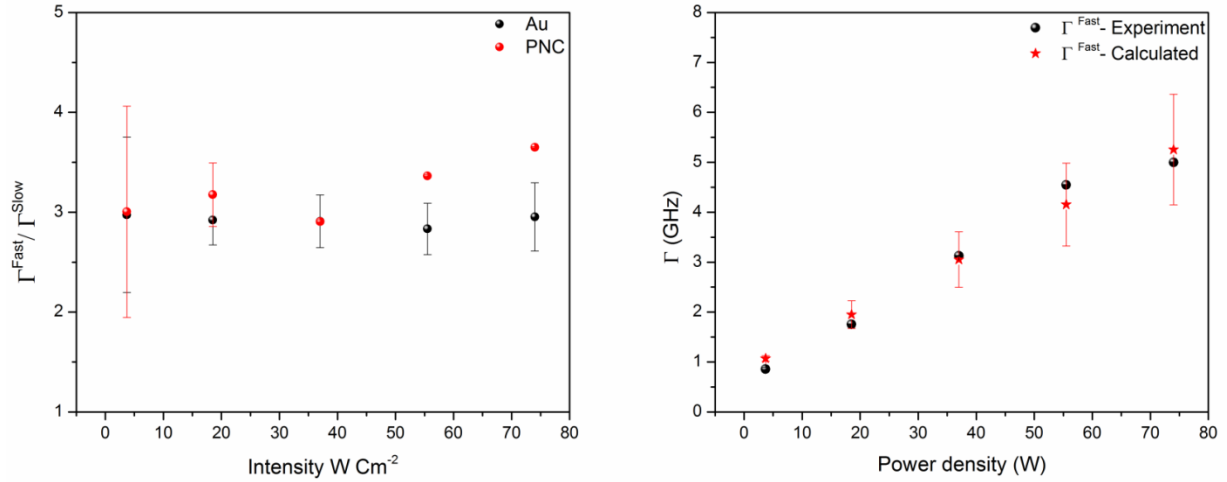


Figure 4| a) The ratio of the fast and slow rates for QDs on an Au film and inside a plasmonic nanopillar. The ratio provides us information about the origin of both rates. According to the statistical scaling law at room temperature, a ratio of 3 corresponds to the excitation of charged biexcitons and charged excitons for the fast and slow rates respectively. For QDs inside the nanopillar, the ratio is maintained indicating that the number of coherent biexcitons and excitons is the same for a given excitation intensity. **b)** Experimental vs. calculated fast SE rate. The calculation was done assuming that the origin of the intensity dependence of the SE rate is due to the plasmonic Dicke effect.

The ratio of the fast and slow rates of QDs on Au film as a function of intensity is ~ 3 (Fig. 4a) which, according to the statistical scaling law at room temperature, indicate that the fast and slow rates correspond to the excitation of charged biexcitons (XX) and charged excitons (X) respectively²⁰. As we detail in the methods section, the SE rate of QDs coupled to the nanoantenna is approximately the energy transfer rate from the excited QDs to LSPs. The linear dependence of the SE rate on the excitation intensity is a signature of cooperative energy transfer. In particular, the cooperative energy transfer rate $\Gamma^c = \sum_i \Gamma_i^{ET}$, where Γ_i^{ET} is the energy transfer rate of individual quantum dots which means that the cooperative energy transfer scales linearly with the ensemble size¹⁴. In general, the energy transfer rate is highly sensitive to plasmon field variations depending on the system geometry and QD separation from metal surface, especially near sharp edges. However, one of the advantages of our cylinder shape nanostructure with spin-coated QDs distributed at similar distances to the metal surface, the energy transfer rate variations within each decay channel are weak. Accordingly, $\Gamma^c \approx N \Gamma^{ET}$, where N is the ensemble size of phase-locked emitters. For low excitation intensities below the

superradiance threshold⁵ cooperative energy transfer does not take place. For intensities higher than the superradiance threshold and below the saturation intensity of the QDs, the ensemble size should scale linearly with the excitation intensity I with some scaling factor α . Consequently, the measured, intensity dependent, SE rate below saturation is given by

$$\Gamma^{\text{Exp}}(I) = \Gamma^{\text{ET}} + \alpha \Gamma^{\text{ET}} I \quad (20)$$

This equation should hold true for both the fast and slow rates. The ratio of the experimentally measured fast and slow rates from the nanopillar (Fig. 4a) is given by

$$\Gamma_{\text{XX}}^{\text{Exp}} / \Gamma_{\text{X}}^{\text{Exp}} = (\Gamma_{\text{XX}}^{\text{ET}} + \alpha_{\text{XX}} \Gamma_{\text{XX}}^{\text{ET}} I) / (\Gamma_{\text{X}}^{\text{ET}} + \alpha_{\text{X}} \Gamma_{\text{X}}^{\text{ET}} I) \quad (21)$$

$\Gamma_{\text{XX}}^{\text{Exp}} / \Gamma_{\text{X}}^{\text{Exp}}$ is also ~ 3 for lower intensities indicating that $\alpha_{\text{XX}} = \alpha_{\text{X}} = \alpha$ within that range. In addition, the measured fast and slow SE rates for the lowest excitation intensity can be taken as a proxy for $\Gamma_{\text{XX}}^{\text{ET}}$ and $\Gamma_{\text{X}}^{\text{ET}}$, respectively. Accordingly, we can quantitatively validate our analysis by, for example, using $\Gamma_{\text{X}}^{\text{ET}}$ to calculate α which we can use it to predict $\Gamma_{\text{XX}}^{\text{Exp}}$. As shown in Fig 4b the calculated and measured $\Gamma_{\text{XX}}^{\text{Exp}}$ are in agreement clearly showing that the SE rate intensity dependence is due to the plasmonic Dicke effect. Finally, the $\Gamma_{\text{XX}}^{\text{Exp}} / \Gamma_{\text{X}}^{\text{Exp}}$ exceeds 3 for higher excitation intensities which is likely to the earlier saturation of excitons compared to biexcitons

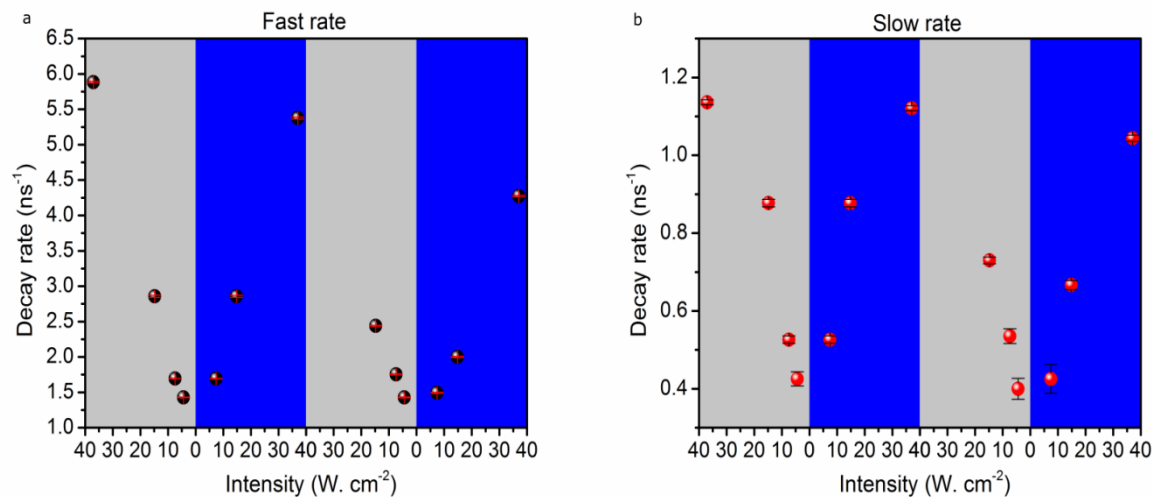


Figure 5|Reversible tuning of SE rate: for a, the fast and b, slow SE rate components. The excitation intensity is decreasing in the grey shaded region and increasing in the blue shaded region.

2.3 All optical modulation of quantum emitter lifetime

In addition to possible optical communication applications, our method can be used for optical modulation. An optical modulator is a device used for manipulating a property of light. In our case, we are interested in the SE rate of an emitter. Figure 5a and 5b show the intensity dependence of the fast and slow components of the SE from a single PNC. The data were collected for four intensities (37, 14.8, 7.4 and 4.4 W. cm⁻²). The grey shaded regions represent decreasing intensity from 37 to 4.4 W. cm⁻² while the blue shaded regions represent increasing the intensity from 4.4 to 37 W. cm⁻². The ability to reversibly tune the SE rate demonstrates complete control on the SE rate establishing the basis for a novel class of optical modulators.

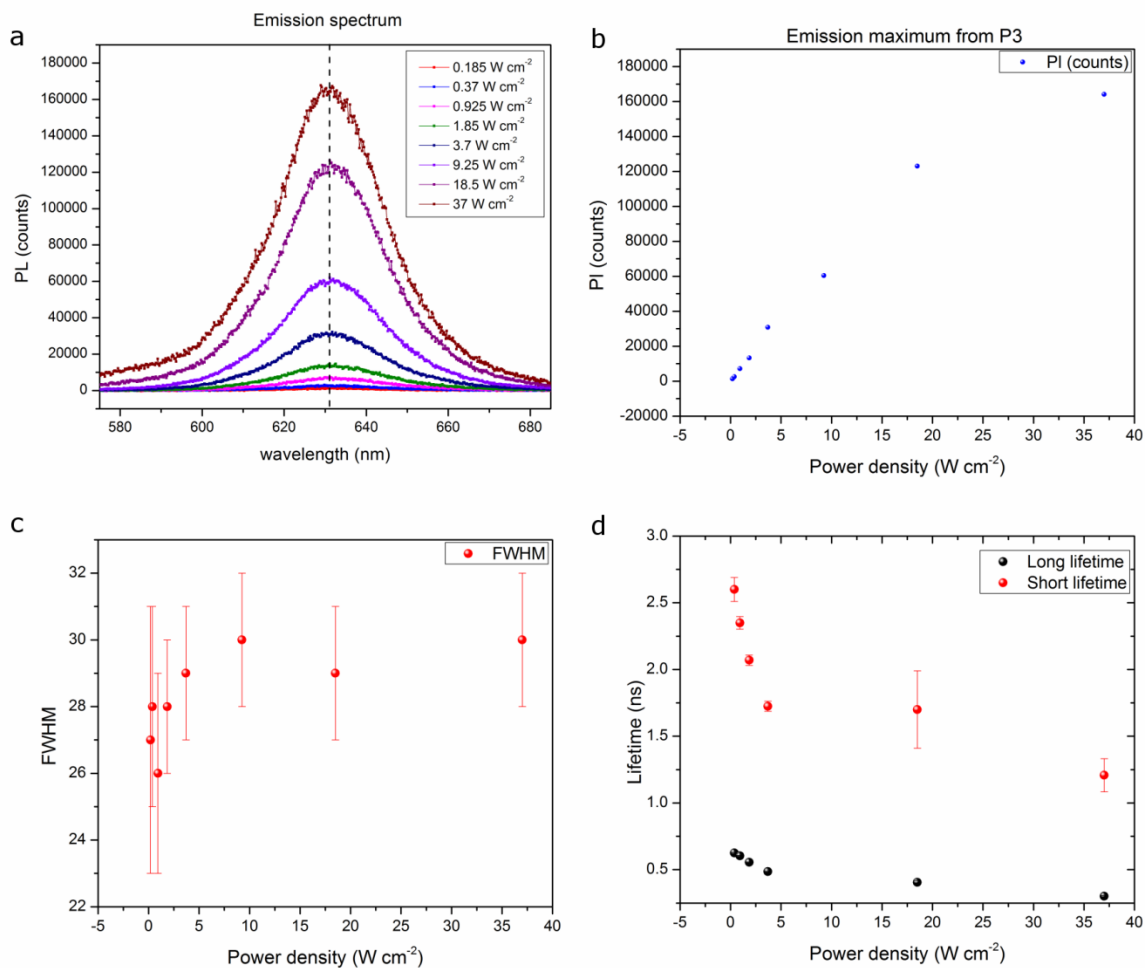


Figure 6 | Absence of stimulated emission: **a)** Photoluminescence spectrum and **b)** its corresponding emission maximum (at 631nm) and **c)** Full-width half maximum. Given that the emission spectrum is neither growing non-linearly at any point nor narrowing, stimulated emission cannot be taking place. **d)** shows the corresponding lifetime components as a function of pump intensity for the same intensity range and on the same nano-pillar.

2.4 Lack of stimulated emission as an alternative mechanism:

Note that the observed effect cannot be due to stimulated emission. Although stimulated emission can decrease the emitters lifetime as a function of intensity, we did not observe any amplification. The amplification experimental fingerprint is the narrowing of the full width half maximum of the emission and a non-linear increase in the emission maximum counts; both features were missing. We show in Fig. 6 the emission spectrum and time resolved lifetime measurements for a single nano-pillar. The PI counts for the excitation intensity range 0.185- 37 W cm⁻² is shown in Fig. 6a. The corresponding emission

maximum and FWHM are shown in Fig 6b and 6c respectively. It is clear that the emission is not undergoing any amplification thus ruling out any significant role of stimulated emission in the lifetime properties of the system. Correspondingly, we see that the lifetime as a function of intensity is decreasing for the same intensity range.

2.5 Excluding plasmonic heating from affecting the measured SE lifetime:

Quantum dots are used as temperature sensors^{24,25} as their emission properties change considerably as a function of temperature. Increasing the ambient temperature of QDs redshifts the emission peak maximum broadens the emission bandwidth and decreases the total emission⁶. In addition, increasing the ambient temperature may change the SE lifetime of QDs, however, it may increase or decrease the SE lifetime depending on the temperature range, and the type and size of QDs under investigation. CdSe QDs show modification in their lifetime properties as a function of temperature^{25,26}. In previous works, the lifetime was investigated at multiple temperature regimes and results showed that for temperatures higher than room temperature, increasing the temperature causes an increase in the lifetime^{25,26}. In all cases, our measurements show that the QDs did not experience plasmonic photo-thermal heating within the investigated power density range. This is evidenced by the fact that the PL peak wavelength did not change as a function of pump power density. We performed these measurements on **P3** (See Fig. 7). The emission spectral properties did not vary as we increased the pump power indicating that the QDs are not sensing any significant change in the ambient temperature. Note that changes up to 5 K have noticeable effects on the emission maximum wavelength investigated in CdSe/ZnS quantum dots²⁵.

In order to exclude any possible effect of plasmonic photo-thermal generation on the QDs lifetime we performed lifetime as well as photoluminescence we performed measurements on infiltrated pillars and varied the pump power by an order of magnitude for each measurement. When we increased the pump power from 40 to 400 microwatts we notice a drop in the total emission counts (Fig. 7) along with broadening of the emission bandwidth and a redshift in the emission peak. These spectral features at high pump power are due to increasing the QDs ambient temperature^{24,25}. We can compare the obtained results to the lifetime measurements at the same pump powers to check the effect of temperature on QDs SE lifetime. Fig. 7 shows that while increasing the pump power reduces the lifetime, at 400 microwatts we get longer lifetime compared to 40 microwatts. This means that increasing the ambient temperature results in increasing the lifetime of the emitters and thus excludes temperature variation as an artifact to our measurements. The short and long lifetime components for 40 microwatts 0.006 ns and 0.25 ns respectively and for 400 microwatts are 0.159 ns and 0.764 ns respectively. This result is in agreement with previous work on similar QDs with similar size ^{26,27}.

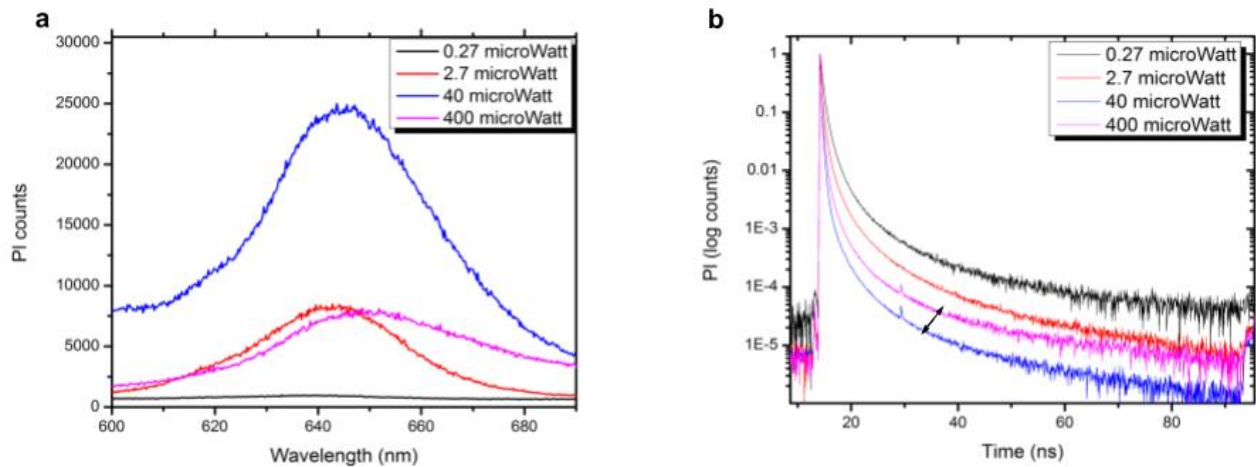


Figure 7 | a, shows the emission spectrum as a function of pump power. In b, we show the corresponding lifetime as we change the pump power. The emission at 400 microwatts resembles that of heated QDs. The corresponding lifetime is longer than the lifetime at 40 microwatts excitation power.

2.6 Spectral shape modification of emission for PNC coupled emitters:

We noted that the change in the QDs emission spectrum on and off the cavity is because PNCs modify the spectral shape of emission as was shown previously by Ringler *et. al.*²⁸. To confirm our observation we fabricated another nano-pillars array . These pillars are 1.8 μm in height and its radius consists of (from the center of the cavity) 40 nm inner cavity radius , 20 nm polymeric shell, 20 nm silver coating and 3.5 SiO layer to avoid PL quenching (Fig. 8a). Then we spin coated the same QDs on top of the sample. Some QDs landed on the tip of the pillars (Fig. 8b) while the rest were on the film. The scattering maximum of these pillars was measured to be at ~ 650 nm (Fig. 8c). The emission of QDs on and off the cavity was collected using a confocal spectroscopy and imaging setup. The focal point was changed and given the height of these pillars we were able to collect either only from the top of the pillars or from the substrate. Fig. 8 shows the normalized emission on and off the

cavity. It is clear that the emission was again shifted toward the resonance maximum of the pillar from ~ 638 nm to ~ 645 nm validating our previous observation. The emission on the pillars is also broader than that of the emission off the pillars. This is likely because the emission is frustrated between two selection rules. One pertaining to the Frank-Condon principle where the emission from a vibrational energy level is preferred which corresponds to the unperturbed maximum emission wavelength of the emitter. The other is related to enhancing the SE emission using the PNC which naturally increases in efficiency for wavelengths with stronger resonant response. If one takes both effects into account, it is straightforward to see why the emission is broadened in the case of a slightly off resonance weakly coupled PNCs.

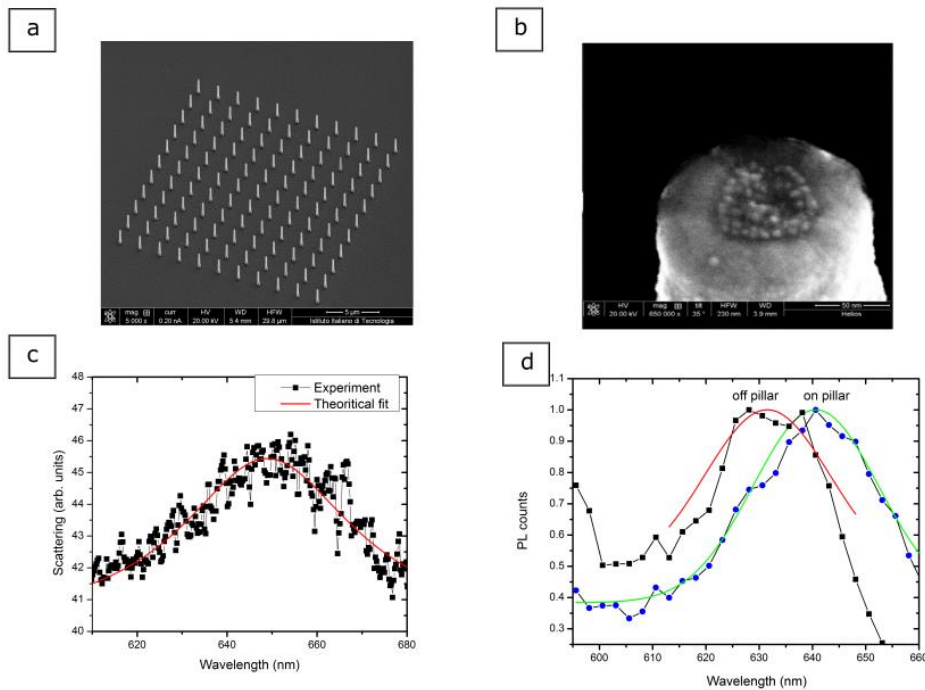


Figure 8 | a, Array of nano-pillars spin-coated with QDs. b, SEM image showing the tip of a pillar where we have QDs landing on its surface. c, The measured scattering of the nano-pillars showing a maximum ~ 650 nm. d, The normalized emission on and off the pillars. The emission on the pillars is redshifted towards the pillars resonant maximum and is broader.

Acknowledgments:

This work was done in collaboration with professor Jesse Berezovsky's group at CWRU at professor Francesco De Angelis group at the Italian Institute of Technology. The authors would like to thank Eugenio Calandrini for his help in sample preparation. G.S. received funding from the Ohio Third Frontier Project 'Research Cluster on Surfaces in Advanced Materials (RC-SAM) at Case Western Reserve University and the GU Malignancies Program of the Case Comprehensive Cancer Center. FDA received funding from the European Research Council under the European Union's Seventh Framework Programme (FP/2007-2013)/ERC Grant Agreement no. [616213], CoG: Neuro-Plasmonics. J.B. received support from U.S. Department of Energy, Office of Science, Basic Energy Sciences, under Award #DE-SC008148.

3-Methods**Sample preparations:****Materials:**

The quantum dots are Lumidot CdSe/ZnS purchased from Sigma-Aldrich (Quantum Dots, QDs, 640 nm emission peak, core-shell type quantum dots, 5 mg/mL in toluene Sigma-Aldrich, Cat No. 680646-2mL).

Fabrication of plasmonic Nano-pillars:

Out-of-plane plasmonic structures have been fabricated by a focused ion beam assisted nanofabrication technique, described in refs. [42, 43] . We herein slightly modified the fabrication process in order to both incorporate the emitters in the vertical structures and infiltrate them in the cavity (Supplementary section 1). Shipley S1813 has been deposited by spin coating onto a 100 nm SiNx membrane. Resist thickness has been adjusted to

achieve the final 450 nm (± 50 nm) nano-pillars height. Polymeric cylindrical scaffold (20 nm wall thickness) is defined by ion milling (Helios Nanolab 620, FEI Co., Hillsboro, OR, USA) to form cylindrical structures. Acceleration voltage was set to be 30 kV with beam current of 40 pA. CdSe/ZnS nanocrystals have been deposited by spin coating (1000 rpm) after dilution to obtain 0.5 mg/mL solution in toluene. Gold (20 nm) was deposited by DC sputter coating in tilted geometry in order to obtain a uniform metal mantle deposited onto gain material. QDs ligands (Hexyldecylamine (HDA), trioctylphosphine (TOPO)) acted as spacer in between gold and CdSe/ZnS. Scanning Electron Microscopy (SEM, Helios Nanolab 620, FEI Co., Hillsboro, OR, USA) was employed to characterize the morphology of fabricated structures. QDs infiltrated structures were prepared by letting diffuse QDs inside nano-pillar cavity. A droplet (10 μ l) of 2.5 mg/ml QDs solution was placed on the backside of the membrane of as-milled nano-pillars. Top-side membrane was placed upside-down and put in contact with pure toluene. This configuration by separating QDs-rich toluene solution from the pure toluene solution allowed creating QDs flux and deposition inside nano-cavities. The samples were kept for 5 minutes in saturated toluene atmosphere, and then washed in pure toluene (Sigma-Aldrich Co. LLC, St. Louis, MO, USA). Finally, gold was uniformly deposited onto QDs infiltrated polymeric scaffolds to form 20 nm layer, as previously described. Fabrication of the reference sample: The reference sample is prepared by first depositing a 5 nm Ti adhesion layer on a glass slide, then we deposited 45 nm Au layer. QDs were spin-coated with the same concentration and spin coating parameters used for the QDs spin-coated on the main sample

Fabrication of the reference sample:

The reference sample is prepared by first depositing a 5 nm Ti adhesion layer on a glass slide, then we deposited 45 nm Au layer. QDs were spin-coated with the same concentration and spin coating parameters used for the QDs spin-coated on the main sample.

Simulating the nano-pillars plasmonic resonance:

All the electromagnetic calculations have been carried out using the commercial software Comsol Multiphysics® (RF module). The refractive index of gold was taken from [44] and the values for PMMA from [45]. For the calculations regarding the out-of-plane antennas (Fig. 1d and 1f.), we assumed a TM polarized plane wave with an angle of incidence of 0° . The simulation domain is enclosed within perfectly matched layers (PML) in order to avoid spurious reflections from the boundaries of the simulation box. The surface is determined by the bottom boundaries of the simulation box and by the metallic bottom-plane.

Experimental setup:**Measuring the LSP resonance of the Nano-pillars:**

We used a Leica DM2500P microscope and attached an Ocean Optics HR4000CG optical fiber to turn it to a spectrometer. By placing the sample under a 100X objective lens with NA 0.75, we were able to collect the scattered light through the objective off and on the nano-pillar array. By taking the difference in the scattered light we obtain the distinct scattering of the nano-pillars which corresponds to its plasmon resonance.

Photoluminescence and fluorescence lifetime measurements:

Excitation is provided by a supercontinuum fiber laser (Fianium SC450PP), outputting ≈ 25 ps duration pulses at a repetition rate of 0.2 MHz. The spectrally broad output of the laser is then filtered by a linearly-graded high-pass and low-pass filter (Edmond optics) mounted on motorized translation stages to tune the cut-on and cut-off wavelengths. The excitation wavelength for the QDs was 490nm with a bandwidth of 20 nm corresponding to its full width half maximum. The excitation (pump) beam is passed through short pass filters with cut-off wavelength of 530 nm. After passing through a 50:50 cube, the beam was then focused on the sample via a 100X objective lens (0.75 NA). The photoluminescence (PL) and scattering is collected again via the 100X microscope objective where we place a long pass 550 nm filter to eliminate the excitation beam when necessary. The PL proceeds to an electron-multiplication CCD (EMCCD) camera/spectrometer to either image the PL or the PL spectrum. By placing the sample on a 3D automated translation stage, we were able to locate the pillars via their PL image. The PL can also be sent to a pair of avalanche photodiodes (APD, PDM-50ct) connected to a time-correlated single photon counting system (TCSPC, Hydraharp 400). The power density was calculated by first measuring the average power before focusing, then determining the beam spot diameter after focusing using the CCD camera. The calculated diameter is ~ 0.6 m.

Confocal pump-probe setup:

Using the same setup for the PL setup for the excitation pump beam we add a collinear probe beam set at 630nm with FWHM 3 nm. The delay was adjusted manually to be (± 0.4 ns). The repetition rate was 0.2 MHz which means that the actual delay for -0.4s delay is $\sim 5 \cdot s$. The delay value was determined using the time-correlated single photon counting

system as it can provide the difference in arrival time for the pump and probe with high accuracy. In order to ensure the complete overlap between the pump and probe beams we used the CCD camera configuration in order to see the exact location of the pump beam, probe beam, and photoluminescence from the nano-pillars. We noticed that the QDs emission drops over time when they are exposed to the pump beam which is likely due to photo-thermal plasmonic heating (Supplementary section 3 and 4). Since the magnitudes of SP-R and SP measurements include the QDs emission, which may decrease over time, we performed the SP measurement ex-ante. This measurement order is chosen to avoid any bias in the results towards supporting our claim, i.e., that SP-R magnitude is greater than the sum of SP and SP separately.

4-References

1. Akselrod, G. M., Argyropoulos, C., Hoang, T. B., Ciraci, C., Fang, C., Huang, J., Smith, D. R., Mikkelsen, M.H. Probing the mechanisms of large Purcell enhancement in plasmonic nanoantennas. *Nat. Photonics* **8**, 835–840 (2014).
2. Pelton, M. Modified Spontaneous Emission in Nanophotonic Structures. *Nat. Photonics*. **9**, 427–435 (2015).
3. Lodahl, P., Driel, A., Nikolaev, I., Irman, A. Controlling the dynamics of spontaneous emission from quantum dots by photonic crystals. *Nature* **430**, 654–657 (2004).
4. Purcell, E. Spontaneous emission probabilities at radio frequencies. *Phys. Rev.* **69**, 681(1946).
5. Gross, M., Haroche, S., *Physics Reports, Review Section of Physics Letters*, 93, 5 301-396 (1982).

-
6. Pustovit, V. N., Shahbazyan, T. V., Cooperative emission of light by an ensemble of dipoles near a metal nanoparticle: The plasmonic Dicke effect , *Phys. Rev. Lett.* **102**, 077401, (2009).
 7. Dicke , R. H., Coherence in Spontaneous Radiation Processes, *Phys. Rev.* **93**, 99 , 1, (1954).
 8. Khurgin, J. B. How to deal with the loss in plasmonics and metamaterials. *Nature Nanotechnol.* **10**, 2–6 (2015).
 9. Russell, K. J., Liu, T., Cui, S. & Hu, E. L. Large spontaneous emission enhancement in plasmonic nanocavities. *Nature Photon.* **6**, 459462 (2012).
 10. Kroekenstoel, E. J. A., Verhagen, E., Walters, R. J., Kuipers, L., Polman, A. Enhanced spontaneous emission rate in annular plasmonic nanocavities *Appl. Phys. Lett.* **95**, 263106 (2009).
 11. Kinkhabwala, A. *et al.* Large single-molecule fluorescence enhancements produced by a bowtie nanoantenna, *Nat. Photonics* **3**, 654-657 (2009).
 12. Goffard, J. *et al.* Plasmonic engineering of spontaneous emission from silicon nanocrystals. *Sci. Rep.* **3**, 2672 (2013).
 13. M. Pelton, G. Bryant, G. Introduction to Metal-Nanoparticle Plasmonics. (Wiley, Science Wise Publishing, Hoboken, NJ, USA, 2013).
 14. Shahbazyan , T. V., Local Density of States for Nanoplasmonics, *Phys. Rev. Lett.* **117**, 207401, (2016).

-
15. Praveena, M., Mukherjee, A., Venkatapathi, M., Basu, J. K., Plasmon-mediated emergence of collective emission and enhanced quantum efficiency in quantum dot films, *Phys. Rev. B*, 92, 235403 (2015).
 16. Mikhail, G., Shestakov, V., Fron, E., Chibotaru, L. F., Moshchalkov, V. V., Plasmonic Dicke Effect in Ag-Nanoclusters-Doped Oxyfluoride, *J. Phys. Chem. C*, 119 (34), 20051–20056, (2015).
 17. D. Miller, *Proceedings of the IEEE*, 97, 7, (2009).
 18. M.S. Eggleston et. al. *Proc. Nat. Acad. Sci.*, 112, 1704–1709 (2015).
 19. Protsenko, I.E., Uskov, A.V., Superradiance of several atoms near a metal nanosphere *Quantum Electronics* 45 (6) 561 – 572 (2015).
 20. Hiroshige, N., Ihara, T., Kanemitsu, Y., Simultaneously measured photoluminescence lifetime and quantum yield of two-photon cascade emission on single CdSe/ZnS nanocrystals, *Phys. Rev. B* 95, 245307 (2017).
 21. Matsuzaki, K., *et. al.*, Strong plasmonic enhancement of biexciton emission: controlled coupling of a single quantum dot to a gold nanocone antenna, *Scientific Reports* 7, Article number: 42307 (2017).
 22. Jin, C.-Y., Johne, R., Swinkels, M. Y., Hoang, T. B., Midolo, L., van Veldhoven, P. J., Fiore, A. Ultrafast non-local control of spontaneous emission. *Nat. Nanotechnol.* 9, 886–890 (2014).
 23. Pagliano, F., Cho, Y., Xia, T., van Otten, F., Johne, R., Fiore, A. Dynamically controlling the emission of single excitons in photonic crystal cavities. *Nat. Commun.* 5, 5786 (2014).

-
24. Thomas, D., Walsh, B. M. and Gupta, M. C. CdSe(ZnS) nanocomposite luminescent high temperature sensor. *Nanotech.* **22**, 185503 (2011).
 25. He-lin ,W. , Ai-jun ,Y. , Cheng-hua, S., Luminescent high temperature sensor based on the CdSe/ ZnS quantum dot thin film. *Optoelectron. Lett.* **9**,6,1 (2013).
 26. Crookera, S. A. , Barrick , T. , Hollingsworth, J. A. , Klimov, V. I. , Multiple temperature regimes of radiative decay in CdSe nanocrystal quantum dots: Intrinsic limits to the dark-exciton lifetime. *App. Phys. Lett.*, **82**,17 (2003).
 27. de Mello Donegá, C. , Bode, M., Meijerink, A., Size- and temperature-dependence of exciton lifetimes in CdSe quantum dots. *Phys. Rev. B*, **74**, 085320 (2006).
 28. Ringler, M., Schwemer, A., Wunderlich, M., Nichtl, A., Kürzinger, K., Klar, T. A., Feldmann, J. Shaping emission spectra of fluorescent molecules with single plasmonic nanoresonators. *Phys. Rev. Lett.* **100**, 203002 (2008).

Tunable Black Gold: Controlling the Near Field Coupling of Immobilized Au Nanoparticles Embedded in Mesoporous Silica Capsules.

Efficient light-heat conversion is central for various applications such as thermophotovoltaics and solar steam generation. Although metals can strongly absorb light and generate heat, their free electrons shield the electric field before any substantial penetration. Excitation of surface plasmons can suppress metal reflection and convert it into a black metal e.g., black gold. Black gold is realized via top-down and bottom-up approaches. Although top-down methods offer flexible and reproducible absorption properties, they are expensive and suffer from low throughput. Bottom-up approaches can be produced on large scale; however, it is difficult to control their absorption properties. In this chapter, we synthesize mesoporous silica capsules grafted with immobilized Au nanoparticles (NPs) with different sizes via controlled chemical synthesis. We show that changing the size of immobilized NPs modifies the inter-particle coupling strength, thus, modifying the NPs absorption. The broadness of the plasmon resonance is tuned across the visible, NIR and short wavelength infrared (SWIR) regions. The proposed approach broadens the possibilities of utilizing black gold in many applications such as thermophotovoltaics, and solar energy harvesting especially in hybrid solar converters [1].

1- Introduction to plasmonic black gold:

Increasing the efficiency and cost effectiveness of solar energy generators allowed them to compete with traditional carbon based energy sources in many energy markets worldwide. However, a major problem facing the proliferation of solar energy generation is energy storage. On one hand, photovoltaic generators enjoy relatively high efficiency but suffer from high electric energy storage costs. On the other hand, concentrated solar power plants collect and store heat and dispatch electricity at lower storage costs but with less efficiency compared to photovoltaics. To address these problems, hybrid solar converters were proposed to optimally exploit the high efficiency of photovoltaics and low costs of solar energy storage [1]. To realize such hybrid solar converters, the excess solar energy not directly used to produce electricity can be stored as heat. This strategy requires developing materials that can efficiently convert light to heat.1 Metallic NPs strongly interact with light oscillating at frequencies near their plasma frequency. The resonant oscillation of free electrons in a NP is called localized surface plasmon resonance (LSPR). Due to high optical losses in metals at resonance, electromagnetic energy is converted into heat; this is the photo-thermal effect in plasmonics [2]. A black metal is metallic structure that absorbs light over the visible spectrum. Although metals are highly reflective due to their negative permittivity, the plasmonic properties of metals in the nano-scale allow them to absorb light efficiently and convert it into heat. The absorption magnitude scales with the strength of the induced polarization and is a maximum at the plasmon resonance. Black metals are realized either by top-down or bottom-up approaches. Top down approaches include lamellar gratings, [3] adiabatic nano-focusing in ultra-sharp convex grooves, [4] nanostructured metallic coatings, [5] and crossed trapezoidal arrays [6]. The absorption

frequency range can be tuned by appropriately choosing the fabrication parameters.

Accordingly, top-down approaches offer a flexible platform for engineering light absorption. However, top-down systems are too expensive and have very low throughput making them impractical to implement. In addition, these designs usually suffer from strong angle and polarization dependence.

Bottom-up approaches include gold smoke deposits, [7] femtosecond laser ablation of metals⁸ and plasmonic colloidosomes [9]. The strong and broad absorption in these systems is due to the inter-particle near field interaction between NP aggregates with random size distribution. Thin-film black gold membranes, however, exhibit broadband absorption via adiabatic nano-focusing of surface plasmons [10]. The relatively low cost and large throughput of bottom up approaches as well as their polarization and angle independence make them a better candidate for practical purposes. However, bottom up approaches suffer from lack of reproducibility and difficulty to control their absorption properties. In order to optimize the energy harvesting efficiency in hybrid solar converters, for example, it is important to be able to control the absorption properties of black metals and that these properties are reproducible on a large scale.

In this work, we present a bottom-up approach to realize tunable omnidirectional light absorption using mesoporous silica capsules embedding immobilized plasmonic Au NPs. The effective immobilization of the particles on the inner surface of the silica shells ensures control over the broadness of the plasmon band by changing the size and inter-distance between the NPs. The broadness of the plasmon resonance is tuned across the visible and NIR (λ : 0.75-1.4 μm) and SWIR (λ : 1.4-3 μm) regions. We highlight the plasmon resonance size dependence of immobilized NPs which differs from well-known plasmon resonance

size dependence of individual [11] or aggregated NPs [19]. Our method, based on a wet chemistry strategy, avoids the complicated fabrication and limitations of top-down approaches while providing considerable control on the system optical properties.

2-Theoretical background:

Broadness of the plasmon resonance in NP aggregates arises from interior and exterior retardation effects. Interior retardation effects occur within a single NP, while exterior retardation occurs among coupled NPs. For mono-dispersed NPs, interior retardation accounts for the broadness of the plasmon resonance. For small NPs resonating at with diameter , only the dipole resonance term dominates the resonance. Accordingly, there exists a certain NP size range (the electrostatic range) where increasing the NP size has no significant effect on the plasmon band broadness. Beyond this range, as the NP size increases, the dipole approximation is invalid and higher order resonances become significant¹¹. Consequently, the plasmon band broadens and its maximum redshifts as a function of the NP size¹¹. Because the field cannot polarize the NP homogeneously, interior retardation takes place and the plasmon resonance band broadens [12].

Exterior retardation effects arise between electromagnetically coupled NPs. Even for NPs with small sizes, if the inter-particle distance between NPs is smaller than the size of the dispersed NPs or if aggregation took place, the plasmon resonance broadens and a second absorption peak starts to appear [11]. Similar to nano-rods, for a given aggregate configuration there are two types of modes; Longitudinal modes where all the dipoles are pointing in the same direction of a given NP chain and transverse modes where the dipoles point perpendicular to the NP chain. The transverse modes do not shift considerably as a function of the number or size of the NPs forming the chain. The longitudinal modes

spectral location depends on the number of the NPs constituting the aggregate and the size of each NP. Larger sizes and numbers correspond to lower energy resonances. This is reminiscent of nano-rods longitudinal mode spectral location dependence on the nano-rod aspect ratio [12]. Note that the effect of NPs size on the plasmon band broadness in a NP chain is significant even if the size of individual NPs lies within the electrostatic regime. A more recent treatment of the effect of NPs coupling is the plasmon hybridization model which draws an analogy between surface plasmon coupling and hybridization of atomic orbitals [18,23]. Coupling surface plasmons of two NPs resonant at a given frequency results in bonding (in-phase) modes that occur at lower frequency and antibonding (out of phase) modes that occur at a higher frequency. Antibonding modes cannot be excited directly by an external field as they are out of phase. In the plasmon hybridization model, NP near-field coupling results in a shift in the plasmon resonance to longer wavelengths. As the inter-particle distance approaches zero, the NPs merge forming an aggregate. The aggregates resonance mode is described as a charge transfer plasmon which takes place at lower energies compared to bonding modes [18].

Another, factor that needs to be taken into account is the size dependence of plasmonic near-field [22]. As the NP size increases, its near-field strength increases and spatially extends to $\sim d/2$, where d is the NP diameter. In small NPs, the existence of electron-surface scattering (Landau damping) attenuates the strength of the localized field. However, for NPs with much larger size ($d > 50$ nm for Au NPs) the near-field strength decreases due to radiative damping and dynamic depolarization effects [22].

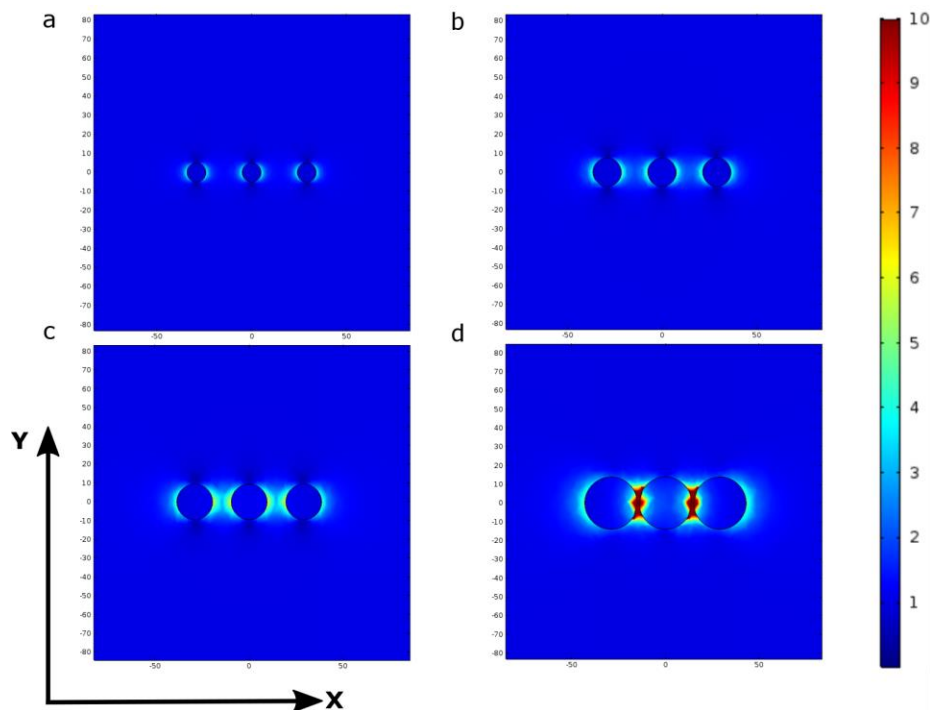


Figure 12| Calculations for local field intensity of Au NPs chain with diameters (a) 10nm (b) 15nm, (c) 19nm, and (d) 28nm. The interaction between the NPs is size dependent due to the reduced inter-particle distance.

3- Results and discussion:

In this work, we explore additional plasmon resonance size dependence. It is well known that the coupling strength between the near fields of two plasmonic NPs depends on the inter-particle distance relative to the NP size [18]. Here we consider the situation where the location of dispersed NPs is spatially fixed. In such case, the coupling strength between the NPs will depend on the NPs size. As the size of each NP increases, the inter-particle distance will decrease and the NPs strongly couple. In addition, the near field of individual NPs extends further spatially as the NP size increases [18]. In this case, not only the NP size determines the spectral properties of the NPs chain as we discussed previously but also it determines the existence and strength of the coupling. The local field intensity calculated

for a chain of three identical spherical Au NPs with diameters 10, 15, 19 and 28 nm is shown in Figure 1 (a), (b), (c), and (d) respectively. The NP centers are fixed and only the diameter is changed. The inter-particle distance between the centers of two adjacent NPs is 29 nm. The E field is polarized in the X direction. In Figure 1. (a) the inter-particle distance is 19 nm; larger than the individual particles size and no interaction between the NPs is observed. By increasing the diameter, the inter-particle distance decreases and the local field of the NPs starts to couple. The coupling strength increases as the inter-particle distance decreases. Calculation details are presented in the methods section.

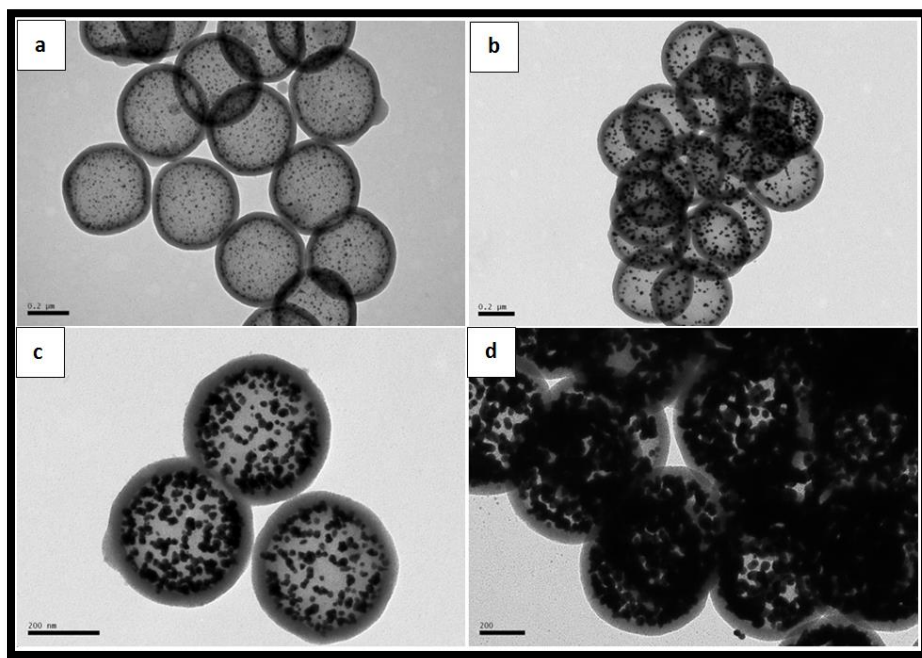


Figure 13| TEM images of Silica shells embedded with pinned Au NPs for (a) S1 (d = 10 nm), (b) S2 (d = 15 nm), (c) S3 (d = 19 nm), and (d) S4 (d = 28 nm). For S1, the NPs are well separated and should exhibit no significant inter-particle coupling. As the NPs size increase in S2, the inter-particle distance becomes smaller than the NPs diameter. Further increase of the NP size in S3 and S4 results in the formation of NP aggregates.

We exploit the size dependence of immobilized NPs to control the absorption properties of Au NPs. In order to realize this system, we synthesized plasmonic structures consisting of a mesoporous silica shell with a diameter of 200 nm, in which Au NPs are grafted on its inner

walls. The effective control over the NPs growth and consequently the average NP inter-

distance was facilitated by the immobilization of the Au NPs used as seeds into the inner walls of the silica capsules. The NPs immobilization was possible due to their partial embedding into the silica shells, which results from the mesoporous silica coating of the polystyrene-coated Au NPs. This ensure that the particles position does not change and only the NP size can be increased by using the well know chemical seeding growth process that offer an accurate control over the nanoparticle size. The synthetic strategy followed in this work is based on previously reported approach [20, 21] although several modifications have been performed to improve the optical properties (detailed in the methods section). We synthesized four samples S1, S2, S3, and S4 with mean NP diameters of ~ 10 nm, 15 nm, 19 nm and 28 nm respectively. The distribution of the NP sizes for all samples is presented in the supporting information.

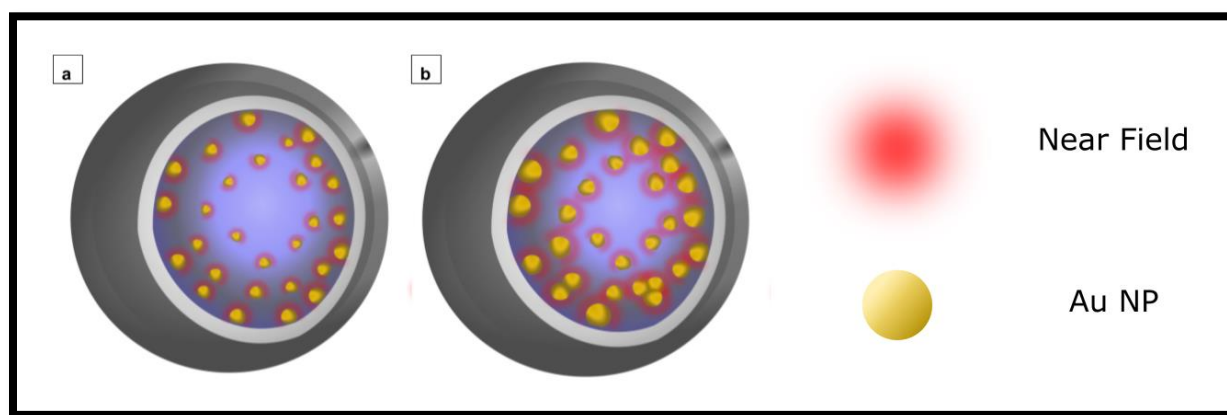


Figure 14|Schematic of mesoporous silica shell with Au NPs: (a) For small size NPs the near field of resonating NPs is not coupled. However, when the NPs size increases as in **(b)** the NPs near fields start to couple resulting in collective resonances and broadening in the plasmon resonance.

TEM images of silica shells embedded with Au NPs are shown in Figure 2 (a), (b) ,(c), and (d) for S1, S2, S3, and S4 respectively. It is visually clear that as the NPs size increases the inter-particle distance decreases. Note that some large NPs start to merge forming

aggregates. Also note that TEM images offer a cross-sectional view of the structure and thus some apparent merger between NPs may not be true.

Figure 3 shows a schematic of a silica shell embedded with Au NPs with small (Figure 3 (a)) and large (Figure 3(b)) NPs. As the size of the NPs increases, the inter-distance between the adjacent NPs decreases and their near fields couples more strongly resulting in broader plasmon resonance.

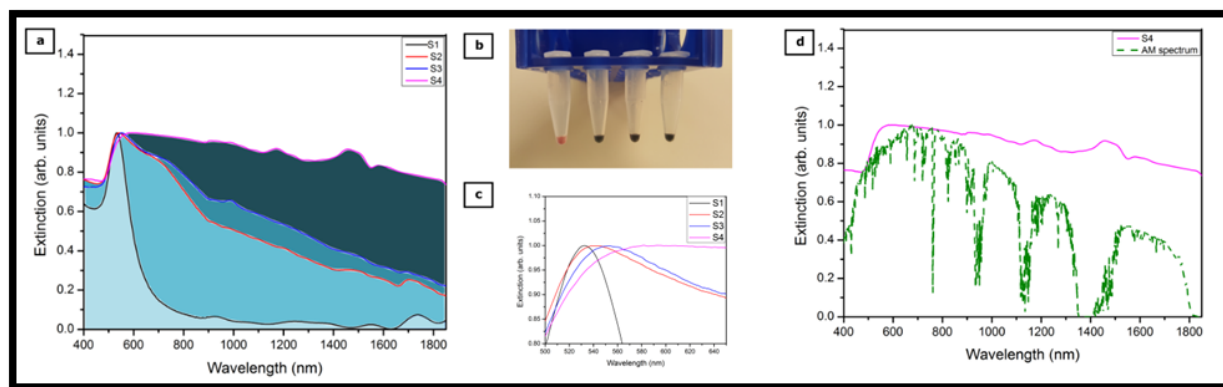


Figure 15| Size dependent plasmon resonance. (a) The measured normalized extinction of **S1**, **S2**, **S3**, and **S4**. The extinction broadens with the decrease of inter-particle distance. In (b) Pictures of **S1**, **S2**, **S3**, and **S4** (from left to right) are shown. It is difficult to see the difference between **S2**, **S3**, and **S4** because they all strongly absorb in the visible. The plasmon band broadening is associated with a redshift in the extinction maximum as shown in (c). We compare the extinction of **S4** with the Air Mass (AM) solar spectrum at sea level in (d). It is clear that **S4** extinction engulfs the AM solar spectrum from the visible to the SWIR.

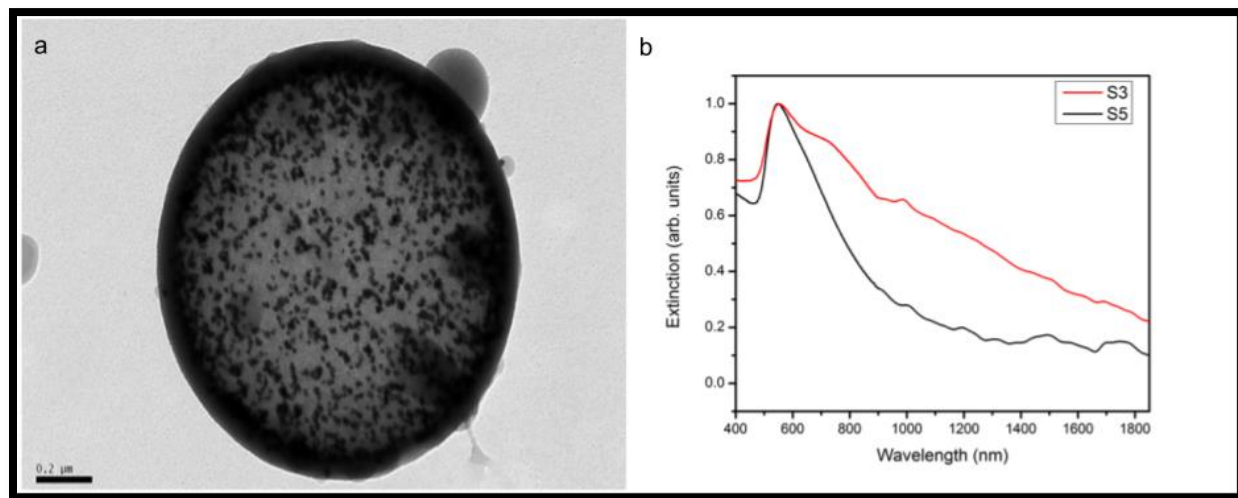
We dissolved the mesocapsules in dimethyl sulfoxide (DMSO) to perform extinction measurements. We chose DMSO because it is relatively transparent in the visible and NIR unlike water that exhibits strong absorption bands in the NIR.¹³ However, DMSO shows strong absorption beyond 1900 nm limiting the spectral range of our investigation.

The extinction measurement and calculation of the four systems are detailed in the methods section. Figure 4 (a) shows the normalized extinction of the four samples. For shells with larger NP sizes, the plasmon resonance band broadens significantly. The estimated full width half maximum (FWHM) of the resonances are 120 nm, 560 nm, 800 nm and 2000 nm for S1, S2, S3, and S4 respectively. Accordingly, we were able to spectrally

tune the plasmon resonance across the visible and NIR and SWIR regions. The FWHM of S4 was calculated by extrapolation of the measured resonance as we could not obtain reliable results beyond 1850 nm due to the DMSO strong absorption. The extrapolation was performed assuming linear decay of the extinction which is the case for the other samples. Figure 4 (b) shows an optical image of the four samples. Note that S2, S3 and S4 demonstrate black gold properties as they absorb over the entire visible spectrum. Compared to the work presented in ref. [9], our system allows for tuning the broadness and extent of the absorption properties of the NPs. In addition, the maximum resonance wavelength is redshifted as we increase the NPs size (Figure 4 (c)). The measured resonance maxima are 532 nm, 538 nm, 552 nm and 581 nm for S1, S2, S3 and S4 respectively. The importance of the wavelength shift is in the possibility to engineer the plasmon resonance. For example, it is possible to suppress the absorption in the visible and shift it further towards the infrared to complement efficient photovoltaic cells that operate in the visible. In figure 4.d. we can see clearly that S4 extinction engulfs the AM solar spectrum at sea level from the visible to the NIR and SWIR regions and possibly the mid wavelength infrared (MIR) region based on our calculated FWHM.

It is very important to stress that the broadness and redshift of the plasmon resonance is not due to interior retardation effects. Even for NPs with mean diameter of 28 nm we are still within the electrostatic regime. Accordingly, the spectral modifications we observe as a function of the NPs size are mainly due to the interactions between different NPs and the formation of aggregates. To illustrate this point further, we synthesized mesoporous silica shells with 184 nm diameter (S5) and average NPs diameter of (Figure 5(a)). The mean diameter of NPs in S3 () is close to that of S5 (see section 1 in the supporting information).

By comparing the extinction of S3 and S5 (Figure 5 (b)), we see that S3 has significantly broader plasmon resonance. It is visually clear that the larger silica shell in S5 allows for the NPs to be well separated resulting in less broadening of the resonance.



. a) TEM image of S5; a 1.34 μm mesocapsule embedding NPs with mean diameter

Figure 16| Effect of individual NP size

~ 18.6 ± 1.5 nm. b) By comparing the extinction of S5 with that of S3 we see that although their NPs share similar size, the plasmon resonance for S3 is significantly broader. By visually examining S5 it is clear that due to the larger surface area of S5 silica shell, the inter-particle distance is larger than that in S3.

In summary, we investigated the plasmon resonance size dependence on immobilized Au NPs grafted on a nano-porous silica shell. We showed that by simply changing the size of the NPs we are able to control the color and broadness of the plasmon resonance providing a significantly broad plasmon resonance for particles with sizes that fall within the dipole approximation range. This method enabled us to create black gold that can strongly absorb in the visible, NIR and SWIR ranges while controlling the broadness of the plasmon resonance which was not possible to realize in previous bottom-up approaches. Our system is a suitable candidate for hybrid solar cell converters. The porous nature of the silica shell would allow in-flow of solvent, e.g., water; inside the mesocapsule (see supporting information, section 3). The plasmonic field confinement creates a nanoscale concentrated

solar energy converter. The strong and broad absorption associated with the plasmon resonance of our structure would allow it to efficiently focus the solar energy and convert it to heat. Future research can produce novel systems that benefit from the plasmon resonance size dependence of immobilized NPs in order to provide cheap and functional plasmonic materials for solar energy conversion.

4-Methods:

Numerical simulation:

Simulations were performed using COMSOL software, which is full wave electromagnetic simulation software based on Finite Element Method. The E field is polarized in the X direction. The normalized field profiles were calculated at the plasmon resonance maximum of individual NPs (~530nm) and plotted in the XY cross section plane. The optical constants of the Au NPs are taken from Johnson and Christy¹⁴. The surrounding medium is presumed to be air.

Extinction measurements:

After dissolving the samples in DMSO, the extinction was measured in two steps. First, we used Uv-Vis (Cary 300 Uv-Vis spectrophotometer) in order to measure the extinction in the visible (400 to 800 nm). To measure the extinction in the NIR region we used variable-angle high-resolution spectroscopic ellipsometry (J. A. Woollam, V-VASE). The extinction of the NPs was excluded by taking the difference between the extinction of the NPs dissolved in DMSO and the DMSO extinction. Taking the extinction difference, however, is not sufficient because adding NPs to the DMSO would dilute the solvent and decrease its extinction. This means that the calculated extinction of the NPs would experience strong troughs when the DMSO is strongly absorbing. On the other hand, the excitation of surface

plasmons localizes the field and enhances the effective absorption of the DMSO¹⁷ resulting in peaks in the differential extinction spectrum. We excluded these troughs and peaks from the results presented in the manuscript. The raw data are presented in the supporting information section 2. For wavelengths longer than 1850 nm light was completely absorbed by the DMSO and we were not able to appropriately calculate the NP extinction.

Samples preparation:

Materials:

Tetraethylorthosilicate 98% (TEOS), ammonium hydroxide solution 28–30%, poly(allylamine hydrochloride) (PAH, 17500 Mw), sodium chloride, tetrachloroauric acid (HAuCl₄·3H₂O), tetrakis(hydroxymethyl)phosphonium chloride solution (THPC), sodium hydroxide, cetyltrimethyl ammonium bromide (CTAB), potassium carbonate, formaldehyde solution (37 wt. %) were purchased from Sigma-Aldrich and polystyrene (PS) beads of 500 nm and 1.4 μm were purchased from Ikerlat. A solution of gold ions pre-reduced to Au⁺ was prepared as described elsewhere.²¹ Pure grade ethanol and Milli-Q grade water were used in all preparations. DMSO was purchased from Cambridge Isotope Laboratory Inc.

Synthesis of nanocapsules AuNPs/mSiO₂ (500nm-1.4μm):

Polystyrene beads functionalization: 25 mL of a solution 1 mg·mL⁻¹ PAH (0.5 M NaCl) were added to the PS beads (12.5 mg) and stirred at room temperature for 30 min. The excess of reagents was removed by four centrifugation-redispersion cycles with pure water (9000 rpm, 40 min).

Deposition of gold nanospheres (AuNPs) onto PS beads: 2.6 nm AuNPs were prepared as described elsewhere.²⁰ Then, 6 and 15 mL of a solution of AuNPs were added to 50 mL

(0.25 mg mL⁻¹) of PAH-functionalized PS beads of 500 nm and 1,4 μm respectively. The mixture was stirred at room temperature for 30 min. In all cases, the excess of AuNP was removed by three centrifugation-redispersion cycles with pure water.

Mesoporous silica coating and hollow capsule preparation of 500 nm: 12.5 mL of PS/AuNSs suspension (1 mg mL⁻¹) was added drop by drop under sonication to a mixed solution of CTAB (312.5 mg), deionized water (125 mL), ethanol (50 mL) and ammonia aqueous solution (1.5 mL, 28 wt%). The resulting solution was homogenized by sonication for 15 minutes. Then, 1.875 mL of a 5% (v/v) TEOS in ethanol was added dropwise to the previous suspension under sonication and was stirred for 17 h. Then it was centrifuge four times and washed with ethanol. Finally, PS and CTAB templates were removed by calcination at 600°C for 4 h and were redispersed in ethanol (10 mL).

Mesoporous silica coating and hollow capsule preparation of 1.34 μm: 1.25 mL of PS/Au suspension (6 mg mL⁻¹) was added drop by drop under sonication to a mixed solution of CTAB (25 mg), deionized water (10 mL), ethanol (7.5 mL) and ammonia aqueous solution (182.5 μL, 28 wt%). The resulting solution was homogenized by sonication for 15 minutes. Then, 250 μL of a 5% (v/v) TEOS in ethanol was added dropwise to the previous suspension under sonication, and was stirred for 17 h. Then it was centrifuge and washed with ethanol four times. Finally, PS and CTAB templates were removed by calcination at 600°C for 4 h and were redispersed in ethanol (10 mL).

Confined growth of the AuNPs for the final preparation of samples (S1, S2, S3, S4, S5): S1 was the previously obtained mesoporous silica Au capsules of 500nm. S2 and S3 were prepared adding 12 or 20 mL of Au⁺ solution, and 12.5 or 20 μ L of formaldehyde solution (37 wt. %) to a 5 mL of S1 (1 mg mL⁻¹) under vigorous stirring respectively. S4 was prepared adding 7.5 mL of Au⁺ solution and 7.5 μ L of formaldehyde solution (37 wt. %) to 1.25 mL of S1 (1.25 mg mL⁻¹). The sample S5 (1.32 μ m) was obtained adding 6 mL of Au⁺ solution and 6 μ L of formaldehyde solution (37 wt. %) to 2 mL of previously prepared 1.32 μ m mesoporous silica Au capsules (0.75 mg mL⁻¹). The samples were centrifuged and washed with ethanol four times.

Acknowledgments:

This work was done in collaboration with professor Miguel A. Correa-Duarte, at the University of Vigo, Spain. The research leading to these results received support and funding from the Ohio Third Frontier Project Research Cluster on Surfaces in Advanced Materials (RC-SAM) at Case Western Reserve University. This work was funded by MINECO-Spain (Grant No. CTM2014-58481-R) and Fundación Tatiana Pérez de Guzmán el Bueno.

This work was published in the following article: “ Mohamed ElKabbash, Ana Sousa-Castillo, Quang Nguyen, Rosalia Mariño-Fernández, Nathaniel Hoffman, Miguel A. Correa-Duarte, Giuseppe Strangi, Tunable Black Gold: Controlling the Near-Field Coupling of Immobilized Au Nanoparticles Embedded in Mesoporous Silica Capsules, 5, 21 November, 1700617, 2017.

5. References

1. H. M. Branz, W. Regan, K. J. Gerst, J. B. Borakac , E. A. Santoria , *Energy Environ. Sci.*, 2015, 8, 3083-3091.
2. A. O. Govorova, H. H. Richardson, *Nano Today*, 2007, 2, 1, 30–38.
3. N. Bonod, G. Tayeb, D. Maystre, S. Enoch, E. Popov, *Opt. Express* , 2008, 16, 15431–15438.
4. T. Søndergaard, S. M. Novikov, T. Holmgaard, R. L. Eriksen, J. Beermann, Z. Han, K. Pedersen , S. I. Bozhevolnyi, *Nat. Comm.* 2012, 3, 969.
5. V. G. Kravets, F. Schedin, A. N. Grigorenko, *Phys. Rev. B* , 2008, 78, 205405.
6. K. Aydin, V. E. Ferry, R. M. Briggs , H. A. Atwater, *Nat. Comm.*, 2011, 2, 517.
7. D. R. McKenzie, *Gold Bull.* 1978 ,11 ,49. See [109, 140]
8. A. Y. Vorobyev, C. Guo, *Phys. Rev. B* , 2005, 72, 195422.
9. D. Liu, F. Zhou, C. Li, T. Zhang, H. Zhang, W. Cai, Y. Li, *Angew. Chem*, 2015, 54, 33 , 10,9596–9600.
10. K. Bae, G. Kang, S. K. Cho, W. Park, K. Kim, W. J. Padilla, *Nat. Comm.* 2015, 6, 10103 10103.
11. S. Link, M. El-Sayed, *Int Rev Phys Chem.* 2000, 19, 3, 409-453.
12. M. quinten and U. Kreibig, *Surf. Sci.* 1986 172(3), 557-577.
13. V. M. Wallace, N. R. Dhumal, F. M. Zehentbauer, H. J. Kim,, J. Kiefer, *J. Phys. Chem. B*, 2015, 119 (46), pp 14780–14789.
14. P. B. Johnson , R. W. Christy, *Phys. Rev. B: Solid State*, 1972, 6, 4370.
15. D. G. Duff, A. Baiker, P. P. Edwards, *Langmuir* 1993, 9, 2301.

-
16. T. Pham, J. B. Jackson, N. J. Halas, T. R. s. Lee, *Langmuir* 2002, 18, 4915–4920.
 17. N. Lawandy, *Proc. SPIE* 5924, 2005, *Complex Mediums VI: Light and Complexity*, 59240G.
 18. M. Pelton, G. Bryant, G. Introduction to Metal-Nanoparticle Plasmonics. Wiley, Science Wise Publishing, Hoboken, NJ, USA, 2013.
 19. S. K. Ghosh, T. Pal, *Chem. Rev.* 2007, 107, 4797
 20. M. Sanlés-Sobrido, W. Exner, L. Rodríguez-Lorenzo, B. Rodríguez-González, M. A. Correa-Duarte, R. A. Alvarez-Puebla, L. Liz-Marzán, *J. Am. Chem. Soc.* 2009, 131, 2699–2705.
 21. M. Sanlés-Sobrido, M. Pérez-Lorenzo, B. Rodríguez-González, V. Salgueiriño, M. A. Correa-Duarte, *Angew. Chem., Int. Ed.* 2012, 51, 3877–3882.
 22. C. Deeb, X. Zhou, J. Plain, G. P. Wiederrecht, R. Bachelot, M. Russell, P. K. Jain. *J. Phys. Chem. C.* 2013, 117,10669-10676.
 23. M. El Kabbash , A. R. Rashed, K. V. Sreekanth, A. De Luca, M. Infusino , G. Strangi. *J. Nanomat.*, 2016, 21.

Active thin-film Metamaterials

In general, for non-luminous objects, color is of two types. *Chemical colors* caused by pigment absorption, and *structural colors* if the color is produced due to other fundamental optical processes such as refraction, reflection or transmission [1].

Structural colors are sub-divided to **prismatic colors** and **interference colors**. The former is due to the dispersion of light inside refractive media, and the latter is due to interference. The first example of metamaterials is that of interference based structural colors. Through millions of years of evolution, nature cracked down nano-technology by creating sub-wavelength structures that cause interference of reflected light resulting in an iridescent color such as that of a peacock feathers or a butterfly wing. Similarly, it is possible to create a metamaterial out of multiple thin-films to create interference effects. In this thesis, we focus mainly on interference based thin-film metamaterials to which we will lay the theoretical ground in the next sub-sections. However, it is important to note that thin-film metamaterials comprise a diverse array of systems. This is because the phase of light can be tailored through careful choice of materials and thicknesses of thin-film stack in order to realize metamaterials with exotic optical properties such as epsilon-near zero metamaterials[2], negative index metamaterials [3], and hyperbolic metamaterials [4].

The first chapter provides a review on the basics of thin-film interference. The second chapter presents our work on iridescent free thin-film light absorbers based on Fabry-Perot resonances. The third chapter deals with the application of the Fabry-Perot cavity

absorber for gas sensing. The fourth chapter introduces a novel optical-coating light absorber based on a low-loss dielectric on a high-loss metal film which we exploit as an active metamaterial for Hydrogen gas sensing in chapter five.

Active interference based thin-film metamaterials

This part deals with thin-film metamaterials that we studied over the past year and the ability to actively tune their optical properties. Research in metamaterials aims to change the properties of materials, not by changing their chemistry, rather by changing their structure at length scales shorter than the wavelength range of interest. In active metamaterials, the structure-based properties of a metamaterial are affected by external stimuli. The induced change in the active metamaterial properties can be harnessed in many applications such as sensing, data-storage, and display technologies. In this section, we discuss the basic principles pertaining to interference based thin-film metamaterials and then focus perfect light absorption in thin-films.

The theory of thin film interference is covered in basic text books [5-7]. For the sake of completeness, we discuss the basic principles of interference, and then we focus on Fabry-Perot type interference using a combination of dielectric and metallic thin films.

1. Interference; a brief overview:

Assuming monochromatic plane waves, interference from two linearly polarized beams depends on the net intensity of the superimposed beams I_{net} such that

$$I_{net} = |\vec{S}| = \frac{|\vec{E} \times \vec{B}|}{\mu_0} \quad (22)$$

where S is the pointing vector, E is the net electric field, B is the net magnetic field and μ_0 is the free space magnetic permeability.

For plane waves, the net electric and magnetic fields are perpendicular and the magnitude of the magnetic field is equal to that of the electric field with a factor of the inverse of the speed of light. The time averaged net intensity $\langle I \rangle$ is given by

$$\langle I \rangle = \frac{1}{2 \mu_0} EB^* = \frac{1}{2 c \mu_0} EE^* \quad (23)$$

where B^* and E^* are the conjugate net magnetic and net electric fields respectively. For interfering parallel electric fields, the net electric field is given by their superposition. For two electric fields E_1 and E_2 with magnitudes E_{01} and E_{02} that differ by a non-trivial phase δ , we have

$$E_1 = E_{01} e^{-i\omega t} \quad (24)$$

$$E_2 = E_{02} e^{-i\omega t + i\delta} \quad (25)$$

$$E = E_1 + E_2 = (E_{01} e^{-i\omega t} + E_{02} e^{-i\omega t + i\delta}), \quad (26)$$

$$\begin{aligned} \text{then } EE^* &= E_{01}^2 + E_{02}^2 + 2 E_{01} E_{02} \left(\frac{e^{-i\delta} + e^{i\delta}}{2} \right) \\ &= E_{01}^2 + E_{02}^2 + 2 E_{01} E_{02} (\cos \delta) \end{aligned} \quad (27)$$

$$\text{Let } I_{01} \equiv \frac{1}{2 c \mu_0} E_{01}^2, I_{02} \equiv \frac{1}{2 c \mu_0} E_{02}^2 \text{ \& } I_{1,2} \equiv \frac{1}{2 c \mu_0} 2 E_{01} E_{02} (\cos \delta) \quad (28)$$

$$\text{then } \langle I \rangle = I_{01} + I_{02} + I_{1,2} \quad (29)$$

where $I_{1,2}$ is the interference term which can have negative values. It is straightforward to see that the phase difference between the electric fields determine the intensity of the net field which has a minimum and maximum corresponding to a phase of an odd and even multiple of π respectively. A very important case is when the two fields with equal magnitudes

$$E_{01} = E_{02} = E_0, \text{ then } I_0 = \frac{1}{2 c \mu_0} E_0^2 \text{ and } \langle I \rangle = 4I_0 \left(\cos \frac{\delta}{2}\right)^2 \quad (10)$$

the interference pattern contrast is stronger and the minimum intensity is 0 for total destructive interference and maximum is $4I_0$ for total constructive interference.

Interference can be categorized into *wave-front splitting* interference and *amplitude splitting* interference [6]. The wave-front splitting interference is when a primary wave-front is split into two or more wave-fronts that are later brought together to interfere. The amplitude splitting interference is when the amplitude of the primary wave-front is divided into two or more segments which travel in separate paths and then combine together to interfere. We are interested here in amplitude splitting interference [6].

2. Amplitude splitting interference in thin films:

If a wave is incident on a semi-reflective surface, part of it will be reflected and the other part will be transmitted. Since both reflected and transmitted waves have lower amplitudes than the incident wave, one can consider this as amplitude splitting. If the two waves are brought together at a later point, then they can interfere. In order for light to interfere, however, the waves must be spatially and temporally coherent.

Accordingly, both waves must travel through a distance that is smaller than the coherence length of the incident wave before they are brought together. This is why in order to observe amplitude splitting interference, we need a *thin-film*; a layered material of thickness that is in the order of the wavelength of interest.

We are interested in a particular type of amplitude-splitting interference schemes; the Fabry-Perot thin-film interference.

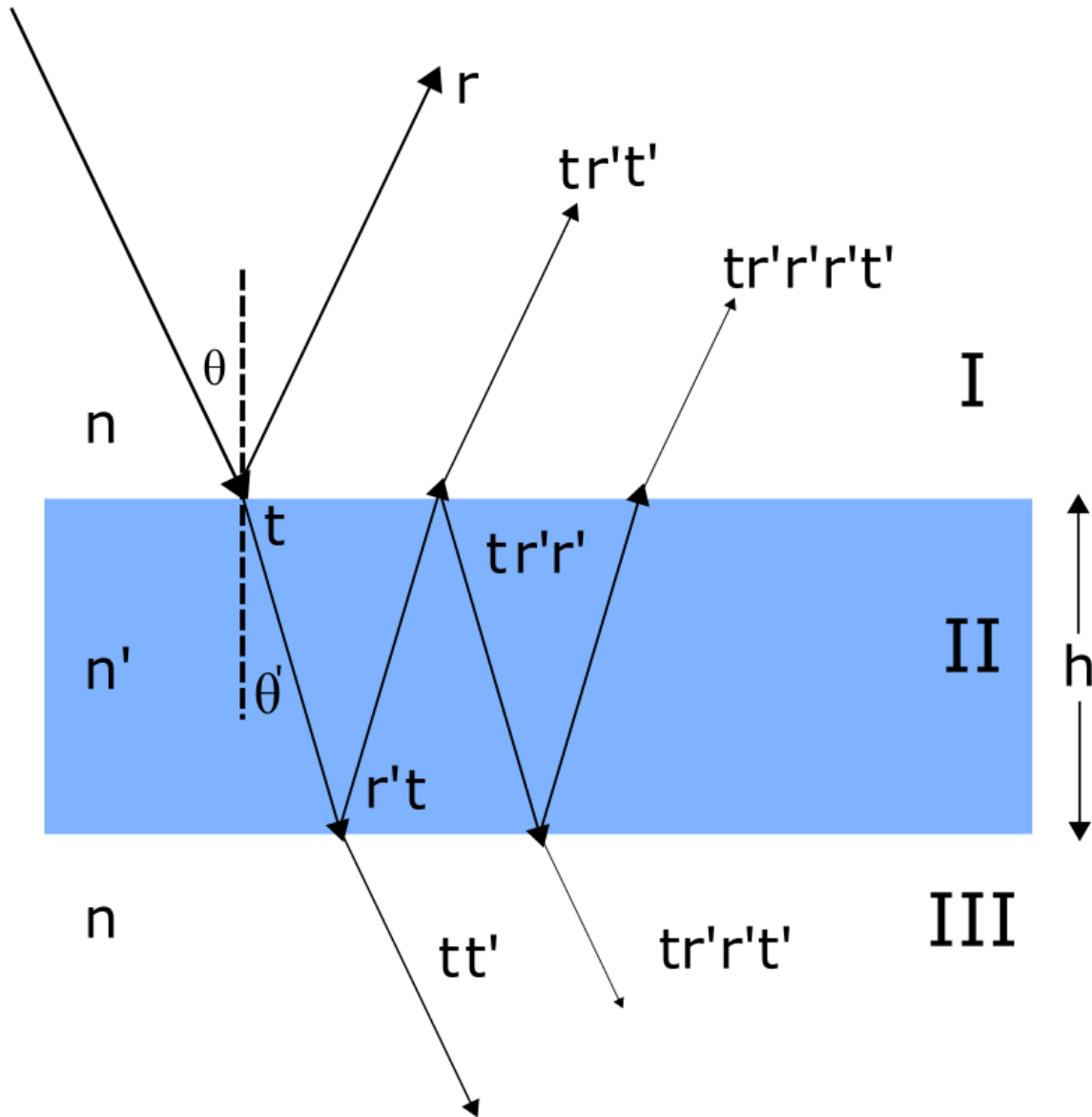


Figure 1 Fabry-Perot interference in dielectric thin films

For the case of a dielectric thin-film (Fig. 1) with thickness h and refractive index n'

sandwiched between two identical dielectric infinite media with refractive index n . A wave

travelling from medium I to II, let r and t be the reflection and transmission coefficients

respectively. For a wave travelling from medium II to I or III, let r' and t' be the

corresponding reflection and transmission coefficients. For a dielectric thin-film, Stoke's

relations dictates that $r' = r$ and $tt' = 1 - r^2$. We define the transmissivity as $T \equiv tt'$,

and the reflectivity as $R \equiv r r'$. The difference in phase between each two successive beams reflected or transmitted through the dielectric film is twice the optical thickness of the film. The phase difference here informs us about the fraction of the wavenumber (phase) that has changed due to double traversing through the film at a given angle and it is given by $\delta = \frac{4\pi}{\lambda_0} n' h \cos \theta' \pm \pi$. The additional π shift is due to the obtained phase shift from reflection off I-II or II-III interfaces. Note that for higher angles, the *phase thickness* decreases and retaining back the same phase thickness requires a decrease in the incident wavelength λ_0 (blue shift).

The normalized reflected intensity I^r with respect to the incident intensity I^i is

$$\frac{I^r}{I^i} = \frac{F \sin(\delta/2)^2}{1 + F \sin(\delta/2)^2} \quad (30)$$

where F is the coefficient of fineness defined as $F \equiv \left(\frac{2r}{1-r^2}\right)^2$. F is proportional to the reflectivity and determines the broadness of the transmitted wavelength range.

Considering that there is no absorbance, $1 = R + T$, the normalized transmitted intensity is then given by

$$\frac{I^t}{I^i} = \frac{1}{1 + F \sin(\delta/2)^2} \quad (31)$$

Note that even for high values of r , if $\delta/2 = m\pi$ and m is an odd number, then the reflected intensity is zero indicating the existence of destructive interference.

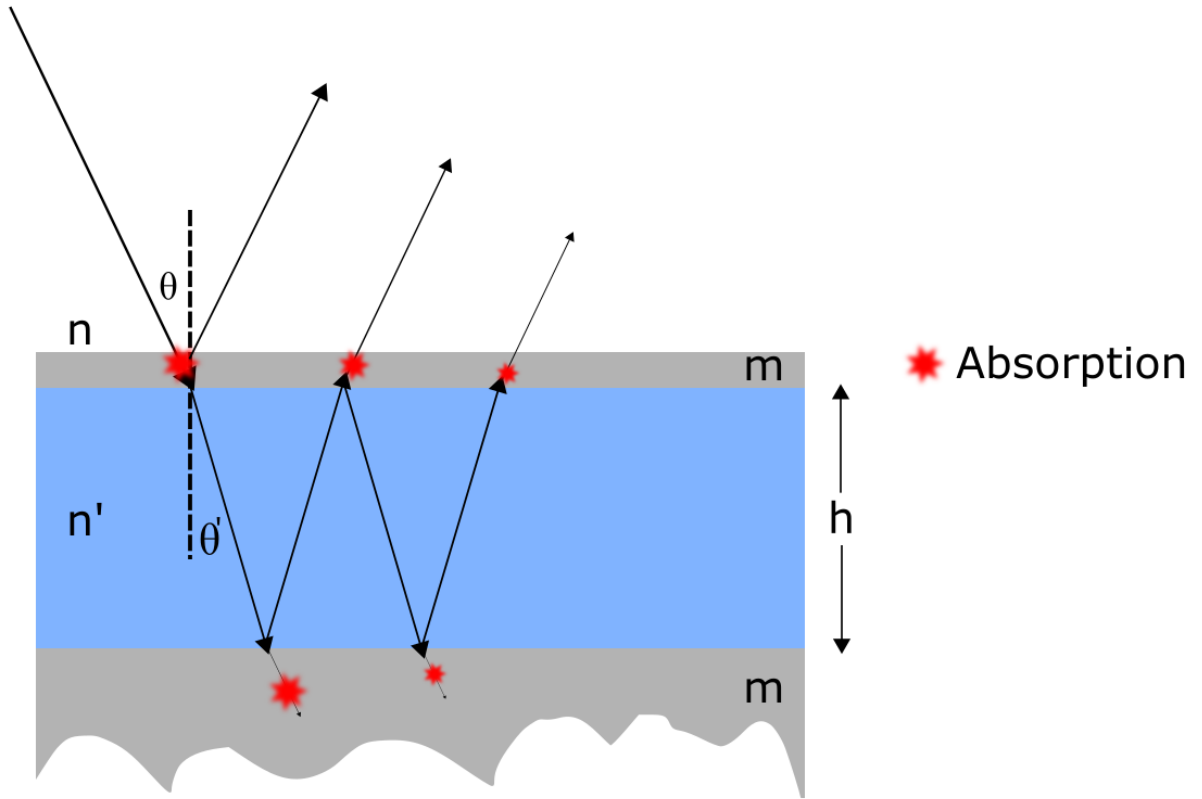


Figure 2: Fabry-Perot etalon with an infinite bottom metal film.

Introducing semi-transparent metal films creates a FP etalon (Fig. 2). Adding metallic thin-films introduces absorption due the existence of oscillating free charges with absorptivity A as well as an additional non-trivial phase ($\phi \neq 0$ or π) unless it the metal film is a perfect electric conductor. The conservation of energy, then, dictates that $T+R+A = 1$, the transmitted intensity is given by

$$\frac{I^t}{I^i} = \left(1 - \frac{A}{1-R}\right)^2 \frac{1}{1 + F \sin(\delta/2)^2} \quad (32)$$

The reflected intensity would naturally have a different expression; however, it will still

maintain the phase factor $\sin(\delta/2)^2$, where $\delta = \frac{4\pi}{\lambda_0} n' h \cos \theta' + 2\phi$ with an added

2ϕ term because of the existence of two metal films. If the phase factor satisfies $\delta/2 = m\pi$,

then I^r will also be zero. If we used a thick metal film as shown in figure 3, then

transmission will also be zero. This means that all light will be absorbed; this is perfect light absorption. Note that this effect occurs even if the metal films are highly reflective. Several works have demonstrated broad and narrow band light absorption using a FP metal-dielectric-metal films (MDM) [8, 9]. The absorption spectral location depends on the wavelength range that satisfies the total destructive interference condition for a given MDM cavity thickness. Since the phase thickness δ depends on the incidence angle, the absorption mode spectral location is angle dependent, i.e., iridescent. As we will show in later sections, we provide a simple solution to the iridescence problem in FP MDM cavities. Finally, while we follow the literature in calling the MDM absorbers as FP etalons or cavities, these are Gires–Tournois (GT) etalons since they operate in reflection mode. The main difference is that traditional GT etalons operate with very low losses (usually using dielectric bragg mirrors) while here we have finite losses due to using metals which are particularly lossy in the optical regime , i.e., visible and NIR regimes.

3. Optical coating perfect light absorbers:

Here we address the ability of light absorption using ultrathin film coatings. The condition where perfect light absorption occurs in a metal-dielectric-metal FP etalon was simply having complete destructive interference and trapping light inside the cavity such that light is absorbed due to the finite absorption of the metal film. This case assumes that the first reflected beam from the top metal layer is *equal* in magnitude to the sum of all beams reflected from the bottom layer which is equivalent to the case addressed in equation 10.

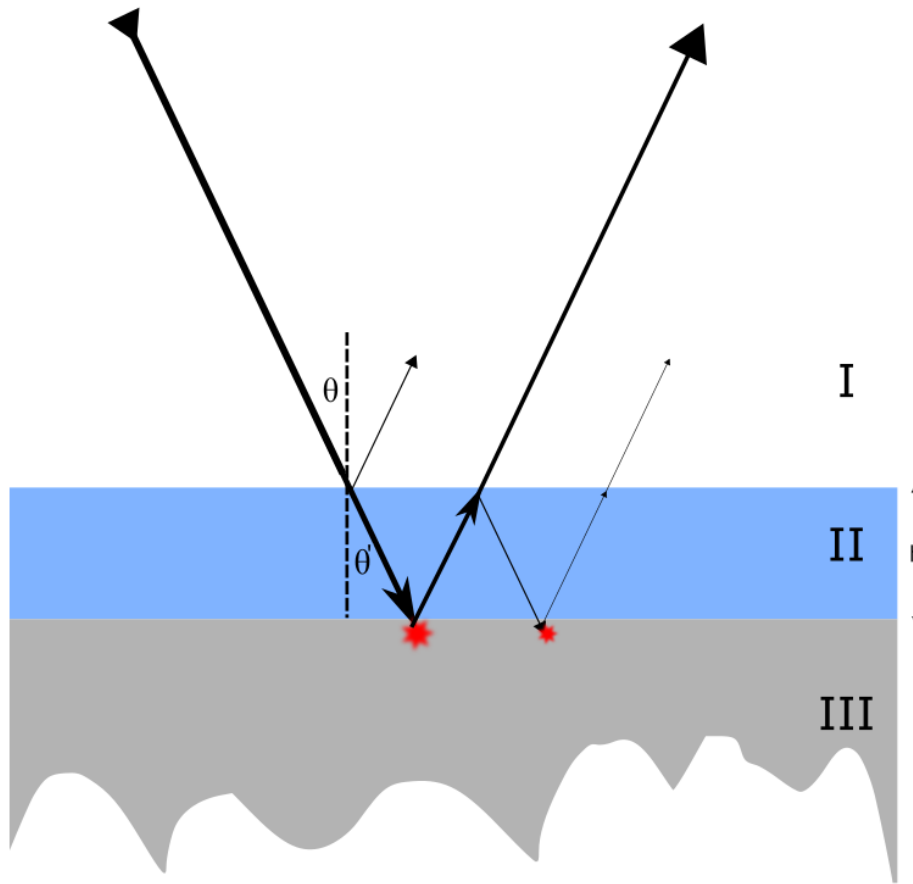


Figure 3|Lossless dielectric thin-film coating on a metal with finite conductivity. Light suffers limited absorption as it reflects from the metal, however, most light intensity escapes the resonator due to the weak reflection from the dielectric at the I-II interface compared to the reflection from the metal-dielectric II-III interface.

For an optical coating, we are limited to having a single dielectric layer coating a substrate that can be metallic. Given the low reflection of dielectrics compared to metals, placing a dielectric on a metallic film is unlikely to create perfect light absorption. In fact, it has been recently claimed that coating a metallic film with a **lossless dielectric** *cannot* result in strong light absorption (see figure 3) [10]. We will show in the following sections that it is possible to realize perfect light absorption even for lossless dielectric coatings. What is universally true, however, is that if a lossless dielectric thin film coated a metal behaving as a perfect electric conductor (PEC), the system cannot exhibit any losses even if the

condition of destructive interference was satisfied and the metallic film is infinitely thick such that no transmission exists.

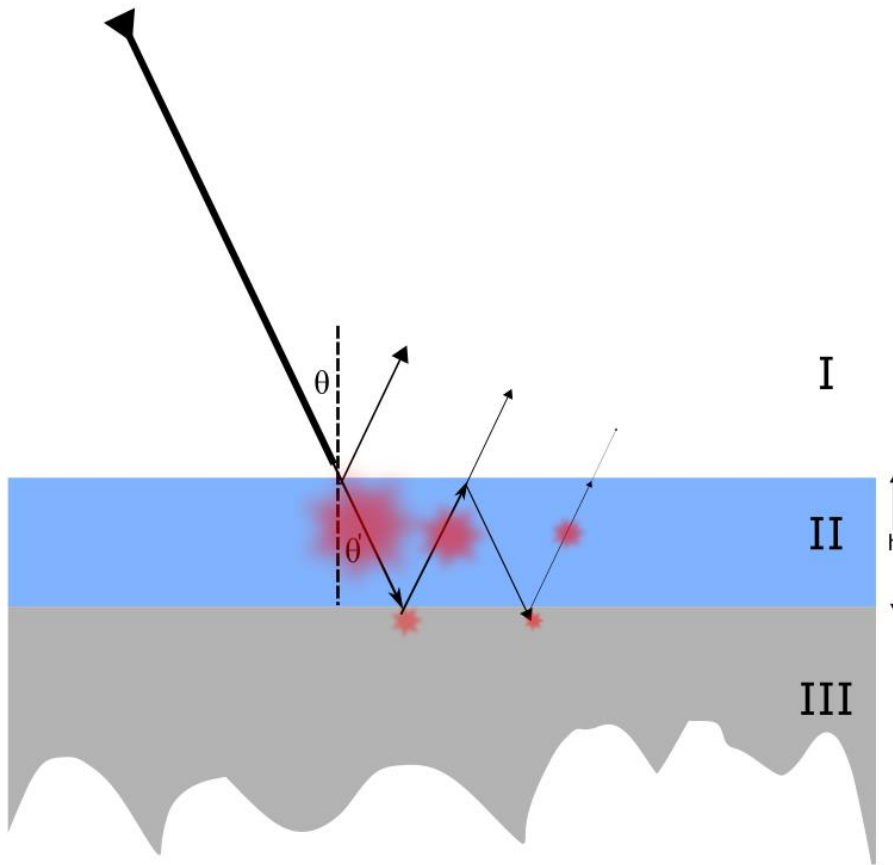


Figure 4| Lossy dielectric thin-film coating on a metal with finite conductivity. The strong losses in the dielectric allows, under the right conditions, for perfect cancellation of reflected light and the wave can be absorbed entirely inside the resonator.

In order to realize perfect light absorption in an optical coating, we need to reduce the intensity of light incident on the bottom metal film such that the reflection from the top dielectric film is equal to, and out of phase with, the reflected beams from the bottom metal film. A dielectric with strong absorption can attenuate light reflected off of the bottom metal film and allows for complete destructive interference. Light will be mainly absorbed inside the highly absorbing (lossy) dielectric. It has been shown recently that a thin-dielectric film that does not support any FP modes can absorb a maximum of 50% of the

incident light. This maximum occurs when $n \approx k \gg 0$, where n and k are the real and imaginary components of the complex dielectric refractive index n^* [11] Kats *et. al.* realized perfect light absorption in optical coatings using lossy dielectrics with simultaneously high n and k . The high value of n^* creates strong impedance mismatch with the incident light beam which increases the reflection intensity from the air-dielectric layer. Due to the strong absorption inside the dielectric layer, the reflected light from the bottom metal is of lower intensity and thus it is possible to create complete destructive interference and light is completely absorbed. For a metal behaving as a PEC and normal incidence the acquired phase is given by $\delta = \frac{4\pi}{\lambda_0} n' h$, which is equal to $m\pi$ when h is a multiple of $\lambda_0/4 n'$. Using a metal with finite conductivity, the non-trivial phase gained from the metal reflection ϕ allows for destructive interference for $h < \lambda_0/4 n'$.

4. References:

- [1] C. Oleari, Color in optical coatings, Optical Thin Films and Coatings, Pages 391–424, 425e (Woodhead Publishing Series in Electronic and Optical Materials, 2013).
- [2] J. Gao, *et. al.* “ Experimental realization of epsilon-near-zero metamaterial slabs with metal-dielectric multilayers,” Applied Physics Letters, 103, 5, 2013.
- [3] Ting Xu, Amit Agrawal, Maxim Abashin, Kenneth J. Chau & Henri J. Lezec , All-angle negative refraction and active flat lensing of ultraviolet light, Nature 497, 470–474 (23 May 2013).
- [4] K. V. Sreekanth, *et. al.*,” Extreme sensitivity biosensing platform based on hyperbolic metamaterials,” Nature Materials 15, 621–627 (2016).
- [5] Born, M & Wolf, E Principles of Optics 7th edn, Cambridge Univ. Press, 2003.
- [6] E. Hecht, Optics, 2nd edn., Addison-Wesley publishing, 1987.

-
- [7] J. H. Simmons, K. S. Potter, *Optical Materials*, Academic Press, 2000.
- [8] Z. Li, E. Palacios, S. Butun, H. Kocer , K. Aydin, "Omnidirectional, broadband light absorption using large-area, ultrathin lossy metallic film coatings," *Sci. Rep.* 5, 15137, 2015.
- [9] Z. Li, S. Butun, K. Aydin, "Large-Area, Lithography-Free Super Absorbers and Color Filters at Visible Frequencies Using Ultrathin Metallic Films," *ACS Phot.* 2, 2, 183-188, 2015.
- [10] M. A. Kats, R. Blanchard, P. Genevet , F. Capasso, "Nanometer optical coatings based on strong interference effects in highly absorbing media," *Nat. Mat.* 12, 20-24 , 2013.
- [11] C. Hägglund, S. P. Apell, B. Kasemo, "Maximized Optical Absorption in Ultrathin Films and Its Application to Plasmon-Based Two-Dimensional Photovoltaics," *Nano Lett.*, 2010, 10 (8), pp 3135–3141, 2010.

Iridescence Free and Narrow Band Perfect Light Absorption in Critically Coupled Metal-High Index Dielectric Cavities

Perfect light absorption in the Visible and near Infrared (NIR) has been demonstrated using a variety of systems, including metamaterials, plasmonic nanostructures, and thin film absorbers. Thin film absorbers offer a simple and low cost design for perfect light absorption as they can be produced on large areas and without lithography. Light is strongly absorbed in a thin film metal-dielectric-metal (MDM) cavity at given resonance frequencies and the absorption bandwidth can be tuned by adjusting the top metal layer thickness. However, a major drawback of MDM absorbers is their strong resonance iridescence, i.e., angle dependence.⁴ Here, we report a novel structure where we solve the iridescence problem by achieving angle insensitive narrowband perfect and near-perfect light absorption. In particular, we show analytically that using a high index dielectric in the MDM cavity is sufficient to achieve angle insensitive cavity resonance. We demonstrate experimentally angle insensitive perfect and near perfect absorbers in the NIR and visible regimes up to ± 60 degrees. By overcoming the iridescence obstacle of MDM absorbers we open the door for practical applications of perfect absorbers at optical frequencies (VIS – NIR).

1. Introduction to thin film cavity absorbers

Structural light absorption offers a broad range of possible applications in photonic and optoelectronic devices. In terms of spectral range, light absorbers can be classified as broadband or narrowband absorbers. Broadband light absorbers are useful for applications that rely on efficient light-to-heat generation such as thermo-photovoltaics,

thermal emission, and thermal imaging.¹ Narrowband light absorbers are promising candidates for sensing, optoelectronic devices, narrowband selective thermal emission and structural coloring which can replace traditional colorant pigmentation used in display technologies.² Many approaches to achieve structural light absorption require intensive lithography and nanofabrication (see ref [8] and references therein). For more practical applications, a large area, lithographically free structural absorber is highly desired. To that end, several works demonstrated broadband absorption using double layer lossy-dielectric/metal films³ and broad and narrowband absorption using metal-dielectric-metal (MDM) triple layer films.^{1,4} The MDM film acts as a subwavelength Fabry-Perot (FP) cavity that resonates with incident light at a given wavelength and angle. While the \mathbf{E} field is highly confined inside the dielectric layer due to constructive interference between the incoming and reflected waves, the power is mostly dissipated inside the metallic films.⁴

Broadband absorbers are largely insensitive to the incident angle due to their broadband nature which results in a slight change in the absorption intensity at a given wavelength as a function of angle.¹ Furthermore, broadband absorption in double layer lossy dielectric/metal films is angle insensitive due to the ultrathin nature of the dielectric layer which decreases the angle dependent phase that partially reflected waves accumulate as they propagate through the thin film.¹¹ On the contrary, for narrowband absorbers the angle dependence is significant and can be detrimental for practical applications especially for structural coloring as their color would change significantly.⁴

Omnidirectional absorption in MDM cavities was previously proposed, but the proposed system can only operate for a specific cavity thickness and at the surface plasmon frequency of the metal-dielectric interface.⁵ Furthermore, the absorption intensity is

reduced drastically for larger angles, which would result in effective color angle dependence. In addition, light absorbers based on ultrathin lossy dielectric/metal films cannot produce narrowband absorption due to the high losses in the dielectric film.³ Depositing an additional metal layer on top of the lossy dielectric can narrow the resonance due to the added interference from the metallic superstrate. However, this is only possible by lowering the losses of the system, e.g., using Silicon instead of Germanium, and/or the metal used, e.g., using silver instead of gold. Accordingly, such structures are constrained to materials exhibiting strong losses within a given wavelength range, which offers a possible but limited solution.⁶ Moreover, even after optimizing these structures, the absorption band is of low quality factor ($Q = \lambda/\Delta\lambda$) ≤ 8 and it does not exhibit perfect absorption because the system is not sufficiently lossy.

In order to realize perfect light absorption, light should be critically coupled to the cavity. In thin film absorbers, critical coupling takes place when the absorption rate equals the reflection rate. For an FP cavity, reflection is suppressed due to destructive interference, and losses are incurred due to losses in the metallic mirrors upon multiple reflections inside the cavity. By optimizing the thickness of the top metal, it is possible to control the finesse and broadness of such critical coupling.⁴

In this work, we analytically, numerically and experimentally demonstrate wide-angle range and narrowband perfect absorption in the NIR and visible regimes in an MDM structure. We show that choosing a dielectric with high refractive index allows for a wider acceptance angle range yielding a color preserving structure. It is worth noting that using high index dielectrics to attenuate iridescence in cavity absorbers was numerically predicted in [7] and conjectured in [9].

1- Theoretical background:

To rationalize the design of our system, we first carried out a theoretical analysis of incident angle sensitivity for the reflectance minimum in an MDM thin film structure. The system consists of a top metal layer of thickness t_m , a middle dielectric layer of thickness of t_d , and a bottom metal layer whose thickness is sufficiently large (\gg the skin depth) that it can be considered a semi-infinite substrate. The metal layers have identical composition, with refractive index n_m and extinction coefficient k_m , while the dielectric is described by refractive index n_d (the extinction coefficient of the dielectric is assumed negligible in the spectral range of interest). All these quantities are functions of the incident wavelength λ .

For a particular choice of refractive indices and layer thicknesses (see Methods for details on the optical functions used for Ag, Ge, MMA, and their respective thicknesses), we can use the standard transfer matrix approach to numerically solve for the reflectance $R(\theta, \lambda)$ as a function of λ and the incident angle θ . The numerical results for the wavelength $\lambda_{\min}(\theta)$ where R has a minimum in the NIR regime are plotted in **Figure 1(a)** as dots over a range of θ , for both p and s-polarized light. Two different system are illustrated, Ag-MMA-Ag and Ag-Ge-Ag to show the dramatic contrast between low-index ($n_{MMA} \sim 1.5$) and high-index ($n_{Ge} \sim 4.2$) dielectrics used for the middle layer. Clearly the Ag-MMA-Ag exhibits a much stronger variation in λ_{\min} with θ than Ag-Ge-Ag. This can be quantitatively seen in Figure 1(b), which plots $|\lambda_{\min}^{-1} d\lambda_{\min}/d\theta|$; the fractional change in λ_{\min} per shift in θ . This quantity is strongly suppressed in the Ge system relative to the MMA one.

To understand the origins of how n_d controls the angular sensitivity of λ_{\min} , we derive an approximate analytical equation whose solution is λ_{\min} . To do this, we note that $R(\theta, \lambda)$ in

the transfer matrix approach is the squared amplitude of a complex rational function, $R(\theta, \lambda) = |N_R(\theta, \lambda) + N_I(\theta, \lambda)/D_R(\theta, \lambda) + D_I(\theta, \lambda)|^2$, with N_R, N_I being the real/imaginary parts of the numerator, and analogously for the denominator terms D_R, D_I . When $\sec \theta \sim O(1)$, i.e. for smaller incident angles $\theta \lesssim 60^\circ$, the minimum in $R(\theta, \lambda)$ as a function of λ coincides with an excellent degree of approximation to the point at which $N_I(\theta, \lambda) = 0$. The latter equation has a much simpler analytical form than the condition for the minimum in R , and can be further simplified by assuming $k_m \gg n_m$ and $k_m \gg \sin \theta$, which are valid for Ag in the NIR wavelength range (1300-1800 nm) we are exploring. The end result is an analytical transcendental equation, whose solution for λ at a given θ gives $\lambda_{\min}(\theta)$,

$$\left[\frac{k_m}{n_d} \left(\frac{\alpha_d}{n_d} \right)^{\pm 1} \sinh \left(\frac{2\pi k_m t_m}{\lambda} \right) - \frac{n_d}{k_m} \left(\frac{n_d}{\alpha_d} \right)^{\pm 1} \cosh \left(\frac{2\pi k_m t_m}{\lambda} \right) \right] \sin \frac{2\pi \alpha_d t_d}{\lambda} + e^{\frac{2\pi k_m t_m}{\lambda}} \cos \left(\frac{2\pi \alpha_d t_d}{\lambda} \right) = 0 \quad (33)$$

where $\alpha_d = \sqrt{n_d^2 - \sin^2 \theta}$. In the terms with the ± 1 power, the +1 choice corresponds to p-polarization, while the -1 choice to s-polarization. In the perfect conductor limit, $k_m \rightarrow \infty$, this equation reduces to the conventional relation defining the modes of a dielectric sandwiched between perfectly conducting plates, $\sin(2\pi \alpha_d t_d / \lambda) = 0$, which is the same for p and s. Equation 1 can be seen as a generalization of this mode equation, accounting for the finite values of k_m and t_m , which lead to different mode locations for the two polarizations. The solution $\lambda_{\min}(\theta)$ calculated numerically from Equation 1 is drawn as a solid line in Figure 1(a), with the corresponding fractional change per angle in Figure 1(b). The results have close agreement with the exact transfer matrix approach up to $\theta \approx 60^\circ$, where the $\sec(\theta) \sim O(1)$ assumption underlying the theory begins to break down. Despite

this limitation, the theory provides an accurate representation of most of the angular range covered in our experiments, as we will show later.

Note that α_d is the only term in Equation 1 that depends directly on the incident angle θ . Though the transcendental equation cannot be solved analytically for $\lambda_{\min}(\theta)$, its structure tells us an important fact. We can use Equation 1 to derive an implicit differential equation for $\lambda_{\min}(\theta)$:

$$\frac{1}{\lambda_{\min}(\theta)} \frac{d\lambda_{\min}(\theta)}{d\theta} = H(\lambda_{\min}(\theta), \alpha_d(\theta)) \frac{1}{\alpha_d(\theta)} \frac{d\alpha_d(\theta)}{d\theta} \quad (34)$$

Here H is a complicated dimensionless function involving the system parameters, but which only depends on θ through $\lambda_{\min}(\theta)$ and $\alpha_d(\theta)$. It is of order $\sim O(1)$ in our spectral and angular range. Thus, the main contributions to setting the magnitude of the fractional change in $\lambda_{\min}(\theta)$ are the terms at the end:

$$\frac{1}{\alpha_d(\theta)} \frac{d\alpha_d(\theta)}{d\theta} = \frac{\cos \theta \sin(\theta)}{n_d^2 - \sin^2(\theta)} \quad (35)$$

As n_d increases to values $\gg 1$, the above expression decreases like $\sim n_d^{-2}$. This rapid decrease with the dielectric refractive index is why high index materials like Ge show such little fractional change in $\lambda_{\min}(\theta)$. We see the n_d^{-2} scaling directly in Figure 1(c), which plots $|\lambda_{\min}^{-1} d\lambda_{\min}/d\theta|$ versus n_d for an Ag-dielectric-Ag system at $\theta = 20^\circ$ using $\lambda_{\min}(\theta)$ solved from Equation 1. For simplicity, n_d here is assumed independent of wavelength. Both p and s polarizations show the same scaling behavior, since they differ only in the form of H .

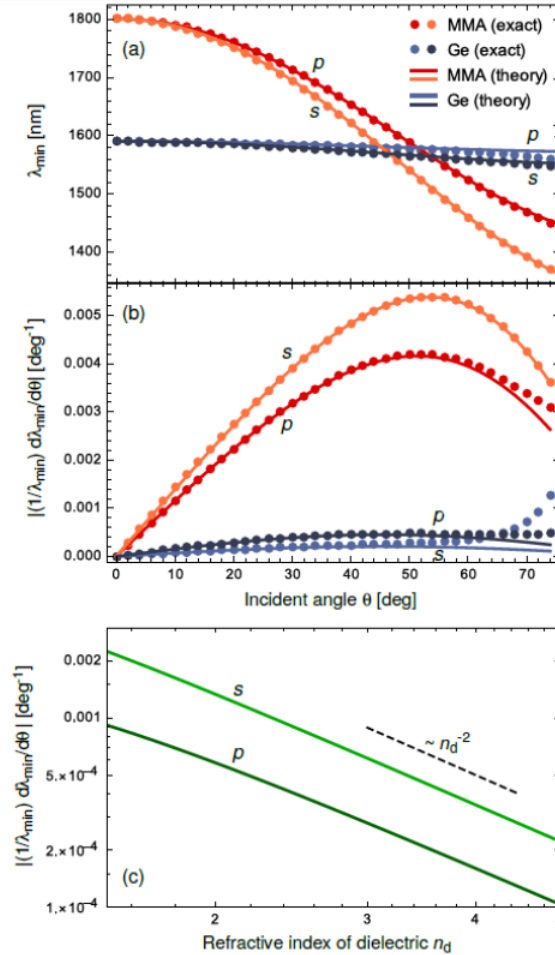


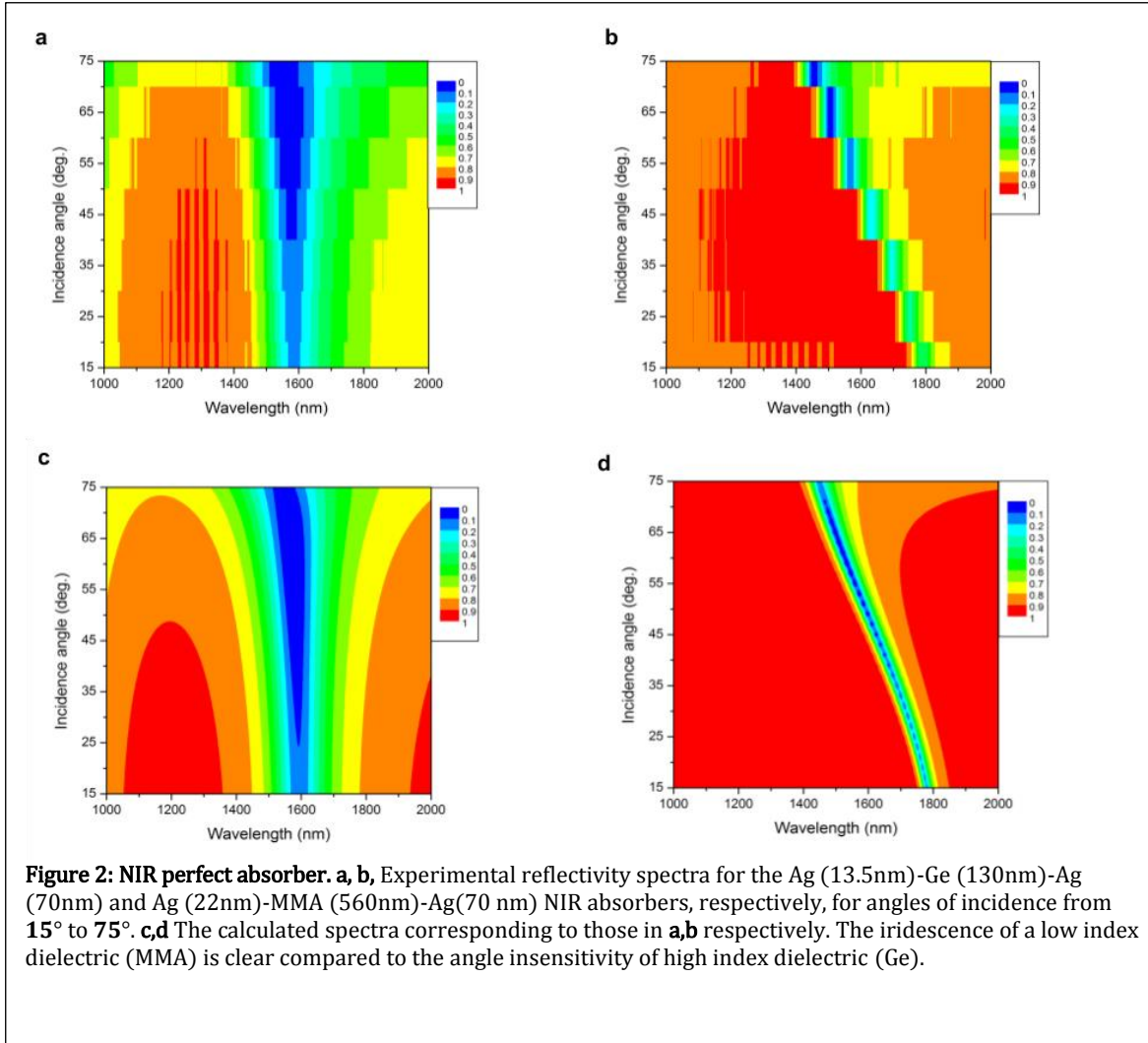
Figure 1 | (a) Wavelength $\lambda_{\min}(\theta)$ at which reflectance is minimized in the NIR region, as a function of incident angle θ for p and s polarized light. Dots correspond to the solution of the exact transfer matrix approach, while solid lines correspond to the solution of the approximate theory, Eq. (1). Two systems are compared: Ag-MMA-Ag (red/orange) and Ag-Ge-Ag (blue/dark blue), with thicknesses and optical constants described in the *Methods*. (b) The fractional shift in wavelength per angle, $|\lambda_{\min}^{-1} d\lambda_{\min}/d\theta|$ versus θ for the same systems as in panel (a). (c) The fractional shift per angle versus n_d for an Ag-dielectric-Ag system at $\theta = 20^\circ$, assuming a wavelength independent n_d . The results are calculated using Eq. (1). The t_m and t_d thicknesses here are taken to be the same values as for the Ag-Ge-Ag system in panel (a).

3-Experimental and discussion:

NIR perfect light absorber: For the design of the NIR perfect absorber, we used an Ag (13.5 nm)-Ge(130nm)-Ag(70nm) cavity. Using a highly reflective metal is essential for

narrowband absorption. Individual thin film thicknesses and refractive indices are obtained via spectroscopic ellipsometry (see *Method*). Absorption is considered complimentary to reflection in this system since scattering in thin films is negligible and the measured transmission is negligible (see supporting information). Note that transmission is suppressed in the NIR even for a relatively thin Ag bottom layer since Ag behaves as a nearly perfect electric conductor in the NIR. In order to realize perfect light absorption our calculations indicated that the Ag top layer should be in the order of 10 nm. Having a very thin Ag film (< 20 nm) can be problematic as thin Ag films tend to be irregular and form islands. This is another advantage for using Ge as a dielectric for the NIR absorber. Very thin Ag films deposited on top of Ge are homogenous and avoid clustering which further increases light absorption due to reduced surface roughness light scattering.¹⁰ For **p** polarized light, we achieved perfect light absorption ($\approx 99.8\%$) at 1576 nm close to the telecommunication wavelength, with Q factor of 8 for 65° incidence angle. Fig. 2(a) shows the reflectivity spectrum for the Ag-Ge-Ag cavity from $15^\circ - 75^\circ$. The absorption minimum remains almost unmodified as a function of the incident angle while the absorption intensity slightly decreases at smaller angles. For comparison, we fabricated an MDM cavity with low n_d dielectric (MMA). Fig. 2(b) shows the reflectivity spectrum for an Ag (22nm) - MMA (560nm) - Ag (70nm) cavity. The first order mode ($m=1$) of such cavity coincides spectrally with the Ag-Ge-Ag cavity mode at $\approx 45^\circ$. We observe considerable spectral shift in the MMA cavity mode for small angular changes. Furthermore, the reflection minimum for the MMA cavity shifts by ≈ 280 nm for the given angle range compared to only ≈ 48 nm shift for the Ge cavity, and this is also corroborated by the excellent agreement between the experimental and calculated reflectivity data

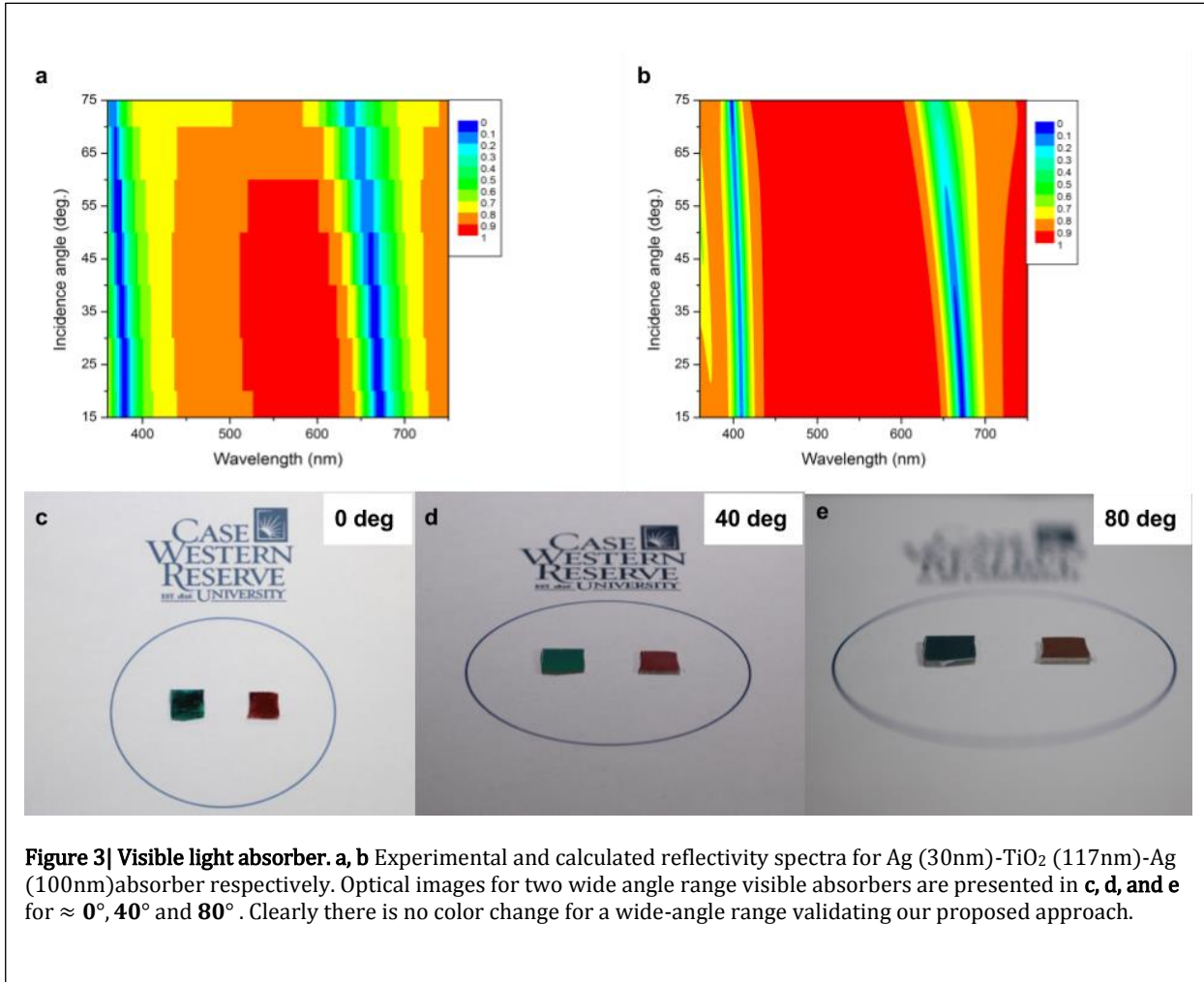
(Figure 2(c) and (d)). The absorption mode of Ag-MMA-Ag cavity is, however, narrower than that of the Ag-Ge-Ag cavity. This is due to the persistence of non-zero losses for Ge in the NIR which is translated to line broadening of the cavity resonance.



Visible near-perfect light absorber: Using Germanium as a narrowband absorber in the visible is not possible because it is highly absorbing due to direct electronic transitions that appear at high photon energies.³ Accordingly, we used Titanium dioxide (TiO₂) which has relatively high n' in the visible ($n' \approx 2.2$) and low losses. We fabricated an Ag(30nm)-

TiO₂(117nm)-Ag(100nm). The measured and calculated reflectance spectrum for **p** polarized light in the visible range from 360 to 750 nm and 15 -75 degrees is shown in Figure 3 (a) and (b) respectively. For the given cavity thickness we obtained two near perfect absorption modes ($m = 1$ and 2) reaching $\sim 94\%$ and 96% absorption and Q factors of ≈ 20 and ≈ 19 respectively for 15° incidence angle. Clearly, the modes are highly insensitive to the angle of incidence (see Fig. 3). The shifts in the reflectance minima for $m = 1$ and 2 modes are $\approx 33\text{ nm}$ and 18 nm respectively.

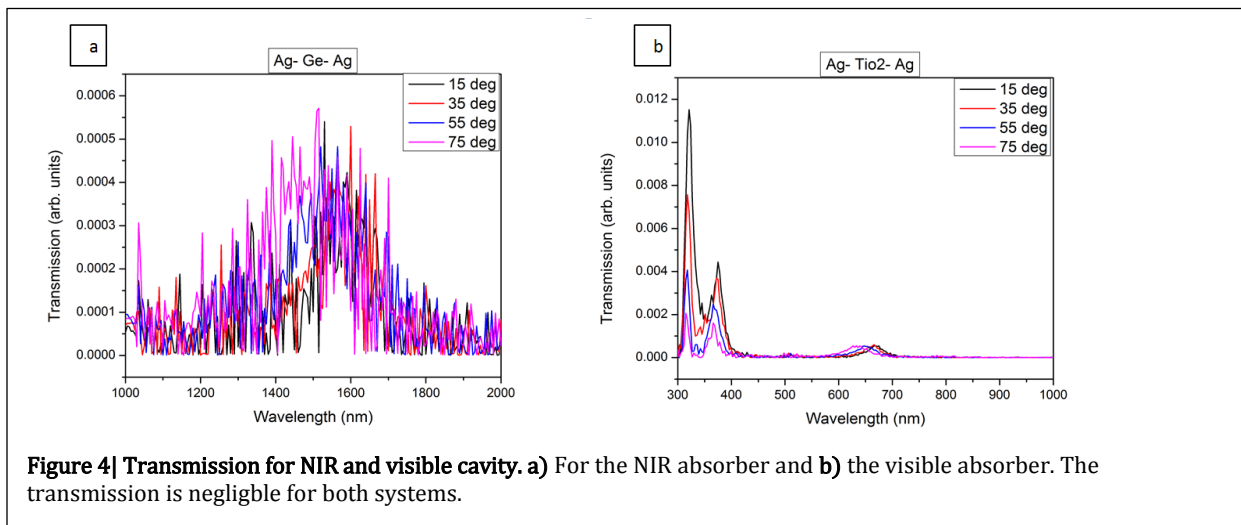
For applications related to structural coloring, it is important to minimize iridescence for unpolarized light. In our cavities, the angle insensitivity persists even for s polarization (see supporting information). Thus, we have achieved angle insensitive colors for unpolarized light, representing a relevant technological advantage for many optical applications. To demonstrate the validity of our approach, optical images (Figure 3 (c), (d), and (e)) were taken for two different Ag-TiO₂-Ag films at three angles showing no color change. For comparison, optical images for low n_d dielectric cavity (SiO₂) are presented in the supporting information of ref [4] showing different colors at different angles of incidence.



Transmission for NIR and visible MDM cavities:

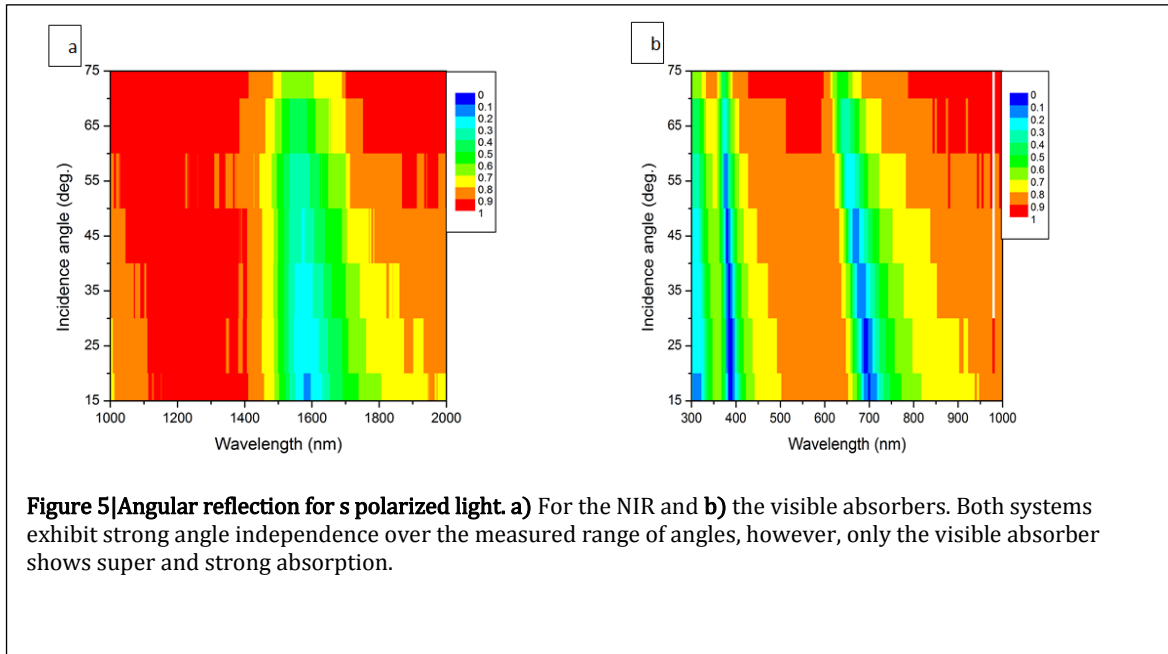
In order to verify that $A = 1-R$, the angular transmission was measured using variable-angle high-resolution spectroscopic ellipsometry (J. A. Woollam, V-VASE). The transmission for P polarized light for both the NIR and the visible cavities is shown in Figure 4, a and b respectively. It is clear that the transmission is negligible for both cases.

This also confirms our claim that in the NIR region using very thick bottom Ag mirror (>100nm) is not necessary.



Angle independence of S polarized light reflection:

We performed reflection measurements for the NIR and visible cavities using s polarized light. Still the modes did not shift considerably as a function of angle (Figure 5). These cavities were not optimized to achieve perfect or super light absorption with s polarized light.



In summary, we demonstrated angle insensitive narrowband perfect and near-perfect light absorption in the NIR and visible using FP cavities with high index dielectrics. Our work provides a practical solution to a major drawback of ultrathin film narrowband absorbers. Here, we relied on critical coupling effects to design and fabricate MDM thin films, which are a simple and low cost design for perfect absorbers as they can be produced with large areas and are lithographically free. We demonstrated the angle insensitivity of such a cavity analytically and showed that the fractional change in r_{\min} of minimum reflection as a function of θ scales inversely with the square of the refractive index. In addition, we have fabricated and characterized iridescence free MDM materials exhibiting narrowband light absorption using an Ag-Ge-Ag cavity in the NIR, and an Ag-TiO₂-Ag cavity in the visible. Our system can be used directly in applications related to structural coloring and EM shielding and can act as a reference for designing angle insensitive light absorbers. In particular,

using a high index dielectric as an overlay on top of any given light absorber should significantly attenuate the absorber angle dependence.

4-Methods:

Samples fabrication:

We fabricated the NIR perfect absorber by depositing ~ 13 nm Ag with 0.3 A s^{-1} deposition rate on a glass slide (Micro slides, Corning), then 130 nm of Ge with 0.5 A s^{-1} deposition rate. Finally, ~ 70 nm Ag was deposited at 0.5 A s^{-1} . For the visible absorber we deposited first 10 nm Ti (0.3 A s^{-1}) to ensure adhesion of the Ag to the glass slide, then we deposited ~ 100 nm Ag (0.5 A s^{-1}), 117 nm TiO₂ (0.5 A s^{-1}) and finally ~ 30 nm Ag (0.3 A s^{-1}) was deposited. For the Ag-MMA-Ag sample, methyl methacrylate (MMA) resist (8.5MMAEL 11, MICROCHEM) was spin-coated on 70 nm Ag film at 4,000 r.p.m., then we deposited ~ 22 nm Ag (0.3 A s^{-1}). We use lower deposition rate for the top Ag layers to decrease clustering and surface inhomogeneity. All Ag films were deposited using thermal evaporation. Ge and TiO₂ were deposited using electron beam evaporation. All materials were purchased from Kurt J. Lesker Company.

Optical characterization:

Variable-angle high-resolution spectroscopic ellipsometry (J. A. Woollam, V-VASE) was used to determine the thicknesses and optical constants of all thin films. The reflectivity spectra as a function of excitation wavelengths and angles were acquired using the same instrument, with wavelength spectroscopic resolutions of 1 nm.

Numerical simulations

The numerical results for the exact position of the reflectance minimum (Figure 1) and full reflectance spectra (Figure 2 c and d, and Figure 3 b) were obtained by using the transfer

matrix method (TMM)¹⁸. In order to find material thickness and dielectric parameters that fit the experimental data (Figure 2 c, d and Figure 3 b) in the measured wavelength and angle ranges, we employed a variety of dielectric models: for MMA and Ge we used the Forouhi-Bloomer model [12, 13] with custom-fit parameters; for the top and bottom Ag layers we used the Drude model, with fitted parameters consistent with the range given in Yang et al. [14]. For Ti, we used the Brendel-Bormann model [15], with the parameter set determined in Rakic' et al. [16]. The thicknesses resulting from best fits are listed in the figure captions. In the theoretical background section, we considered the bottom Ag layer to be infinite. For the Ag-MMA-Ag cavity, the top Ag layer was 22 nm and the MMA was 560 nm. For the Ag-Ge-Ag cavity the top Ag layer was 13 nm and the Ge layer was 130 nm. Finally for the Ag-TiO₂ – Ag layer the top Ag layer was 30 nm and the TiO₂ was 117 nm.

Acknowledgments:

This work was done in collaboration with professor Michael Hinczewski group at CWRU. Funding for this work is from the Ohio Third Frontier Project Research Cluster on Surfaces in Advanced Materials (RC-SAM); Case Comprehensive Cancer Center, Case Western Reserve University.

This work is published in the following article: “M. ElKabbash, E. Ilker, T. Letsou, N. Hoffman, A. Yaney, M. Hinczewski, and G. Strangi, Iridescence-free and narrowband perfect light absorption in critically coupled metal high-index dielectric cavities, *Optics Letters*, 42, 18, 3598-3601 (2017)”

5-References

- 1- Z. Li, E. Palacios, S. Butun, H. Kocer , K. Aydin. *Sci. Rep.*, **2015**, 5, 15137.

-
- 2- Y.-K. R. Wu, A. E. Hollowell, C. Zhang , L. J. Guo. *Sci Rep.*, **2013**, 3, 1194.
 - 3- M. A. Kats, R. Blanchard, P. Genevet , F. Capasso. *Nat. Mat.*, **2013**, 12, 20–24.
 - 4- Z. Li, S. Butun, K. Aydin. *ACS Phot.*, **2015**, 2 ,2, 183-188.
 - 5- H. Shin, M. F. Yanik , S. Fan. *App. Phys. Lett.*, **2004**, 84, 22.
 - 6- K.-T. Lee, S. Seo, J. Y. Lee, L. J. Guo. *Adv. Mat.*, 2014,26, 36 ,24, 6324–6328.
 - 7- J.-B. You, W.-J. Lee, D. Won, K. Yu. *Opt. Exp.* **2014**, 22, 7.
 - 8- C. M. Watts, X. Liu, W. J. Padilla, *Adv. Mater.*, **2012**, 24, OP98.
 - 9- D. Liu, H.T. Yu, Y.Y. Duan, Q. Li, Y.M. Xuan. *Sci. Rep.*, **2016**, 6 , 3251.
 - 10- V.J. Logeeswaran, N. P. Kobayashi, M. S. Islam, W. Wu, P. Chaturvedi, N. X. Fang, S. Y. Wang, R. S. Williams, *Nano Lett.* **2009**, 9 (1), 178-182.
 - 11- M. A. Kats, F. Capasso . *Laser Photon. Rev.*, **2016**, 10(5), 699-699.
 - 12- A.R. Forouhi, I. Bloomer. *Phys. Rev. B.* 34, 7018–7026 (**1986**).
 - 13- A.R. Forouhi, I. Bloomer. *Phys. Rev. B.* 38, 1865–1874 (**1988**).
 - 14- U. Y. Honghua, J. D'Archangel, M. L. Sundheimer, E. Tucker. *Phys. Rev. B* ,91, 235137, (**2015**).
 - 15- G. D. Boreman , M. B. Raschke. *Phys. Rev. B* 91, 235137, (**2015**).
 - 16- R. Brendel and D. Bormann. *J. Appl. Phys.* 71, 1-6 (**1992**).
 - 17- A. D. Rakic´ , A. B. Djuris´ ic´ , J. M. Elazar, M. L. Majewski. *Applied Optics* 37 (22), 5271-5283, (**1998**).
 - 18- F. L. Pedrotti, L. M. Pedrotti, L. S. Pedrotti, *Introduction to Optics*, 3rd edition, , Pearson education limited, **2006**.

Hydrogen sensing using thin-film cavity perfect light absorber

Hydrogen sensing is important in many industrial, biomedical, environmental and energy applications. Realizing a practical, reliable and cheap hydrogen sensor, however, is an ongoing challenge [1]. Here we demonstrate a hydrogen sensor based on optically active metal-dielectric-metal (MDM) cavity absorber. The sensor demonstrates high figure-of-merit and can sense low hydrogen concentrations. Although the sensor exhibit hysteresis, we did not observe any significant deformation that affects the sensor optical properties. The large area and reusability of our sensor makes it an attractive and practical option especially for miniaturized hydrogen sensors necessary for medical and food safety applications.

1- Introduction to nano-photonic hydrogen sensing:

At ambient pressure and temperature hydrogen is colorless, tasteless and highly flammable [2]. Hydrogen is flammable at concentrations ranging from 4% -75% with low ignition energy [3]. Accordingly, hydrogen sensing is largely used in industries where it is a necessary component or a byproduct to monitor and control the hydrogen partial pressure for safety purposes. Hydrogen is also produced by certain bacteria and hydrogen sensors are used in food industry and have possible medical applications [2, 4, 5]. While gas chromatography and mass spectrometry systems can be used in large scale industrial sensing, other applications require miniaturized sensors. Several nano-photonic and plasmonic systems were proposed as platform for optical hydrogen sensing [6, 7]. Photonic and plasmonic materials enable subwavelength control and manipulation of light and exhibit unique functionalities [8]. Metals that form metal hydrides, e.g. Palladium (Pd),

upon exposure to hydrogen are excellent candidates for miniaturized hydrogen sensors. When Pd is exposed to hydrogen it forms palladium hydride (PdH_x) with certain hydrogen atomic ratio x . PdH_x exists in two solid state phases (α and β) depending on the temperature, pressure, and hydrogen partial pressure in its environment. At low hydrogen partial pressure, intercalated hydrogen atoms are randomly situated inside the Pd lattice and the hydrogen forms a solid solution (α phase) [9]. At higher hydrogen partial pressure, hydrogen-hydrogen interactions result in a more ordered structure forming a hydride β phase [3]. In the β phase, the lattice parameter increase by $\sim 3.5\%$ as the lattice expands to accommodate the hydrogen atoms occupying new lattice sites [9]. For intermediate hydrogen partial pressures, both α and β phases coexist in a Pd film (so called α' phase) [10]. In α' and β phases, Pd experiences significant hysteresis between the formation and decomposition of the hydride phase. This hysteresis is because of the energy barrier between the hydride and metal phases due to lattice strains which does not exist in the α phase [3, 11]. The change in the complex permittivity and lattice structure of Pd results in a measurable optical response from a photonic [12] or a plasmonic [6, 8] system.

While sensors based on metal hydrides are highly selective compared to other materials [13], these sensors are lithographically intense [6,8]. Realizing large area and lithography free hydrogen sensor can overcome nanofabrication problems, e.g. high costs, low throughput and fabrication imperfection. In this work, we use thin film cavity perfect light absorbers as large-area and lithographically free hydrogen sensors. The fabrication simplicity, selectivity, and large throughput of our sensor make it a promising candidate for practical hydrogen sensing applications.

Hydrogen sensing based on perfect light absorption was introduced in [8] where the authors used palladium nano-wires as a grating on top of a multilayer system. In such system, reflection is reduced via impedance matching in order to achieve perfect light absorption with absorbance $A \approx 99.5\%$. Changes in the optical properties in the palladium nanowire resulted in a shift in the absorption maximum $\Delta\lambda_{max} \approx 19nm$, and a change in the measured relative intensity change of up to 500. Additionally, thin-film absorber hydrogen sensing was numerically investigated in [14].

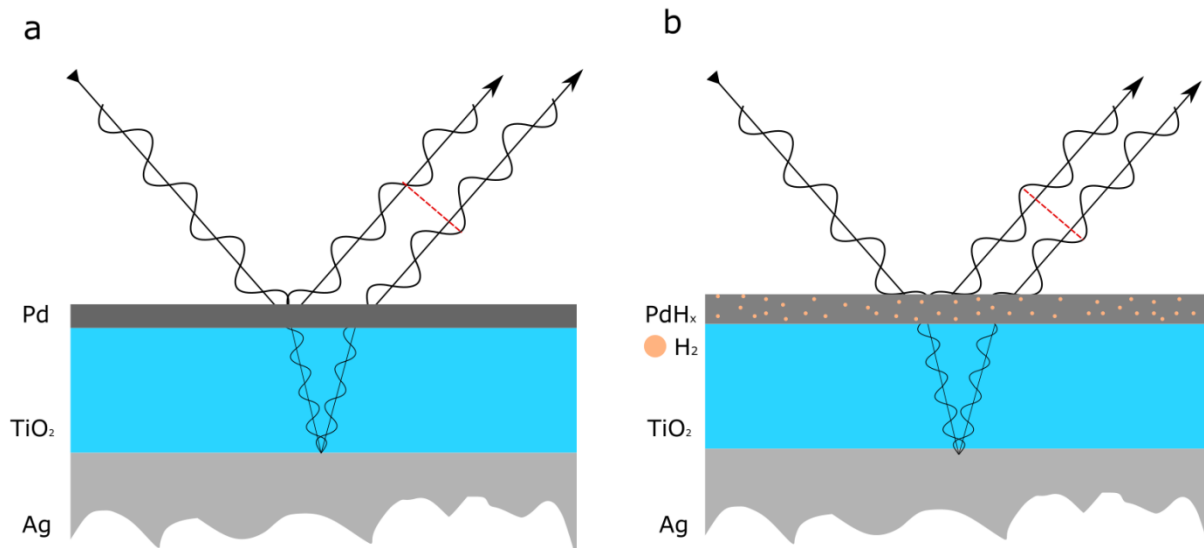


Figure 1 | Fabry-Perot cavity absorber sensor: a) A light absorber, metal (Pd)-dielectric (TiO_2)-metal (Ag) cavity. The reflection decrease due to destructive interference **b)** Exposing the absorber to hydrogen convert the Pd layer to a hydride PdH_x with a given hydrogen atomic ratio (x). The cavity can be designed such that formation of the hydride results in total destructive interference and perfect light absorption.

2- Thin film absorber sensor design:

The sensor consists of a $\lambda/4$ nm Pd- $\lambda/4$ nm TiO_2 - $\lambda/4$ nm Ag MDM cavity (Fig. 1a). In a thin-film metal-dielectric-metal (MDM) cavity, since scattering is negligible, the sum of the absorbance A , transmittance T and reflectance R is given by $A + T + R = 1$. The goal of a thin-film optical perfect absorber is to eliminate both T and R . Using an opaque, thick metal film as a bottom layer eliminates T while realizing total destructive interference eliminates R . Given that interference in thin-films is an amplitude splitting interference [15], perfect

light absorption is possible if light reflected from the top layer is cancelled out by the subsequent reflected partial waves by the bottom metal layer.

At resonance, the cavity absorption is maximized due to destructive interference [16]. The cavity resonance takes place when the phase difference between two successive reflected

beams $\delta = \frac{4\pi}{\lambda_0} n' h \cos \theta' + \phi^t + \phi^b = 2m\pi$, [17] where λ_0 and θ' are the incidence

wavelength and angle respectively, n' and h are the refractive index and thickness of the dielectric forming the cavity respectively, ϕ^t and ϕ^b are the phase acquired upon reflecting from the top and bottom metal layers respectively and m is the resonance order and is an odd number. Note that the acquired phase shift from a metal with finite conductivity is non-trivial ($\neq 0$ or π) and depends on the metal complex permittivity. As shown schematically in Fig. 1, transforming Pd to PdH_x changes ϕ^t and thus results in a shift in the resonant mode. Starting with a cavity that exhibits near-perfect light absorption, it is possible to choose an angle such that as Pd converts to PdH_x the absorption intensity increases by approaching an exact π phase difference between the partially reflected waves as shown in Fig. 1a, and 1b.

3-Experimental:

The setup and sensor schematics and the sensor image are shown in Fig. 2a and 2b respectively. In order to expose the sensor to different hydrogen concentrations, we attach a microfluidic channel on the sensor with tubing connected to a tank of nitrogen mixed with hydrogen with 4% concentration and another with pure nitrogen. Each gas source is regulated via an MFC which allows us to change the hydrogen concentration. The sensor is then placed on a variable angle ellipsometer (J. A. Wollam) to measure the reflectivity R as a function of angle. Introducing the channel affects the measured reflectivity as it splits the

incident beam into two reflected beams. We investigate the beam reflected from the sensor surface from which we are able to determine the reflection minimum of the cavity mode.

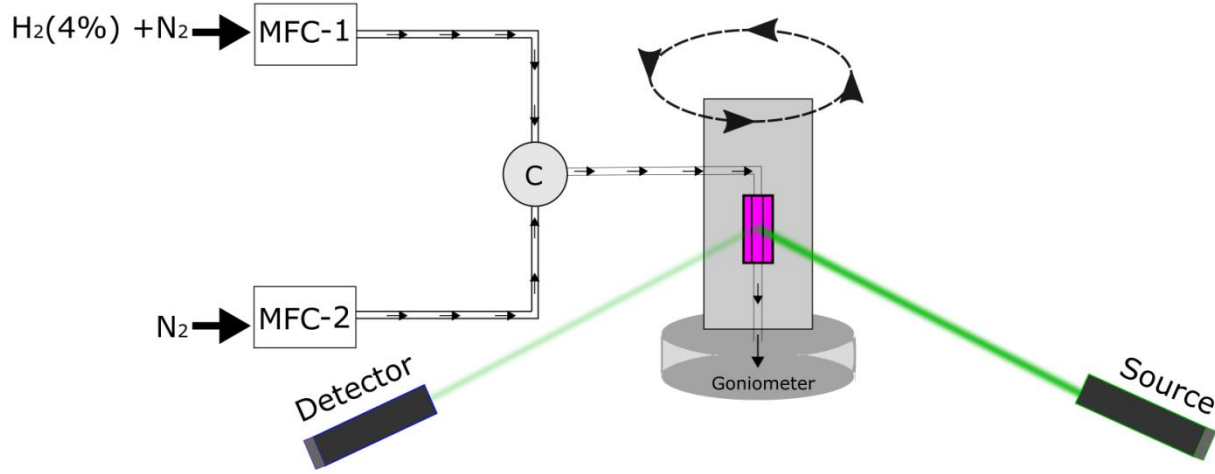


Figure 2 | Schematic of the sensing setup: A microfluidic channel is attached to the thin-film absorber and connected to two mass flow controllers (MFCs). One MFC controls the flow of nitrogen mixed with hydrogen (4% in concentration) and another MFC controls the flow of pure nitrogen. The sensor is then placed on a variable angle ellipsometer to measure the angular reflectivity.

We define a quantity that reflects the optical activity of our absorber $\eta = R_{N_2}/R_{H_2}^C$, where

R_{N_2} is the reflectivity of the sensor without hydrogen and $R_{H_2}^C$ is the reflectivity of the

sensor with hydrogen of concentration C . We design our experiments such that $R_{H_2}^C < R_{N_2}$,

and that $R_{H_2}^C$ decreases as we increase the hydrogen concentration. The sensitivity is then

defined as $\Delta\eta/\Delta C$. We are also interested in the total shift of the wavelength of minimum

reflectivity λ_{min} , where the sensitivity is defined as $\Delta\lambda_{min}/\Delta C$. Due to the channel effect on

the measured reflectivity, we calculate η by locating λ_{min} which, for a given C , corresponds

to a certain hydrogen atomic ratio x in the hydride PdH_x . Knowing the optical constants of

PdH_x allows us to obtain the *true* reflectivity of the cavity for a given C . The sensing results

for 0%, 0.7%, 2% and 4% H_2 exposure are shown in Fig. 3. The inset of Fig. 3a shows the

measured shift in $\Delta\lambda_{min}$ for the different concentrations. The sensitivity $\Delta\lambda_{min}/\Delta C$ is

15 ± 2 nm per 1% increase in the Hydrogen concentration.

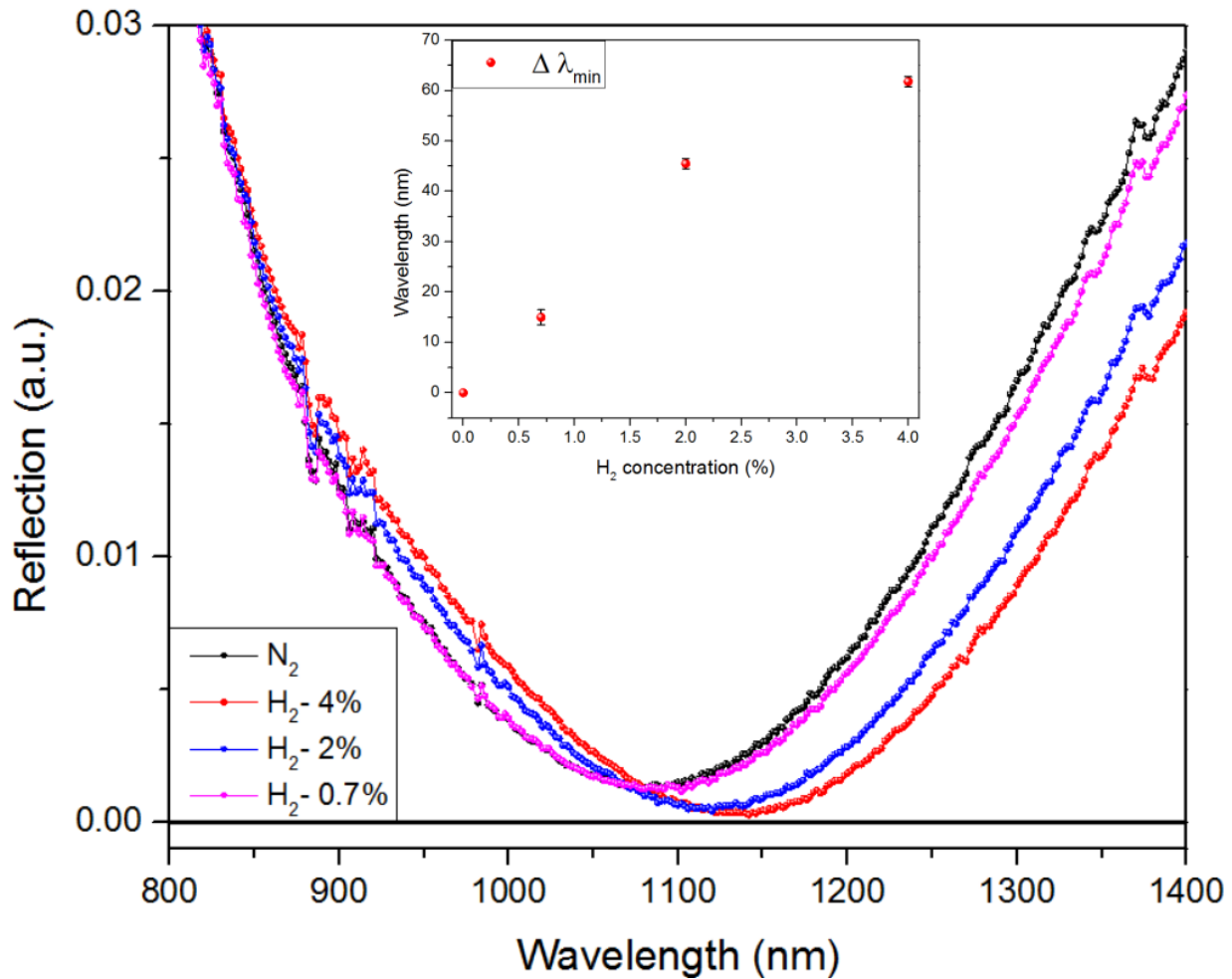


Figure 3 | Reflectance as a function of hydrogen concentration: The reflectivity of the cavity absorber as a function of hydrogen concentration. The absorption mode red-shifts and decrease in absorption. The inset shows the λ_{\min} as a function of concentration.

For hydrogen concentrations leading to the creation of α' or β phases, hysteresis in thin-film hydrogen sensors is always present. The hysteresis is due to the existence of a mechanical energy barrier due to the coherency strain produced by the lattice expansion in the hydride phase [11]. The energy barrier prevents releasing hydrogen atoms situated inside the hydride lattice. Figure 4 shows the sensor response of the cycled hydrogen response for hydrogen concentrations (0%, 0.7%, 2%, 3% and 4%). The existence of

coherency strain, however, did not affect the overall performance of our sensor as the cavity mode relaxed to its initial state.

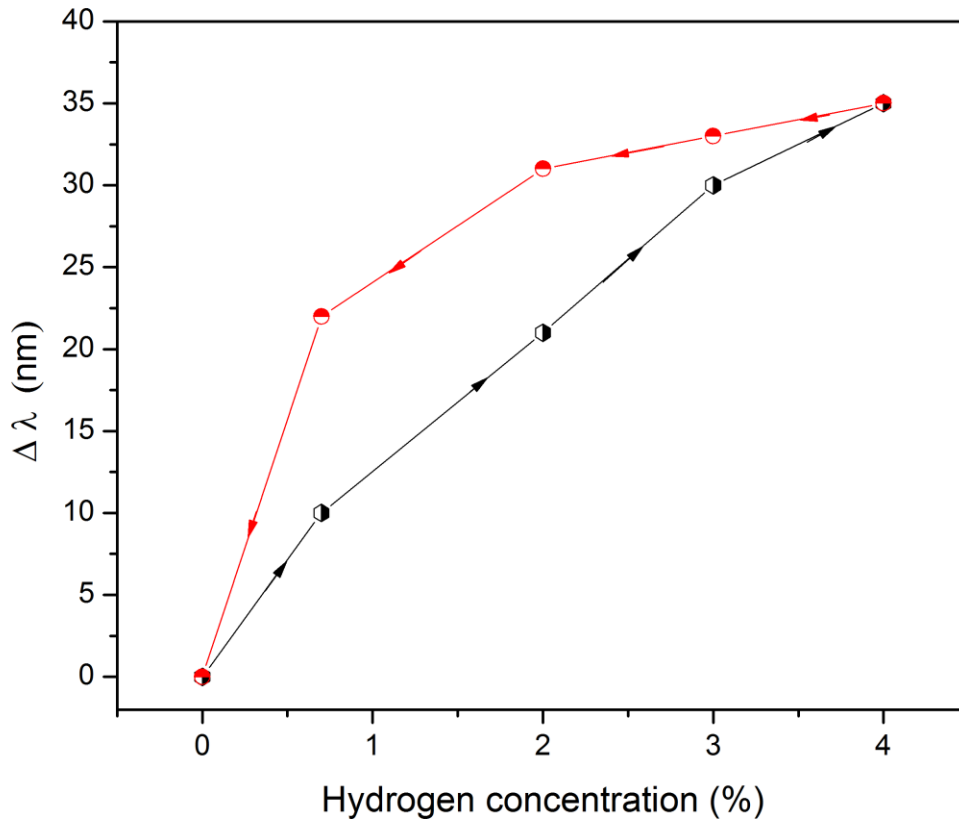


Figure 4| Hysteresis in the cavity absorber: Coherency strains affect the relaxation of the absorption cavity mode and result in hysteresis.

It is worth noting that the maximum shift in the hysteresis measurements at 4% hydrogen concentration is significantly lower than that measured earlier. This can either mean that the sensor itself deteriorated due to strains and cracks or that the hydrogen atomic ration in the formed hydride decreased. Given that the 0% case (nitrogen only) did not change in all experiments; we can safely assume that it is the latter. The reason why we would have different hydrogen atomic ratios is because the pressure inside the channel was not

controlled. The internal pressure depends on the flow rate as well as the tubing physical integrity which changed over time.

The proposed sensor's main advantage is the ease of fabrication and large area of exposure which can allow it to be used for large scale production. Indeed, in a more natural environment, the constraints imposed by the channel will not be present. Future works can utilize other metals that form hydride. The hysteresis problem can be overcome, or at least attenuated, by introducing a metal hydride alloys[18].

Acknowledgments:

This work was done in collaboration with professor Michael Hinczewski group, Professor Mohan Sankaran group, and Professor Umut Gurken group at CWRU. Funding for this work is from the Ohio Third Frontier Project Research Cluster on Surfaces in Advanced Materials (RC-SAM); Case Comprehensive Cancer Center, Case Western Reserve University.

4- References:

- [1] R. Pitts, P. Liu, S-H. Lee, E. Tracy, Interfacial Stability of Thin Film Hydrogen Sensors, proceedings of the 2001 DOE hydrogen program review, 2001.
- [2] S. Syrenova, C. Langhammer Plasmonic Hydrogen Sensing with Nanostructured Metal Hydrides Carl Wadell, ACS Nano,, 8 (12), pp 11925–11940, 2014.
- [3] N. R. Fong, P. Berinibc , R. N. Taita, Hydrogen sensing with Pd-coated long-range surface plasmon membrane waveguides, Nanoscale, 7, 2016.

-
- [4] J. R Wilkins, G. E. Stoner, E. H. Boykin, Microbial Detection Method Based on Sensing Molecular-Hydrogen. *Appl. Microbiol.* 27, 949–952, 1974.
- [5] C. H. S. Hitchcock, Determination of Hydrogen as a Marker in Irradiated Frozen Food. *J. Sci. Food Agric.* 80, 131–136, 2000.
- [6] N. Liu, M. L. Tang, M. Hentschel, H. Giessen, A. P. Alivisatos, Nanoantenna-enhanced gas sensing in a single tailored nanofocus, *Nature Materials* 10, 631–636, 2011.
- [7] X. Bévenot, A. Trouillet, C. Veillas, H. Gagnaire, M. Clément, Surface plasmon resonance hydrogen sensor using an optical fibre, *Meas. Sci. Technol.* 13, 118, 2002.
- [8] A. Tittl, P. Mai, R. Taubert, D. Dregely, N. Liu, H. Giessen, Palladium-Based Plasmonic Perfect Absorber in the Visible Wavelength Range and Its Application to Hydrogen Sensing, *Nano Lett.*, 11 (10), pp 4366–4369, 2011.
- [9] S. Syrenova, C. Wadell, F. A. A. Nugroho, T. A. Gschneidtner, Y. A. Fernandez, G. Nalin, D. Świtlik, F. Westerlund, T. J. Antosiewicz, V. P. Zhdanov, K. Moth-Poulsen, C. Langhammer, Hydride formation thermodynamics and hysteresis in individual Pd nanocrystals with different size and shape, *Nature Materials* 14, 1236–1244, 2015.
- [10] F.D. Manchester, A. San-Martin, J.M. Pitre, The H-Pd (Hydrogen-Palladium) System, *Journal of Phase Equilibria*, 15, 1, 1994.
- [11] Schwarz, R. B. & Khachaturyan, A. G. Thermodynamics of open two-phase systems with coherent interfaces: Application to metal–hydrogen systems. *Acta Mater.* 54, 313–323, 2006.
- [12] Y. Zhao ; Q.-l. Wu ; Y.-n. Zhang, High-Sensitive Hydrogen Sensor Based on Photonic Crystal Fiber Model Interferometer, 66, 8, 2017.

-
- [13] Peter Ngene, Tsveta Radeva, Martin Slaman, Ruud J. Westerwaal, Herman Schreuders, Bernard Dam Seeing Hydrogen in Colors: Low-Cost and Highly Sensitive Eye Readable Hydrogen Detectors, *advanced functional materials*, 24, 16, 23, 2374–2382, 2014.
- [14] M. Serahtlioglu, M. Erhatlioglu, S. Ayas, N. Biylikli, A. Dana, M. E. Solmaz, Perfectly absorbing ultra-thin interference coatings for hydrogen sensing, *Optics Letters*, 41, 8, 2016.
- [15] E. Hecht, *Optics*, 2nd edn., Addison-Wesley publishing, 1987.
- [16] M. ElKabbash, E. Ilker, T. Letsou, N. Hoffman, A. Yaney, M. Hinczewski, G. Strangi, Iridescence-free and narrowband perfect light absorption in critically coupled metal high-index dielectric cavities, *Optics letters*, 42, 18, 3598-3601, 2017.
- [17] Born, M & Wolf, E *Principles of Optics* 7th edn, Cambridge Univ. Press, 2003.
- [18] C.Wadell, F. Anggoro, A. Nugroho, E. Lidström, B. Iandolo, J. B. Wagner, C. Langhammer, Hysteresis-Free Nanoplasmonic Pd–Au Alloy Hydrogen Sensors, *Nano Lett.*, 15 (5), 3563–3570, 2015.

Nanometer Optical Coating Absorbers Using Loss-free Dielectrics and Low Conductivity Metals.

Optical absorbers that enable strong to perfect light absorption have many applications in thermo-photovoltaics, photo-detectors, stealth technologies, thermal emission, optical switches and structural coloring [1-5]. Using thin-film interference enabled lithographically free light absorbers that are large scale and simple to realize and tune [5]. The simplest design of a light absorber is an optical coating consisting of a nanometer thick, lossy dielectric on a metal with finite conductivity [6]. Although such system found many applications [7], it is limited to materials and spectral regions where the dielectric is strongly absorptive and the metal substrate is not behaving as a perfect electric conductor (PEC). Here we show that it is possible to achieve strong to perfect light absorption using loss-free dielectric on a metal with low conductivity. Using our approach, we demonstrate iridescent-free light absorption in the visible, NIR, and short wavelength IR (SWIR) regions. The simplicity and flexibility of our design makes the proposed absorber attractive for many applications specifically in structural coloring, selective thermal emission, bolometers, and sensing.

1- Introduction to optical coating absorbers

The existence of free electrons in metals results in both absorbing as well as reflecting incident light. Accordingly, it is not possible to achieve perfect light absorption using metals. The absorption due to a single reflection from a metal surface, however, depends on its conductivity σ ; free electrons in metals with high σ screen the electric field efficiently

and result in less absorptive losses. For metals, the complex refractive index $n(\omega)_m^*$ at a given frequency ω is given by $n(\omega)_m^* = n_m + i k_m$. If $k_m \gg n_m$ and $n_m \approx 1$, then σ is high (e.g., Ag, Al, Au, etc.), and if $k_m \approx n_m \gg 1$, σ is low (e.g., Pd, Ti, Ni, W, Cr, etc.). Similar consideration is given to dielectric films where it is possible to create strong light absorption due to, e.g., inter-band transitions. However, a dielectric with strong losses will naturally have a high refractive index and will exhibit strong impedance mismatch with light incident from air. The impedance mismatch will increase reflection and perfect light absorption is not possible. It is possible, however, to realize strong and perfect light absorption using metals only that has structural features which allows strong field localization and decreases the reflected and transmitted intensity utilizing, e.g., surface plasmon resonance [8] or free space impedance matching using metamaterials and metasurfaces [9].

For large scale, lithographically free optical absorbers, combination of dielectric and metal films is necessary. Since scattering is negligible in thin-films, the sum of the absorptivity A , transmissivity T and reflectivity R is given by $A + T + R = 1$. The goal of a thin-film optical perfect absorber is to eliminate both T and R . Using an opaque, thick metal film as a bottom layer eliminates T while realizing total destructive interference eliminates R . Given that interference in thin-films is an amplitude splitting interference [10], perfect light absorption is possible if light reflected from the top layer is cancelled out by the subsequent reflected partial waves by the bottom metal layer. Using an optical coating absorber, i.e., a dielectric thin-film on a metallic substrate is advantageous, compared to metal-dielectric-metal cavities. Firstly, destructive interference phase can accumulate for a dielectric film with thickness $t \leq \lambda / 4 n$ which is important when the total thickness of the

absorber affects its efficiency and cost, e.g., for IR absorption and thermal emitters [7]. In addition, dielectric films cannot be scratched easily which is advantageous for structural coloring and visual arts applications. Kats *et al.* demonstrated an optical coating absorber using a highly absorbing dielectric on a metal with finite, yet high, σ . Having a strongly absorbing dielectric film is very limiting as it requires a dielectric with a large complex refractive index $\mathbf{n}^* = \mathbf{n} + i\mathbf{k}$, such that $\mathbf{n} \approx \mathbf{k} \gg \mathbf{1}$ [11]. These conditions are usually satisfied in semiconductors at photon energies above their bandgap. However, most dielectrics are lossless. The current understanding is that without a strongly absorbing dielectric, an optical coating absorber is *not possible* and that such system would be the optical coating analogue of a Gires–Tournois etalon. [6].

In this work, we show that even with a loss-free dielectric coating, it is possible to realize strong to perfect light absorption by using a metal with low σ as a substrate. We highlight the flexibility of our approach by comparing the reflectivity of different thicknesses of titanium dioxide (TiO₂) thin-film on a high σ metal (Silver- Ag) and low conductivity metal (Nickel-Ni) and show that perfect light absorption in the visible and NIR is only possible using a low σ metal. Given that low conductivity metals do not behave as PEC in most of the IR region [12], we demonstrate perfect light absorption in the short wavelength IR region (SWIR) using germanium (Ge) optical coating with thickness $t < \lambda/4 n$ which is not possible using an Ag film substrate as Ag becomes a PEC for energies below the NIR region.

2-Results and Discussion:

Fig. 1a presents a schematic of a lossy-dielectric on a metal with high σ [OC1] compared to a lossless dielectric on a metal with low σ [OC2] (Fig. 1b). The amplitude of the first reflected beam is generally low since dielectrics weakly reflect light. However, total

destructive interference is possible only if the partial waves reflected from the bottom metal layer are attenuated due to losses in the dielectric (OC1) or in the metal (OC2). Using a commercially available finite element method package (COMSOL), we calculate the total power dissipation density for a normal incident plane wave with wavelength 650nm on OC1 using a lossy dielectric (Germanium-15 nm) on a high σ metal [Ag-100nm] (Fig. 1c), and compare it to the total power dissipation density in OC2 system using a lossless dielectric (TiO₂ – 40 nm) on a low σ metal [Ni-100nm] (Fig. 1d). The thicknesses were chosen to realize total destructive interference at 650nm. It is clear that most of the energy is dissipated in the dielectric (Fig. 1c) for OC1 and is entirely dissipated in the metal for OC2 (Fig. 1d). The strong loss-heat generation in the metal film allows our proposed system to work as a bolometer as we will detail later.

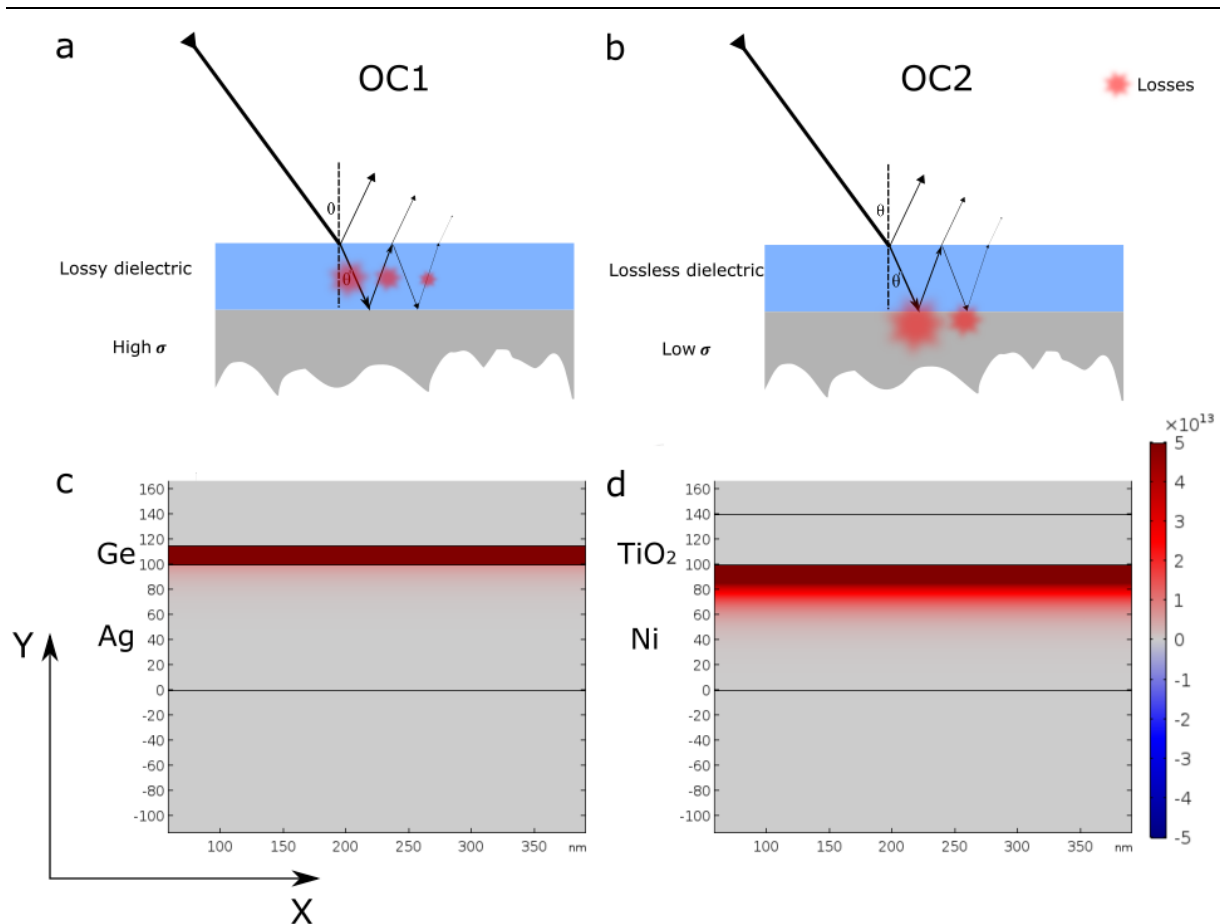


Figure 1 [Optical coating absorbers] based on a) lossy dielectric on a metal with high σ (OC1) where the absorption mainly takes place in the dielectric, and b) a lossless dielectric on low σ (OC2) where the absorption mainly takes place in the metal. In all cases, when the destructive interference condition is met, the reflected wave at the air-dielectric interface would have an equal magnitude to the sum of the partial waves reflected from the metal substrate. c) and d) show the calculated total power dissipated on OC1 and OC2 respectively. In OC1 the power is mainly dissipated inside the dielectric with some losses incurred in the metal, while in OC2 the power is entirely dissipated inside the metal.

We demonstrate our approach in the visible and NIR using a TiO₂ coating with different thicknesses deposited on either a 90 nm Ag film or a 90nm Ni film. Fig. 2 a, b, c, and d show the reflectivity for s-polarized light with incident angles 15° to 75° for TiO₂ with thickness $t = 20, 40, 60, \text{ and } 80 \text{ nm}$ for Ag substrate (left) and Ni substrate (right).

The strong absorption for the TiO₂-Ag optical coating is limited to wavelengths $< 500 \text{ nm}$ and its spectral location is independent of the dielectric thickness. This is because Ag conductivity is low $< 500 \text{ nm}$ and thus it is possible to realize strong light absorption even with a lossless dielectric. Using Ni as a substrate, however, allows for strong to perfect light

absorption that redshifts as we increase the TiO₂ thickness and spans the visible and NIR regions while maintaining a thickness $t \leq \lambda / 4 n$. The absorption reaches up to 99.8% and stays above 80% for all measured incident angles and for all TiO₂ thicknesses. Note that the absorption modes are iridescent free as the dielectric is of a relatively high refractive index (cite our work). Fig. 3a shows an optical image of Ni substrate coated with different thicknesses of TiO₂ (20 to 60 nm by 10nm). Fig. 3b shows Ni film deposited on a roughened glass surface (frosted microscope glass slide) and coated with two 55nm and 65nm thick TiO₂. The ability to maintain the color integrity even on a roughened surface is due to the iridescent free absorption property of our system.

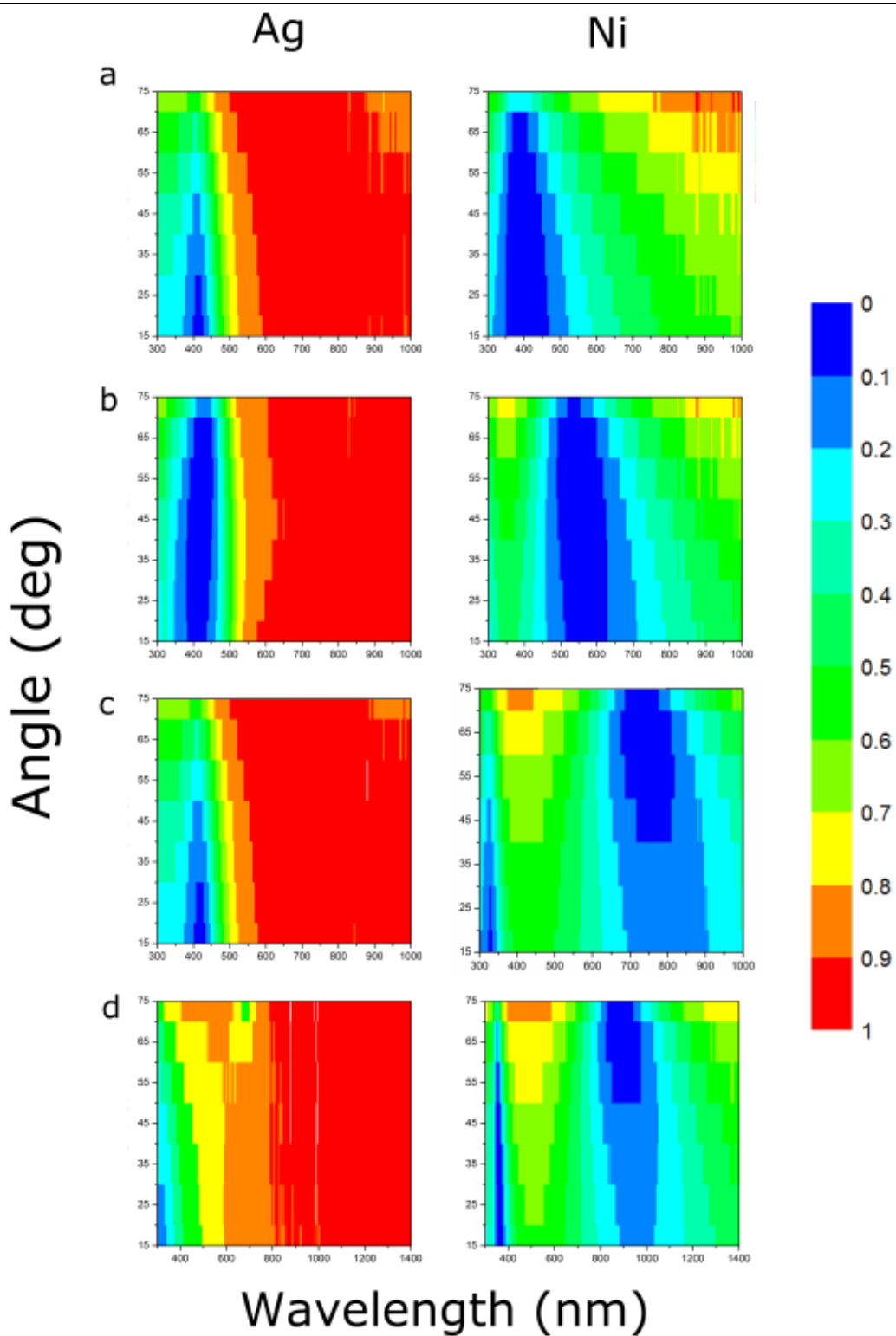


FIGURE 2|Reflectivity spectrum: Experimental Reflectivity spectra for S-polarized light for angles of incidence from 15° to 75° for an Ag film (left) and Ni film (right) coated with TiO₂ thickness A) 20nm, B) 40nm, C) 60nm and D) 80 nm.

One major difficulty using OC1 is that high conductivity metals behave as PEC above the NIR region prohibiting strong absorption for dielectrics with $t \leq \lambda/4 n$ where having thinner optical coatings is of paramount importance. Many low conductivity metals, however, do not behave as PEC in the NIR-SWIR-MIR regions [12]. We deposit an 80nm Ge layer on Ag and Ni substrates and show the s-polarization reflectivity for incident angles 15° to 75° . Since Ge is not highly absorbing above the NIR region, strong absorption is realized only for the Ge-Ni optical coating. In addition, the Ge layer thickness $h \sim \lambda/53 n_{Ge}$, for $n_{Ge} \sim 4$ at 1700nm. The absorption reaches up-to 99.8% and stays above 76% for all measured angles. The strong heat localization in the metallic substrate along with the relatively thin dielectric coating and low angle sensitivity makes the proposed system an excellent candidate for a bolometer where absorbed infrared radiation is transformed into a measured change in the electric conductivity.

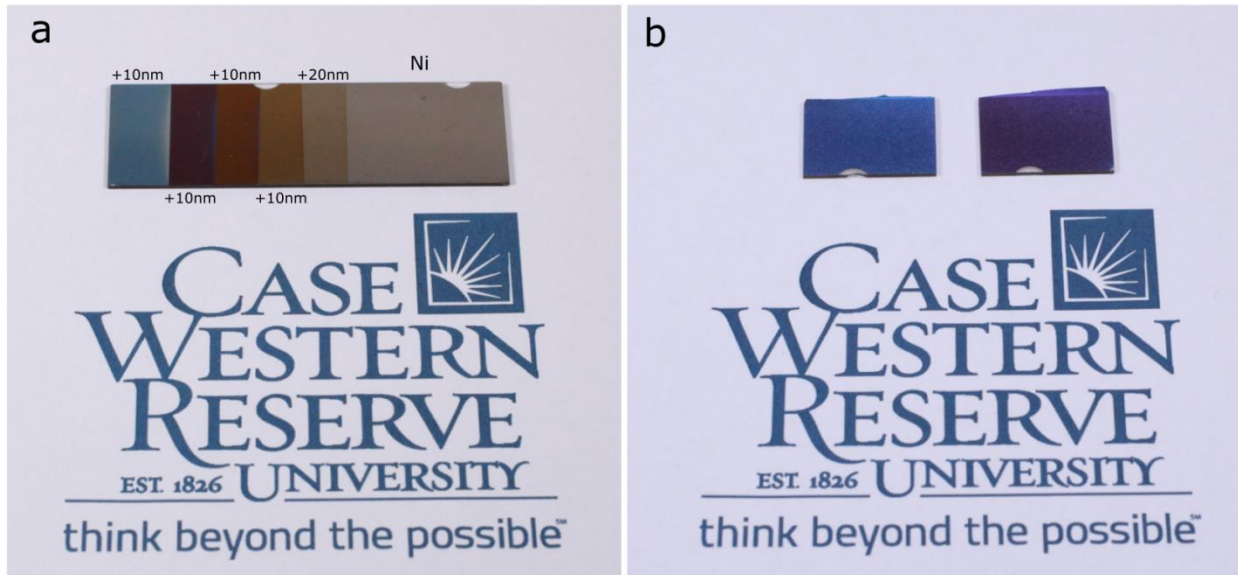


Figure 3| Optical images of visible light absorbers: a) A glass slide with a 90nm Ni film coated with different thicknesses of TiO2 showing a variety of colors. b) Shows a frosted (roughened) glass substrate with a 90nm Ni film coated with 55nm (right) and 65nm(left) TiO2. The iridescent-free property of the optical coating allows maintaining color integrity even on a rough surface.

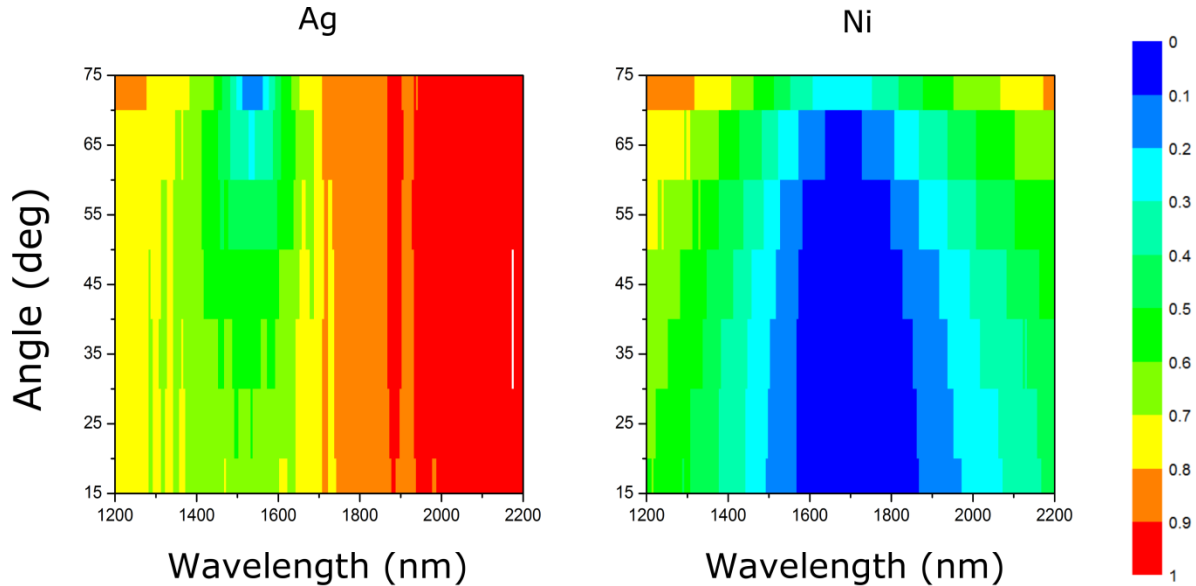


Figure 4| Short wavelength IR absorber: [add the labels] Depositing an 80nm of Ge on a) Ag, and b) Ni substrates only result in light absorption for Ni substrate because Ge has low losses for energies below the NIR. The absorption maximum corresponds to 1700nm which means that the dielectric thickness is $< \lambda/4n$. This is possible because Ni does not behave as a PEC in the SWIR region.

The lack of stringent requirements on the dielectric film has an additional advantage; by simply oxidizing the surface of a low conductivity metal, it is possible to realize structural coloring and perfect light absorption. To demonstrate this, we deposited Ni films on a thin glass slide. The glass slide was cleaned and annealed at high temperatures to ensure having a clean surface. Then we placed the metal on a hot plate with temperature $\sim 200\text{C}^0$. The Ni film quickly started to show colors similar to the colors we obtained by depositing a separate dielectric layer. Fig. 5a shows five samples of heated Ni film as the color progress over time (from left to right). We deposited Ni on a silicon wafer, and then etched the surface in order to image the film cross-section. It is clear that the film grows a thin layer of oxide on top of it which in turn determines the color of the film. Fig. 5b shows the corresponding SEM image for the yellow (second from left) and purple (fourth from left) films.

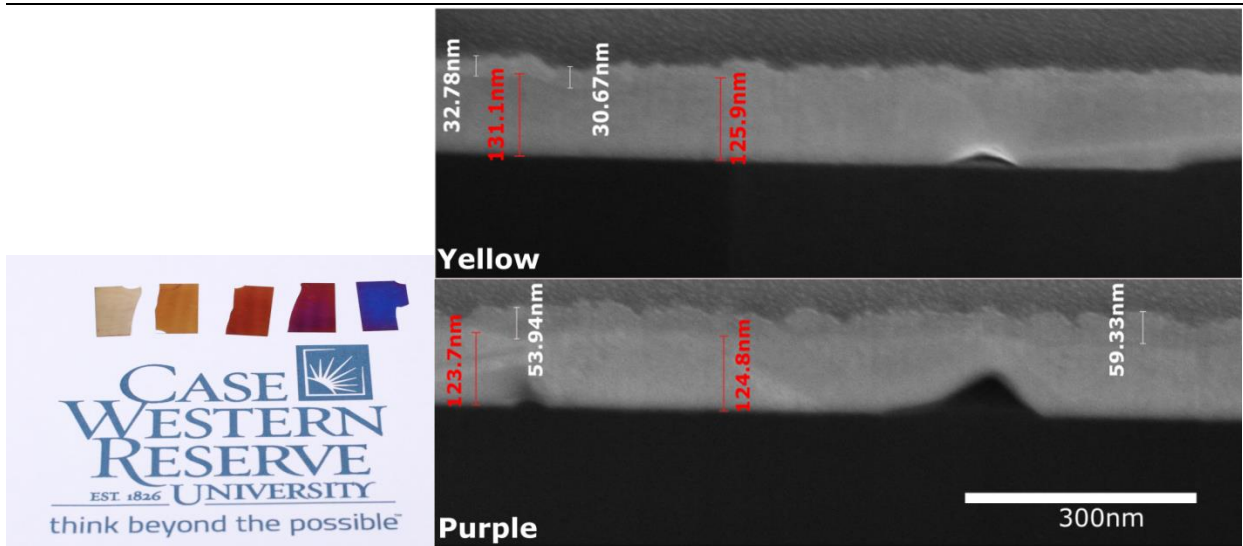


Figure 5| Oxidized metal thin-film absorber: **a)** Optical images of a Ni thin film that is heated on a hot plate showing a light-yellow, yellow, light-red, purple and blue colors. **b)** an SEM image of a cross-section in the yellow (top) and purple (bottom) films.

Performing reflectivity measurements on the yellow, purple and blue samples, we observe a wide angle range, perfect light absorption modes that redshifts for longer heating periods (thicker dielectric films).

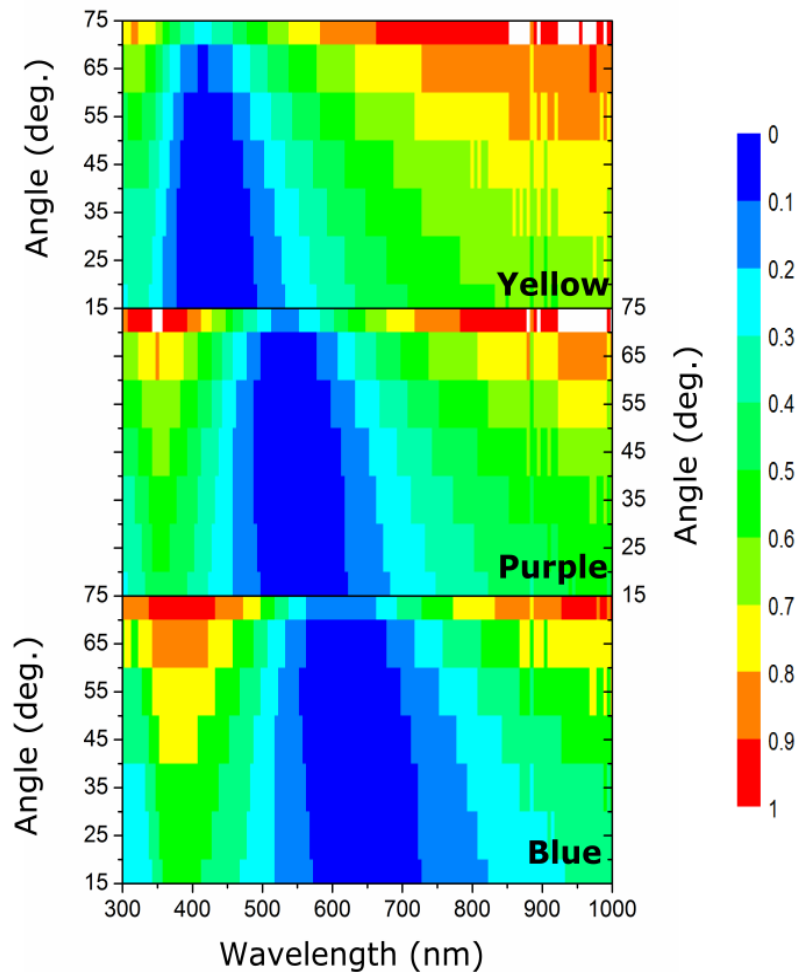


Figure 6| Reflectivity measurements for oxidized metal absorber for the a) yellow, b) purple, and c) blue samples showing a wide angle range perfect light absorption.

3-Conclusion and outlook:

The demonstrated optical absorber can be used as a platform for many applications. In the visible regime, this absorber can be directly used for structural coloring. The absorber iridescent free property would enable using it on roughed and bendable substrate which is an important feature. The simplicity of realizing perfect absorption in the NIR opens the door for applications in electromagnetic shielding in optical networks. In addition, the unique ability to achieve sub $\lambda/4n$ perfect absorption for energies below the NIR without looking for special dielectrics and/or reflecting substrates [7] makes our design attractive as a selective thermal emitter. Furthermore, since the electromagnetic energy is almost

entirely dissipated inside the metal, it is possible to use include it as the radiation sensitive element. Finally, considering that the system consists of just two films, the proposed absorber is a promising platform for gas sensing. For instance, it is possible to create a hydrogen gas sensor using a metal that can form a hydride, e.g. Pd. On the other hand, many dielectrics, e.g., metal oxides, can be used to detect many gases, e.g., CO, CO₂, and H₂ where interacting with such gases change the optical properties of the oxide [13].

Acknowledgments:

This work was done in collaboration with professor Michael Hinczewski group at CWRU. Funding for this work is from the Ohio Third Frontier Project Research Cluster on Surfaces in Advanced Materials (RC-SAM); Case Comprehensive Cancer Center, Case Western Reserve University.

4-References:

- 1- Z. Zhou, E. Sakr, Y. Sun, P. Bermel, ; Solar thermophotovoltaics: reshaping the solar spectrum, *Nanophotonics* ,5 (1):1–21, (2016). [thermophotovoltaic]
- 2- Y. Pan, *et. al.* , A Rapid Response Thin-Film Plasmonic-Thermoelectric Light Detector, *Scientific Reports*, 6, 37564 (2016). [photodetector]
- 3- Jon A. Schuller, Edward S. Barnard, Wenshan Cai, Young Chul Jun, Justin S. White & Mark L. Brongersma, Plasmonics for extreme light concentration and manipulation, *Nature Materials* 9, 193–204 (2010)
- 4- Y. Yang, *et. al.*, Femtosecond optical polarization switching using a cadmium oxide-based perfect absorber, *Nature Photonics* 11, 390–395 (2017).

-
- 5- Z. Li, S. Butun, K. Aydin, Large-Area, Lithography-Free Super Absorbers and Color Filters at Visible Frequencies Using Ultrathin Metallic Films, *ACS Photonics*, 2 (2), pp 183–188, 2015.
 - 6- M. A. Kats, R. Blanchard, P. Genevet , F. Capasso. Nanometre optical coatings based on strong interference effects in highly absorbing media. *Nature Materials*, 12, 20–24, 2013.
 - 7- M. A. Kats, F. Capasso, Optical absorbers based on strong interference in ultra-thin films *Optics, Laser & Photonics Reviews* 10 (5), 699, 2016.
 - 8- M. ElKabbash, A. Sousa-Castillo, Q. Nguyen, R. Mariño-Fernández, N. Hoffman, M. A. Correa-Duarte, G. Strangi , Tunable Black Gold: Controlling the Near-Field Coupling of Immobilized Au Nanoparticles Embedded in Mesoporous Silica Capsules, *Advanced Optical Materials*, 10.1002/adom.201700617, 2017.
 - 9- C. M. Watts, X. Liu, W. J. Padilla, Metamaterial Electromagnetic Wave Absorbers, *Advanced Materials*, 24, OP98–OP120, 2012.
 - 10- E. Hecht, *Optics*, 2nd edn., Addison-Wesley publishing, 1987.
 - 11- C. Hägglund, S. P. Apell, B. Kasemo, “Maximized Optical Absorption in Ultrathin Films and Its Application to Plasmon-Based Two-Dimensional Photovoltaics,” *Nano Lett.*, 2010, 10 (8), pp 3135–3141, 2010.
 - 12- M. A. Ordal, L. L. Long, R. J. Bell, S. E. Bell, R. R. Bell, R. W. Alexander, Jr., C. A. Ward, Optical properties of the metals Al, Co, Cu, Au, Fe, Pb, Ni, Pd, Pt, Ag, Ti, and W in the infrared and far infrared, *APPLIED OPTICS* , 22, 7 , 1983.
 - 13- C. Wang, L. Yin, L. Zhang, D. Xiang , R. Gao, Metal Oxide Gas Sensors: Sensitivity and Influencing Factors, *Sensors*, 10, 2088-2106, 2010.

Hydrogen sensing using optical coating light absorber

In the previous chapter, we demonstrated iridescent free light absorber using a low-loss dielectric and a high-loss metal. The absorption mode depends on the optical parameters of both the dielectric and the metal layer. Hence, this absorber can act as a refractometer; changes in the optical parameters of either layers induce a change in the absorption spectral properties. Palladium is a high-loss metal that forms a hydride if it is exposed to hydrogen. We use Germanium-Palladium optical coating absorber to detect hydrogen. We monitor both the spectral location of the reflection minimum λ_{\min} and the full width half maximum of the absorption mode. Due to the iridescent free absorption of the introduced absorber, the total shift in λ_{\min} was found to be also angle independent.

1- Background and introduction:

Advances in nano-lithography and nano-fabrication fueled the research in nano-photonics and opened the door for many possible applications in imaging, spectroscopy, energy, drug delivery and discovery, and sensing. Many of the introduced nano-photonics structures require intense lithography especially for operation in the UV, visible, and NIR regions. Recently, however, thin-film metamaterials that consist of alternating metal-dielectric thin films were used in order to realize the same functionalities without lithography, e.g. negative index metamaterials [1], epsilon near zero metamaterials [2] hyperbolic metamaterials [3], and perfect light absorbers [4]. Thin-film metamaterials are, accordingly, more suitable for low cost and large scale production. In this work, we use an

optical coating absorber that consists of a low-loss dielectric and high-loss metal thin films for lithographically free hydrogen sensing. The low iridescence of the absorber allows for an angle robust sensing measurements. We obtain two sensing parameters; changes in λ_{\min} and changes in the full-width half maximum (FWHM) of the absorption mode.

Recently, we introduced an interference based, thin-film optical absorber consisting of a low-loss dielectric and a high-loss metal [4]. To realize perfect light absorption in an optical coating, both Transmissivity T and Reflectivity R must be zero. Using a thick metal film eliminates T . Adding a coherent dielectric thin-film results in destructive interference which can eliminate R under certain conditions detailed in the previous chapter. The destructive interference is realized when the phase difference δ between two interfering waves is given by $\delta = \frac{4\pi}{\lambda_0} n_d t \cos \theta_d + \phi_R = 2m\pi$, where λ_0 is the wavelength of the incident light in free space, n_d is the dielectric refractive, θ_d is the refracted angle inside the dielectric, ϕ_R is the phase shift from a single reflection of the metal film, and m is an odd number. For metals with low conductivity, $\phi_R \neq \pi$ and depends on the complex permittivity of the metal [5]. Changes in the metal permittivity, hence, will change the wavelength at which destructive interference (and absorption) would take place. Note that this optical coating absorber is iridescent free especially when using a dielectric with high n_d .

Metals that form metal hydrides, e.g. Palladium (Pd) are of low conductivity and reversibly interact with intercalating adsorbed hydrogen atoms. When Pd is exposed to hydrogen it forms palladium hydride (PdH_x) with certain hydrogen atomic ratio x . The hydride has a different complex permittivity depending on x , and would yield a different reflection phase, i.e., $\phi_R(x)$. Fig. 1 shows a schematic of the proposed sensor. PdH_x exists in two solid state

phases (α and β) depending on the temperature, pressure, and hydrogen partial pressure in its environment. At low hydrogen partial pressure, intercalated hydrogen atoms are randomly situated inside the Pd lattice and the hydrogen forms a solid solution (α phase) [6]. At higher hydrogen partial pressure, hydrogen-hydrogen interactions result in a more ordered structure forming a hydride β phase [7]. In the β phase, the lattice parameter increase by $\sim 3.5\%$ as the lattice expands to accommodate the hydrogen atoms occupying new lattice sites [6]. For intermediate hydrogen partial pressures, both α and β phases coexist in a Pd film (so called α' phase) [8]. In α' and β phases, Pd experiences significant hysteresis between the formation and decomposition of the hydride phase. This hysteresis is because of the energy barrier between the hydride and metal phases due to lattice strains which does not exist in the α phase [6, 9].

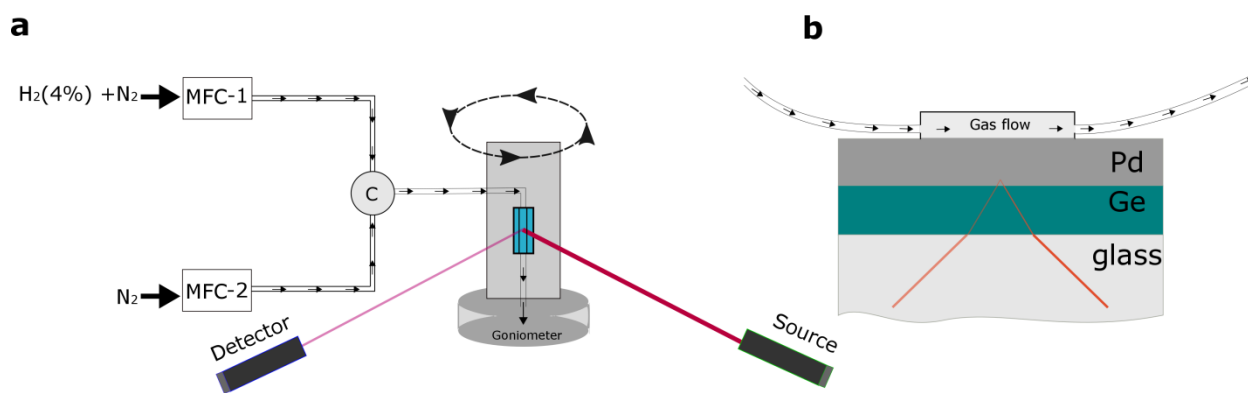


Figure 1| Schematic of the setup and sensor: a) A microfluidic channel is attached to the optical absorber and connected to two mass flow controllers (MFCs). One MFC controls the flow of nitrogen mixed with hydrogen (4% in concentration) and another MFC controls the flow of pure nitrogen. The sensor is then placed on a variable angle ellipsometer to measure the angular reflectivity. **b)** A schematic of the optical coating sensor. The microfluidic channel is attached to the top of the Pd film in order to expose Pd to the gas from the MFCs.

2- Results and Discussion:

The setup and sensor schematics are shown in Fig. 2a and 2b respectively. In order to expose the sensor to different hydrogen concentrations, we attach a microfluidic channel

on the sensor with tubing connected to a tank of nitrogen mixed with hydrogen with 4% concentration and another with pure nitrogen. Each gas source is regulated via an MFC which allows us to change the hydrogen concentration. The sensor is then placed on a variable angle ellipsometer (J. A. Wollam) to measure the reflectivity R as a function of angle. The sensor consists of a Palladium (Pd) film (20nm) on Germanium (Ge) film (60nm) deposited on a glass slide. The microfluidic channel is attached to the palladium side and the reflection is interrogated from the glass side. We obtain an absorption mode in the NIR centered around $\lambda_{\min} \sim 1450\text{nm}$. Note that, according to our ellipsometry fitting, Ge has low losses in the NIR and that most of the absorption occurring inside the Pd layer. We used Ge since it has high refractive index in order to realize iridescent free absorption [4]. The angle dependence of nano-photonics gas sensors [6] would be a major disadvantage when it comes to device engineering as it imposes additional restrictions on the sensing device design.

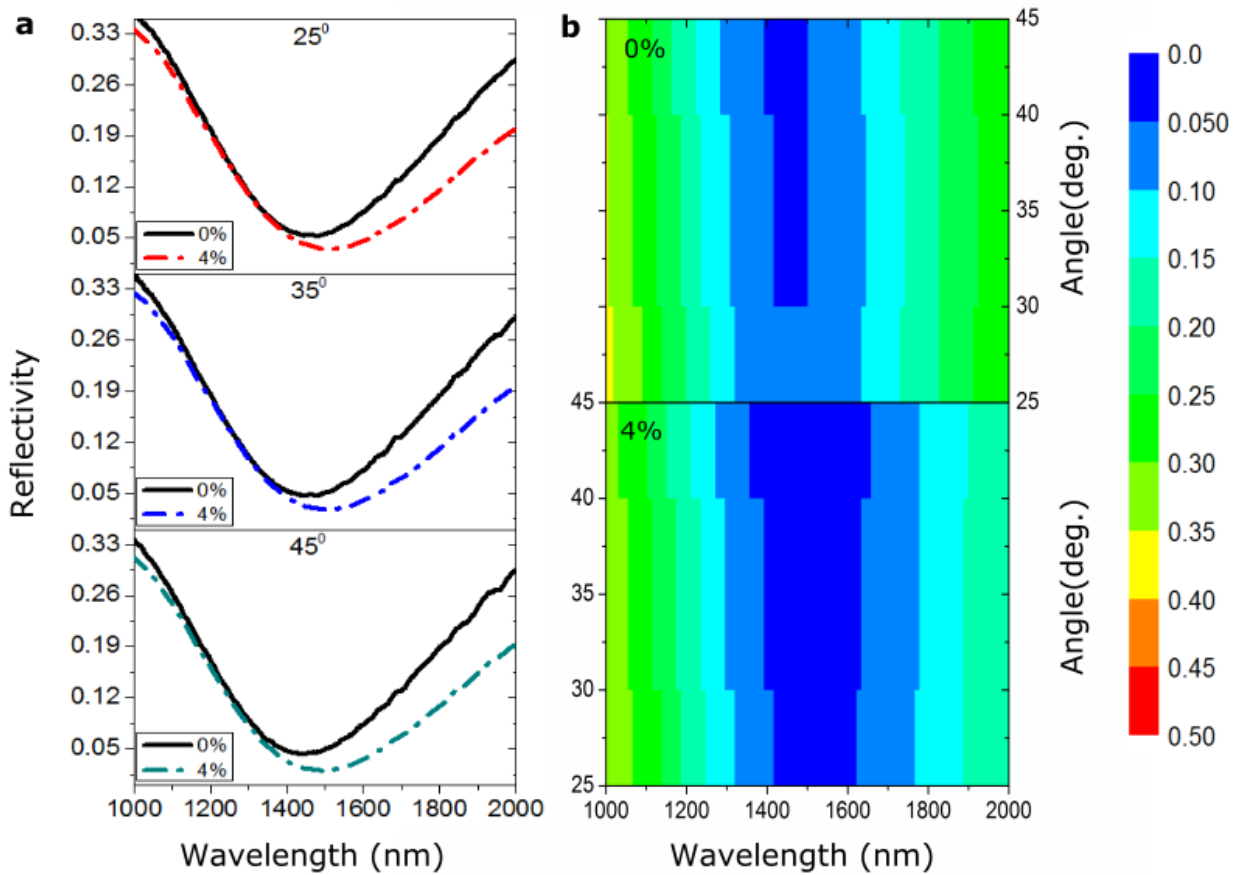


Figure 2| Sensitivity for different angles of incidence: a) reflectivity measurements for the optical absorber before and after introducing hydrogen with $C=4\%$ for three different incident angles 25° , 35° , and 45° . **b)** A contour plot for the reflectivity (color bar range 0-0.50 R) shows the angular reflection of the absorber. The FWHM increases significantly after introducing hydrogen for all incident angles.

In order to evaluate the sensitivity and angular sensitivity of the sensor, we performed measurements for hydrogen concentration $C=4\%$ for 25° , 35° , and 45° angles of incidence. The total shift in λ_{\min} is $46 \pm 2\text{nm}$, $47 \pm 2\text{nm}$, and $45 \pm 2\text{nm}$, for 25° , 35° , and 45° , respectively (Fig. 2a). The low iridescence in the destructive interference condition of the absorber is maintained even after introducing hydrogen which highlights the sensor angular robustness. Fig. 2b shows the angular reflectivity contour plot for the sensor exposed to N_2 and $\text{N}_2 + \text{H}_2(4\%)$. The modification in the absorptivity of the metal hydride

resulted in a significant broadening in the absorption mode. The change in the FWHM is $195 \pm 4\text{nm}$, $186 \pm 4\text{nm}$, and $228 \pm 4\text{nm}$, for 25° , 35° , and 45° respectively. This is a measurable, and likely more convenient, signal that can be monitored using a broadband light source.

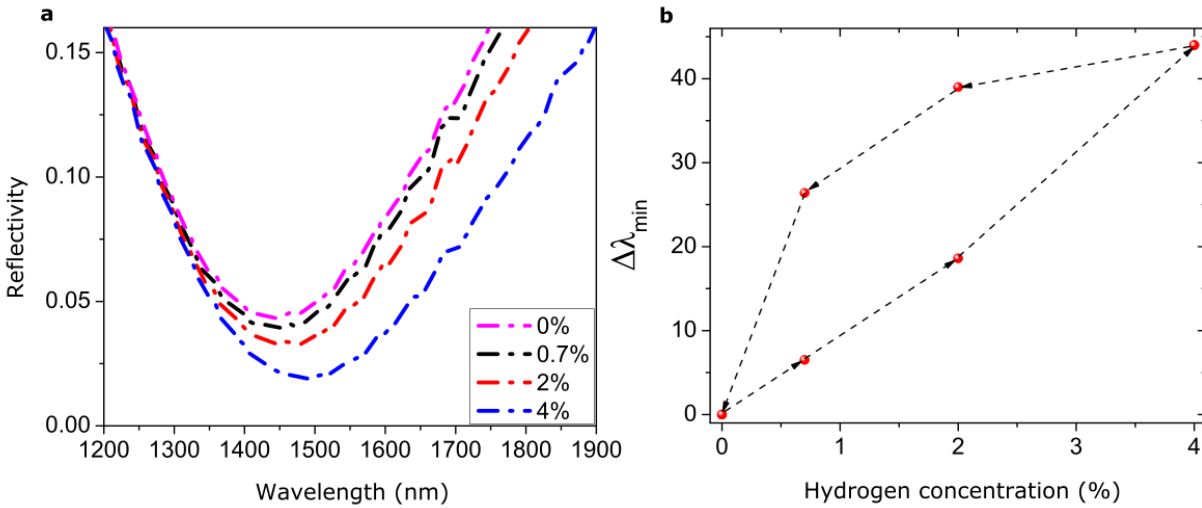


Figure 3| Sensitivity for different hydrogen concentration: a) Reflectivity of the absorber as a function of hydrogen concentration. b) Hysteresis in the shift in reflectivity minimum λ_{\min} .

Fig.3a shows the shift in the absorption mode for a given angle (45°) as a function of hydrogen concentration. We obtained a shift of 6.5nm, 18.6nm, and 44nm for hydrogen concentrations $C=0.7\%$, 2%, and 4%, respectively. As we eluded before, for hydrogen concentrations leading to the creation of α' or β phases (high values of x), hysteresis in thin-film hydrogen sensors is always present. The hysteresis is due to the existence of a mechanical energy barrier due to the coherency strain produced by the lattice expansion in the hydride phase [9]. The energy barrier prevents releasing hydrogen atoms situated inside the hydride lattice. Fig. 3b shows the sensor response of the cycled hydrogen response for hydrogen concentrations (0%, 0.7%, 2% and 4%) at 45° incidence angle. Due to hysteresis, the hydrogen atomic ratio at a given hydrogen concentration is different; the atomic ratio is higher during relaxation as deintercalation is hindered due to coherency

strains. The existence of coherency strain, however, did not affect the overall performance of our sensor as the cavity mode relaxed to its initial state and the maximum shift at H₂ (4%), was maintained.

In summary, we have introduced a large area, lithographically free hydrogen sensor using an optical coating absorber. The spectral shift in the reflection minimum was monitored and it showed high sensitivity. Due to the reduced angular dependence of the absorption mode of the optical coating, the sensitivity was also angle independent. We also noted a strong change in the FWHM of the absorber when it is exposed to hydrogen. Like other metal-hydride hydrogen sensors, our sensor suffers from hysteresis. However, the sensor maintains its structural integrity even after several sensing cycles.

Acknowledgments:

This work was done in collaboration with professor Michael Hinczewski group, Professor Mohan Sankaran group, and Professor Umut Gurken group at CWRU. Funding for this work is from the Ohio Third Frontier Project Research Cluster on Surfaces in Advanced Materials (RC-SAM); Case Comprehensive Cancer Center, Case Western Reserve University.

3- References:

- [1] J. Gao, *et al.* "Experimental realization of epsilon-near-zero metamaterial slabs with metal-dielectric multilayers," *Applied Physics Letters*, 103, 5, 2013.
- [2] Ting Xu, Amit Agrawal, Maxim Abashin, Kenneth J. Chau & Henri J. Lezec, All-angle negative refraction and active flat lensing of ultraviolet light, *Nature* 497, 470–474 (23 May 2013).
- [3] K. V. Sreekanth, *et al.*, "Extreme sensitivity biosensing platform based on hyperbolic metamaterials," *Nature Materials* 15, 621–627 (2016).
- [4] M. ElKabbash, E. Ilker, T. Letsou, N. Hoffman, A. Yaney, M. Hinczewski, G. Strangi, Iridescence-free and narrowband perfect light absorption in critically coupled metal high-index dielectric cavities, *Optics letters*, 42, 18, 3598-3601, 2017.
- [6] S. Syrenova, C. Wadell, F. A. A. Nugroho, T. A. Gschneidner, Y. A. Fernandez, G. Nalin, D. Świtlik, F. Westerlund, T. J. Antosiewicz, V. P. Zhdanov, K. Moth-Poulsen, C. Langhammer, Hydride formation thermodynamics and hysteresis in individual Pd nanocrystals with different size and shape, *Nature Materials* 14, 1236–1244, 2015.
- [7] N. R. Fong, P. Berinibc, R. N. Taita, Hydrogen sensing with Pd-coated long-range surface plasmon membrane waveguides, *Nanoscale*, 7, 2016.
- [8] F.D. Manchester, A. San-Martin, J.M. Pitre, The H-Pd (Hydrogen-Palladium) System, *Journal of Phase Equilibria*, 15, 1, 1994.
- [9] Schwarz, R. B. & Khachaturyan, A. G. Thermodynamics of open two-phase systems with coherent interfaces: Application to metal–hydrogen systems. *Acta Mater.* 54, 313–323, 2006.

Bibliography

- 1- J. B. Khurgin, How to deal with the loss in plasmonics and metamaterials, *Nature Nanotechnology* 10, 2–6 (2015)
- 2- E. Le, R. Pablo Etchegoin, *Principles of Surface-Enhanced Raman Spectroscopy*, 1st edition. Elsevier Science, 2008.
- 3- A. Zayats, I. Smolyaninov, A. A. Muradudin, Nano-optics of surface plasmon polaritons, Volume 408, Issues 3–4, Pages 131-314, 2005.
- 4- M. Pelton, G. W. Bryant, *Introduction to Metal-Nanoparticle Plasmonics*, Wiley, 2013.
- 5- S. A. Maier, *Plasmonics: Fundamentals and Applications*, Springer Science & Business Media, 2007.
- 6- W. D. Newman, C. L. Cortes, J. Atkinson, S. Pramanik, R. G. DeCorby, Z. Jacob. Ferrell–Berreman Modes in Plasmonic Epsilon-near-Zero Media, *ACS Photonics*, 2 (1), 2015.
- 7- M. Sukharev, A. Nitzan, Optics of plasmon-exciton nanomaterials, *Journal of Physics: Condensed Matter*, 2017.
- 8- L. Cao, M. L. Brongersma, Active Plasmonics: Ultrafast developments, *Nature Photonics* 3, 12 – 13, 2009.
- 9- A. V. Krasavin, N. I. Zheludev, Active plasmonics: Controlling signals in Au/Ga waveguide using nanoscale structural transformations. *Applied Physics Letters*, 84, 1416 –1418 (2004).
- 10-T. B. Hoang, M. H. Mikkelsen, Broad electrical tuning of plasmonic nanoantennas at visible frequencies , , *Applied Physics Letters* , 108 , 18 , 183107, 2016.

-
- 11-Y. Abate, R. E. Marvel, J. I. Ziegler, S. Gamage, M. H. Javani, M. I. Stockman, R. F. Haglund, Control of plasmonic nanoantennas by reversible metal-insulator transition *Scientific Reports*, 5, 13997, 2015.
 - 12-S. Link, M. A. El-Sayed, Spectral properties and relaxation dynamics of surface plasmon electronic oscillations in gold and silver nanodots and nanorods, *The Journal of Physical Chemistry B*, 103 ,40, Pages 8410-8426, 1999.
 - 13-P. Guo, R. D. Schaller, J. B. Ketterson, R. P. H. Chang, Ultrafast switching of tunable infrared plasmons in indium tin oxide nanorod arrays with large absolute amplitude. *Nature Photonics*. 10, 267–273 (2016).
 - 14-Y. Yang, K. Kelley, E. Sacht, S. Campione, T. S. Luk, J.,-P., Maria, M. B. Sinclair, I. Brener, Femtosecond optical polarization switching using a cadmium oxide-based perfect absorber . *Nature Photonics*, 11, 390–395 (2017).
 - 15-K. F. MacDonald, Z. L. Sámsón, M. I. Stockman , N. I. Zheludev, Ultrafast active plasmonics, *Nature Photonics* 3, 55 - 58 (2009).
 - 16-N. Rotenberg, M. Betz, H. M van Driel, Ultrafast control of grating-assisted light coupling to surface plasmons, *Optics letters* , 33 , 18 , 2137-2139, 2008.
 - 17-M. Pelton Modified Spontaneous Emission in Nanophotonic Structures. *Nature Photonics*. 9, 427–435, 2015.
 - 18-J. H. Simmons, K. S. Potter, *Optical Materials*, Academic Press, 2000.
 - 19- H. A. Atwater. *Sci. Am.* 2007, 296, 56.
 - 20-J. B. Pendry, D. R. Smith, *Sci. Am.* 2006, 295, 60.
 - 21-E. Ozbay, *Science* 2006, 311, 189.
 - 22-S. Schlücker, *Angew. Chem. Int. Ed.* 2014, 53, 4756.

-
- 23-X. Huang, M. A. El-Sayed, J. Adv. Res. 2010, 1, 13.
- 24-M. Hedayati, F. Faupel. J. Materials 2014, 7, 1996.
- 25-C. M. Watts, X. L. Liu, W. J. Padilla. Adv. Mater. 2012, 24, 98.
- 26-J. B. Khurgin. Nat. Nanotechnol. 2015, 10, 2.
- 27-U. Kreibig, C. V. Fragstein. Phys. 1969, 224, 307.
- 28- M. El Kabbash, R. A. Rashed, K. V.Sreekanth, A. De Luca, M. Infusino, G. Strangi. J. Nanomat. 2016, 2016, 1.
- 29- N. M. Lawandy. Appl. Phys. Lett. 2004, 85, 5040.
- 30-G. Strangi, A. De Luca, S. Ravaine, M. Ferrie, R. Bartolino. Appl. Phys. Lett. 2011, 98, 251912.
- 31- A. De Luca, M. P. Grzelczak, I. Pastoriza-Santos, L. M. Liz-Marzan, M. La Deda, M. Striccoli, G. Strangi. ACS Nano. 2011, 5, 5823.
- 32-M. Infusino, A.De Luca, A.Veltri, C. Vazquez-Vazquez, M. A. Correa-Duarte, R. Dhama, G. Strangi. ACS Photonics 2014, 1, 371
- 33- S. Xiao, V. P. Drachev¹, A. V. Kildishev¹, X. Ni¹, U. K. Chettiar, H.-K. Yuan¹, V. M. Shalaev. Nature 2010 , 466, 735.
- 34-O. Hess, J. B. Pendry, S. A. Maier, R. F. Oulton, J. M. Hamm. Nat. Mater. 2012 , 11, 573.
- 35- N. Meinzer, M. Ruther, S. Linden, C. M. Soukoulis, G. Khitrova, J. Hendrickson, J. D. Oltzky, H. M. Gibbs, M. Wegener. Opt. Express 2010, 18, 24140.
- 36-J. Y. Suh, C. H. Kim, W. Zhou, M. D. Huntington, T. D. Co, M. R. Wasielewski, T. W. Odom. Nano Lett., 2012, 12, 5769.
- 37-J. M. Hamm,S. Wuestner, K. L. Tsakmakidis, O. Hess. Phys. Rev. Lett. 2011, 107, 167405.

-
- 38- M. Quinten, U. Kreibitz. *Surf. Sci.* 1986, 172, 557.
- 39- C. Burda, S. Link, T. C. Green, M. A. El-Sayed. *J. Phys. Chem. B* 1999, 103, 10775.
- 40- S. Hunsche, T. Dekorsy, V. Klimov, H. Kurz. *Appl. Phys. B* 1996, 62, 3.
- 41- X.Wang, Y. Guillet, P. R. Selvakannan, H. Remita, B. Palpant. *J. phys. Chem. B.* 2015, 119, 7416.
- 42- S. Link, M. A. El-Sayed. *J. Phys. Chem. B.* 1999, 103, 8410.
- 43- T. S. Ahmadi, S. L. Logunov, M. A. El-Sayed. *J. Phys. Chem. B* 1999, 100, 8059.
- 44- D. D. Ryutov. *Plasma Phys. Control. Fusion* 1999, 41, A1.
- 45- P. K. Jain, W. Qian, M. A. El-Sayed. *J. Phys. Chem. B* 2006, 110, 136.
- 46- C. D. Grant, A. M. Schwartzberg, T. J. Norman, J. Z. Zhang. *J. Am. Chem. Soc.* 2003, 125, 549.
- 47- M. J. Feldstein, C. D. Keating, Y.H. Liau, M. J. Natan, N. F. Scherer. *J. Am. Chem. Soc.* 1997, 119, 6638.
- 48- B. A. Smith, J. Z. Zhang, U. Giebel, G. Schmid. *Chem. Phys. Lett.* 1997, 270, 139.
- 49- S. Link, M. A. El-Sayed. *Int. Rev. Phys. Chem.* 2000, 19, 3, 409.
- 50- R. Dhama, A. R. Rashed, V. Caligiuri, M. El Kabbash, G. Strangi, A. De Luca. *Opt. Express.* 2016, 24, 13, 14632.
- 51- R. W. Schoenlein, W. Z. Lin, J. G. Fujimoto, G. L. Esley. *Phys. Rev. Lett.* 1987, 58, 1680.
- 52- R. F. Oulton. *Nat. Phot.* 2012, 6, 219.
- 53- A. R. Rashed, A. De Luca, R. Dhama, A. Hosseinzadeh, M. Infusino, M. El Kabbash, S. Ravaine, R. Bartolino, G. Strangi. *RSC Adv.* 2015, 5, 53245.
- 54- G. Lilley, M. Messner, K. Unterrainer. *Opt. Mater. Express*, 2015, 5, 2112.

-
- 55-A. De Luca, N. Depalo, N.E. Fanizza, M. Striccoli, M. L. Curri, M. Infusino, A. R. Rashed, M. La Deda, G. Strangi. *Nanoscale* 2013, 5, 6097.
- 56- Akselrod, G. M., Argyropoulos, C., Hoang, T. B., Ciraci, C., Fang, C., Huang, J., Smith, D. R., Mikkelsen, M.H. Probing the mechanisms of large Purcell enhancement in plasmonic nanoantennas. *Nat. Photonics* **8**, 835–840 (2014).
- 57- Pelton, M. Modified Spontaneous Emission in Nanophotonic Structures. *Nat. Photonics*. **9**, 427–435 (2015).
- 58- Lodahl, P., Driel, A., Nikolaev, I., Irman, A. Controlling the dynamics of spontaneous emission from quantum dots by photonic crystals. *Nature* **430**, 654–657 (2004).
- 59- Purcell, E. Spontaneous emission probabilities at radio frequencies. *Phys. Rev.* **69**, 681(1946).
- 60- Gross, M., Haroche, S., *Physics Reports, Review Section of Physics Letters*, 93, 5 301-396 (1982).
- 61- Pustovit, V. N., Shahbazyan, T. V., Cooperative emission of light by an ensemble of dipoles near a metal nanoparticle: The plasmonic Dicke effect , *Phys. Rev. Lett.* 102, 077401, (2009).
- 62- Dicke , R. H., Coherence in Spontaneous Radiation Processes, *Phys. Rev.* 93, 99 , 1, (1954).
- 63- Khurgin, J. B. How to deal with the loss in plasmonics and metamaterials. *Nature Nanotechnol.* **10**, 2–6 (2015).
- 64- Russell, K. J., Liu, T., Cui, S. & Hu, E. L. Large spontaneous emission enhancement in plasmonic nanocavities. *Nature Photon.* **6**, 459462 (2012).

-
- 65- Kroekenstoel, E. J. A., Verhagen, E., Walters, R. J., Kuipers, L., Polman, A. Enhanced spontaneous emission rate in annular plasmonic nanocavities *Appl. Phys. Lett.* **95**, 263106 (2009).
- 66- Kinkhabwala, A. *et al.* Large single-molecule fluorescence enhancements produced by a bowtie nanoantenna, *Nat. Photonics* **3**, 654-657 (2009).
- 67- Goffard, J. *et al.* Plasmonic engineering of spontaneous emission from silicon nanocrystals. *Sci. Rep.* **3**, 2672 (2013).
- 68- M. Pelton, G. Bryant, G. Introduction to Metal-Nanoparticle Plasmonics. (Wiley, Science Wise Publishing, Hoboken, NJ, USA, 2013).
- 69- Shahbazyan, T. V., Local Density of States for Nanoplasmonics, *Phys. Rev. Lett.* **117**, 207401, (2016).
- 70- Praveena, M., Mukherjee, A., Venkatapathi, M., Basu, J. K., Plasmon-mediated emergence of collective emission and enhanced quantum efficiency in quantum dot films, *Phys. Rev. B*, **92**, 235403 (2015).
- 71- Mikhail, G., Shestakov, V., Fron, E., Chibotaru, L. F., Moshchalkov, V. V., Plasmonic Dicke Effect in Ag-Nanoclusters-Doped Oxyfluoride, *J. Phys. Chem. C*, **119** (34), 20051–20056, (2015).
- 72- D. Miller, *Proceedings of the IEEE*, **97**, 7, (2009).
- 73- M.S. Eggleston *et al.* *Proc. Nat. Acad. Sci.*, **112**, 1704–1709 (2015).
- 74- Protsenko, I.E., Uskov, A.V., Superradiance of several atoms near a metal nanosphere *Quantum Electronics* **45** (6) 561 – 572 (2015).

-
- 75- Hiroshige, N., Ihara, T., Kanemitsu, Y., Simultaneously measured photoluminescence lifetime and quantum yield of two-photon cascade emission on single CdSe/ZnS nanocrystals, *Phys. Rev. B* **95**, 245307 (2017).
- 76- Matsuzaki, K., *et. al.*, Strong plasmonic enhancement of biexciton emission: controlled coupling of a single quantum dot to a gold nanocone antenna, *Scientific Reports* **7**, Article number: 42307 (2017).
- 77- Jin, C.-Y., Johne, R., Swinkels, M. Y., Hoang, T. B., Midolo, L., van Veldhoven, P. J. , Fiore, A. Ultrafast non-local control of spontaneous emission. *Nat. Nanotechnol.* **9**, 886–890 (2014).
- 78- Pagliano, F., Cho, Y., Xia, T., van Otten, F., Johne, R., Fiore, A. Dynamically controlling the emission of single excitons in photonic crystal cavities. *Nat. Commun.* **5**, 5786 (2014).
- 79- Thomas, D., Walsh, B. M. and Gupta, M. C. CdSe(ZnS) nanocomposite luminescent high temperature sensor. *Nanotech.* **22**, 185503 (2011).
- 80- He-lin ,W. , Ai-jun ,Y. , Cheng-hua, S., Luminescent high temperature sensor based on the CdSe/ ZnS quantum dot thin film. *Optoelectron. Lett.* **9**,6,1 (2013).
- 81- Crookera, S. A. , Barrick , T. , Hollingsworth, J. A. , Klimov, V. I. , Multiple temperature regimes of radiative decay in CdSe nanocrystal quantum dots: Intrinsic limits to the dark-exciton lifetime. *App. Phys. Lett.*, **82**,17 (2003).
- 82- de Mello Donegá, C. , Bode, M., Meijerink, A., Size- and temperature-dependence of exciton lifetimes in CdSe quantum dots. *Phys. Rev. B*, **74**, 085320 (2006).

-
- 83- Ringler, M., Schwemer, A., Wunderlich, M., Nichtl, A., Kürzinger, K., Klar, T. A., Feldmann, J. Shaping emission spectra of fluorescent molecules with single plasmonic nanoresonators. *Phys. Rev. Lett.* **100**, 203002 (2008).
- 84- H. M. Branz, W. Regan, K. J. Gerst, J. B. Borakac , E. A. Santoria , *Energy Environ. Sci.*, 2015, 8, 3083-3091.
- 85- A. O. Govorova, H. H. Richardson, *Nano Today*, 2007, 2, 1, 30–38.
- 86- N. Bonod, G. Tayeb, D. Maystre, S. Enoch, E. Popov, *Opt. Express* , 2008, 16, 15431–15438.
- 87- T. Søndergaard, S. M. Novikov, T. Holmgaard, R. L. Eriksen, J. Beermann, Z. Han, K. Pedersen , S. I. Bozhevolnyi, *Nat. Comm.* 2012, 3, 969.
- 88- V. G. Kravets, F. Schedin, A. N. Grigorenko, *Phys. Rev. B* , 2008, 78, 205405.
- 89- K. Aydin, V. E. Ferry, R. M. Briggs , H. A. Atwater, *Nat. Comm.*, 2011, 2, 517.
- 90- D. R. McKenzie, *Gold Bull.* 1978 ,11 ,49. See [109, 140]
- 91- A. Y. Vorobyev, C. Guo, *Phys. Rev. B* , 2005, 72, 195422.
- 92- D. Liu, F. Zhou, C. Li, T. Zhang, H. Zhang, W. Cai, Y. Li, *Angew. Chem*, 2015, 54, 33 , 10,9596–9600.
- 93- K. Bae, G. Kang, S. K. Cho, W. Park, K. Kim, W. J. Padilla, *Nat. Comm.* 2015, 6, 10103 10103.
- 94- S. Link, M. El-Sayed, *Int Rev Phys Chem.* 2000, 19, 3, 409-453.
- 95- M. Quinten and U. Kreibig, *Surf. Sci.* 1986 172(3), 557-577.
- 96- V. M. Wallace, N. R. Dhumal, F. M. Zehentbauer, H. J. Kim,, J. Kiefer, *J. Phys. Chem. B*, 2015, 119 (46), pp 14780–14789.
- 97- P. B. Johnson , R. W. Christy, *Phys. Rev. B: Solid State*, 1972, 6, 4370.

-
- 98-D. G. Duff, A. Baiker, P. P. Edwards, *Langmuir* 1993, 9, 2301.
- 99-T. Pham, J. B. Jackson, N. J. Halas, T. R. s. Lee, *Langmuir* 2002, 18, 4915–4920.
- 100- N. Lawandy, *Proc. SPIE* 5924, 2005, *Complex Mediums VI: Light and Complexity*, 59240G.
- 101- M. Pelton, G. Bryant, G. Introduction to Metal-Nanoparticle Plasmonics. Wiley, Science Wise Publishing, Hoboken, NJ, USA, 2013.
- 102- S. K. Ghosh, T. Pal, *Chem. Rev.* 2007, 107, 4797
- 103- M. Sanlés-Sobrido, W. Exner, L. Rodríguez-Lorenzo, B. Rodríguez-González, M. A. Correa-Duarte, R. A. Alvarez-Puebla, L. Liz-Marzán, *J. Am. Chem. Soc.* 2009, 131, 2699–2705.
- 104- M. Sanlés-Sobrido, M. Pérez-Lorenzo, B. Rodríguez-González, V. Salgueiriño, M. A. Correa-Duarte, *Angew. Chem., Int. Ed.* 2012, 51, 3877–3882.
- 105- C. Deeb, X. Zhou, J. Plain, G. P. Wiederrecht, R. Bachelot. M. Russell, P. K. Jain. *J. Phys. Chem. C.* 2013, 117,10669-10676.
- 106- M. El Kabbash , A. R. Rashed, K. V. Sreekanth, A. De Luca, M. Infusino , G. Strangi. *J. Nanomat.*, 2016, 21.
- 107- C. Oleari, *Color in optical coatings, Optical Thin Films and Coatings*, Pages 391–424, 425e (Woodhead Publishing Series in Electronic and Optical Materials, 2013).
- 108- J. Gao, *et al.* “ Experimental realization of epsilon-near-zero metamaterial slabs with metal-dielectric multilayers,” *Applied Physics Letters*,103, 5 , 2013.

-
- 109- Ting Xu, Amit Agrawal, Maxim Abashin, Kenneth J. Chau & Henri J. Lezec , All-angle negative refraction and active flat lensing of ultraviolet light, *Nature* 497, 470–474 (23 May 2013).
- 110- K. V. Sreekanth, *et. al.*,”Extreme sensitivity biosensing platform based on hyperbolic metamaterials,” *Nature Materials* 15, 621–627 (2016).
- 111- Born, M & Wolf, E *Principles of Optics* 7th edn, Cambridge Univ. Press, 2003.
- 112- E. Hecht, *Optics*, 2nd edn., Addison-Wesley publishing, 1987.
- 113- J. H. Simmons, K. S. Potter, *Optical Materials*, Academic Press, 2000.
- 114- Z. Li, E. Palacios, S. Butun, H. Kocer , K. Aydin, “Omnidirectional,broadband light absorption using large-area, ultrathin lossy metallicfilm coatings,” *Sci. Rep.*5, 15137, 2015.
- 115- Z. Li, S. Butun, K. Aydin, “Large-Area, Lithography-Free Super Absorbers and Color Filters at Visible Frequencies Using Ultrathin MetallicFilms,” *ACS Phot.*2, 2, 183-188, 2015.
- 116- M. A. Kats, R. Blanchard, P. Genevet , F. Capasso, “Nanometer optical coatings based on strong interference effects in highly absorbingmedia,” *Nat. Mat.*12, 20-24 , 2013.
- 117- C. Hägglund, S. P. Apell, B. Kasemo, “Maximized Optical Absorption in Ultrathin Films and Its Application to Plasmon-Based Two-Dimensional Photovoltaics,” *Nano Lett.*, 2010, 10 (8), pp 3135–3141, 2010.
- 118- Z. Li, E. Palacios, S. Butun, H. Kocer , K. Aydin. *Sci. Rep.*, **2015**, 5, 15137.
- 119- Y.-K. R. Wu, A. E. Hollowell, C. Zhang , L. J. Guo. *Sci Rep.*, **2013**, 3, 1194.
- 120- M. A. Kats, R. Blanchard, P. Genevet , F. Capasso. *Nat. Mat.*, **2013**, 12, 20–24.

-
- 121- Z. Li, S. Butun, K. Aydin. ACS Phot., **2015**, 2, 2, 183-188.
- 122- H. Shin, M. F. Yanik, S. Fan. App. Phys. Lett., **2004**, 84, 22.
- 123- K.-T. Lee, S. Seo, J. Y. Lee, L. J. Guo. Adv. Mat., 2014, 26, 36, 24, 6324–6328.
- 124- J.-B. You, W.-J. Lee, D. Won, K. Yu. Opt. Exp. **2014**, 22, 7.
- 125- C. M. Watts, X. Liu, W. J. Padilla, Adv. Mater., **2012**, 24, OP98.
- 126- D. Liu, H.T. Yu, Y.Y. Duan, Q. Li, Y.M. Xuan. Sci. Rep., **2016**, 6, 3251.
- 127- V.J. Logeeswaran, N. P. Kobayashi, M. S. Islam, W. Wu, P. Chaturvedi, N. X. Fang, S. Y. Wang, R. S. Williams, Nano Lett. **2009**, 9 (1), 178-182.
- 128- M. A. Kats, F. Capasso. Laser Photon. Rev., **2016**, 10(5), 699-699.
- 129- A.R. Forouhi, I. Bloomer. Phys. Rev. B. 34, 7018–7026 (**1986**).
- 130- A.R. Forouhi, I. Bloomer. Phys. Rev. B. 38, 1865–1874 (**1988**).
- 131- U. Y. Honghua, J. D’Archangel, M. L. Sundheimer, E. Tucker. Phys. Rev. B, 91, 235137, (**2015**).
- 132- G. D. Boreman, M. B. Raschke. Phys. Rev. B 91, 235137, (**2015**).
- 133- R. Brendel and D. Bormann. J. Appl. Phys. 71, 1-6 (**1992**).
- 134- A. D. Rakic, A. B. Djurisic, J. M. Elazar, M. L. Majewski. Applied Optics 37 (22), 5271-5283, (**1998**).
- 135- F. L. Pedrotti, L. M. Pedrotti, L. S. Pedrotti, Introduction to Optics, 3rd edition, Pearson education limited, **2006**.
- 136- R. Pitts, P. Liu, S-H. Lee, E. Tracy, Interfacial Stability of Thin Film Hydrogen Sensors, proceedings of the 2001 DOE hydrogen program review, 2001.

-
- 137- S. Syrenova, C. Langhammer Plasmonic Hydrogen Sensing with Nanostructured Metal Hydrides Carl Wadell, ACS Nano,, 8 (12), pp 11925–11940, 2014.
- 138- N. R. Fong, P. Berinibc , R. N. Taita, Hydrogen sensing with Pd-coated long-range surface plasmon membrane waveguides, Nanoscale, 7, 2016.
- 139- J. R Wilkins, G. E.Stoner, E. H. Boykin, Microbial Detection Method Based on Sensing Molecular-Hydrogen. Appl. Microbiol. 27, 949–952, 1974.
- 140- C. H. S. Hitchcock, Determination of Hydrogen as a Marker in Irradiated Frozen Food. J. Sci. Food Agric. 80, 131–136, 2000.
- 141- N. Liu, M. L. Tang, M. Hentschel, H. Giessen, A. P. Alivisatos, Nanoantenna-enhanced gas sensing in a single tailored nanofocus, Nature Materials 10, 631–636, 2011.
- 142- X. Bévenot, A. Trouillet, C. Veillas, H. Gagnaire, M. Clément, Surface plasmon resonance hydrogen sensor using an optical fibre, Meas. Sci. Technol. 13, 118, 2002.
- 143- A. Tittl, P. Mai, R. Taubert, D. Dregely, N. Liu, H. Giessen, Palladium-Based Plasmonic Perfect Absorber in the Visible Wavelength Range and Its Application to Hydrogen Sensing, Nano Lett., 11 (10), pp 4366–4369, 2011.
- 144- S. Syrenova, C. Wadell, F. A. A. Nugroho, T. A. Gschneidtnr, Y. A. Fernandez, G. Nalin, D. Świtlik, F. Westerlund, T. J. Antosiewicz, V. P. Zhdanov, K. Moth-Poulsen, C. Langhammer, Hydride formation thermodynamics and hysteresis in individual Pd nanocrystals with different size and shape, Nature Materials 14, 1236–1244, 2015.
- 145- F.D. Manchester, A. San-Martin, J.M. Pitre, The H-Pd (Hydrogen-Palladium) System, Journal of Phase Equilibria, 15, 1, 1994.

-
- 146- Schwarz, R. B. & Khachaturyan, A. G. Thermodynamics of open two-phase systems with coherent interfaces: Application to metal–hydrogen systems. *Acta Mater.* 54, 313–323, 2006.
- 147- Y. Zhao ; Q.-l. Wu ; Y.-n. Zhang, High-Sensitive Hydrogen Sensor Based on Photonic Crystal Fiber Model Interferometer, *66*, 8, 2017.
- 148- Peter Ngene, Tsveta Radeva, Martin Slaman, Ruud J. Westerwaal, Herman Schreuders, Bernard Dam Seeing Hydrogen in Colors: Low-Cost and Highly Sensitive Eye Readable Hydrogen Detectors, *advanced functional materials*, 24, 16, 23, 2374–2382, 2014.
- 149- M. Serahtlioglu, M. Erhatlioglu, S. Ayas, N. Biylikli, A. Dana, M. E. Solmaz, Perfectly absorbing ultra-thin interference coatings for hydrogen sensing, *Optics Letters*, 41, 8, 2016.
- 150- E. Hecht, *Optics*, 2nd edn., Addison-Wesley publishing, 1987.
- 151- M. ElKabbash, E. Ilker, T. Letsou, N. Hoffman, A. Yaney, M. Hinczewski, G. Strangi, Iridescence-free and narrowband perfect light absorption in critically coupled metal high-index dielectric cavities, *Optics letters*, 42, 18, 3598-3601, 2017.
- 152- Born, M & Wolf, E *Principles of Optics* 7th edn, Cambridge Univ. Press, 2003.
- 153- C.Wadell, F. Anggoro, A. Nugroho, E. Lidström, B. Iandolo, J. B. Wagner, C. Langhammer , Hysteresis-Free Nanoplasmonic Pd–Au Alloy Hydrogen Sensors, *Nano Lett.*, 15 (5), 3563–3570, 2015.
- 154- Z. Zhou, E. Sakr, Y. Sun, P. Bermel, ; Solar thermophotovoltaics: reshaping the solar spectrum, *Nanophotonics* ,5 (1):1–21, (2016). [thermophotovoltaic

-
- 155- Y. Pan, et. al. , A Rapid Response Thin-Film Plasmonic-Thermoelectric Light Detector, *Scientific Reports*, 6, 37564 (2016). [photodetector]
- 156- Jon A. Schuller, Edward S. Barnard, Wenshan Cai, Young Chul Jun, Justin S. White & Mark L. Brongersma, Plasmonics for extreme light concentration and manipulation, *Nature Materials* 9, 193–204 (2010)
- 157- Y. Yang, et. al., Femtosecond optical polarization switching using a cadmium oxide-based perfect absorber, *Nature Photonics* 11, 390–395 (2017).
- 158- Z. Li, S. Butun, K. Aydin, Large-Area, Lithography-Free Super Absorbers and Color Filters at Visible Frequencies Using Ultrathin Metallic Films, *ACS Photonics*, 2 (2), pp 183–188, 2015.
- 159- M. A. Kats, R. Blanchard, P. Genevet , F. Capasso. Nanometre optical coatings based on strong interference effects in highly absorbing media. *Nature Materials*, 12, 20–24, 2013.
- 160- M. A. Kats, F. Capasso, Optical absorbers based on strong interference in ultra-thin films *Optics, Laser & Photonics Reviews* 10 (5), 699, 2016.
- 161- M. ElKabbash, A. Sousa-Castillo, Q. Nguyen, R. Mariño-Fernández, N. Hoffman, M. A. Correa-Duarte, G. Strangi , Tunable Black Gold: Controlling the Near-Field Coupling of Immobilized Au Nanoparticles Embedded in Mesoporous Silica Capsules, *Advanced Optical Materials*, 10.1002/adom.201700617, 2017.
- 162- C. M. Watts, X. Liu, W. J. Padilla, Metamaterial Electromagnetic Wave Absorbers, *Advanced Materials*, 24, OP98–OP120, 2012.
- 163- E. Hecht, *Optics*, 2nd edn., Addison-Wesley publishing, 1987.

-
- 164- C. Hägglund, S. P. Apell, B. Kasemo, "Maximized Optical Absorption in Ultrathin Films and Its Application to Plasmon-Based Two-Dimensional Photovoltaics," *Nano Lett.*, 2010, 10 (8), pp 3135–3141, 2010.
- 165- M. A. Ordal, L. L. Long, R. J. Bell, S. E. Bell, R. R. Bell, R. W. Alexander, Jr., C. A. Ward, Optical properties of the metals Al, Co, Cu, Au, Fe, Pb, Ni, Pd, Pt, Ag, Ti, and W in the infrared and far infrared, *APPLIED OPTICS* , 22, 7 , 1983.
- 166- C. Wang, L. Yin, L. Zhang, D. Xiang , R. Gao, Metal Oxide Gas Sensors: Sensitivity and Influencing Factors, *Sensors*, 10, 2088-2106, 2010.
- 167- J. Gao, et. al. "Experimental realization of epsilon-near-zero metamaterial slabs with metal-dielectric multilayers," *Applied Physics Letters*, 103, 5 , 2013.
- 168- Ting Xu, Amit Agrawal, Maxim Abashin, Kenneth J. Chau & Henri J. Lezec , All-angle negative refraction and active flat lensing of ultraviolet light, *Nature* 497, 470–474 (23 May 2013).
- 169- K. V. Sreekanth, et. al.",Extreme sensitivity biosensing platform based on hyperbolic metamaterials," *Nature Materials* 15, 621–627 (2016).
- 170- M. ElKabbash, E. Ilker, T. Letsou, N. Hoffman, A. Yaney, M. Hinczewski, G. Strangi Iridescence-free and narrowband perfect light absorption in critically coupled metal high-index dielectric cavities, *Optics letters*, 42, 18, 3598-3601, 2017.
- 171- S. Syrenova, C. Wadell, F. A. A. Nugroho, T. A. Gschneidner, Y. A. Fernandez, G. Nalin, D. Świtlik, F. Westerlund, T. J. Antosiewicz, V. P. Zhdanov, K. Moth-Poulsen, C. Langhammer, Hydride formation thermodynamics and hysteresis in individual Pd nanocrystals with different size and shape, *Nature Materials* 14, 1236–1244, 2015.

-
- 172- N. R. Fong, P. Berinibc , R. N. Taita, Hydrogen sensing with Pd-coated long-range surface plasmon membrane waveguides, *Nanoscale*, 7, 2016.
- 173- F.D. Manchester, A. San-Martin, J.M. Pitre, The H-Pd (Hydrogen-Palladium) System, *Journal of Phase Equilibria*, 15, 1, 1994.
- 174- Schwarz, R. B. & Khachaturyan, A. G. Thermodynamics of open two-phase systems with coherent interfaces: Application to metal–hydrogen systems. *Acta Mater.* 54, 313–323, 2006.